Bifurcation-based Ordinary Differential Equation Model Identification

By

Kyoung Hyun Lee

Department of Engineering Mathematics
University of Bristol

A dissertation submitted to the University of Bristol in accordance with the requirements of the degree of Doctor of Philosophy in the Faculty of Engineering.

November 2022

Word count: ten thousand and four

Abstract

Nonlinear dynamical systems that depend on a parameter can dramatically change their dynamic behaviour at particular parameter values. Accurately predicting these topological changes, called bifurcations, in a mathematical model is crucial in many systems. However, getting a quantitative agreement between the model and the physical reality is extremely difficult using either a mechanistic or a data-driven model. Omitted physics of the mechanistic models sometimes causes deterioration in prediction performance. For data-driven models, it is particularly challenging to capture bifurcation with existing data-driven modelling methods, which typically focus on fitting time series data.

We combine studies in dynamical systems, invariant manifold and normal form theories with data-driven modelling to capture the quantitative behaviour of bifurcations in experimental systems. Moreover, we develop techniques not only for model identification but also for data collection to provide a comprehensive modelling approach. Therefore, the thesis has two themes: experimental bifurcation analysis and bifurcation-based model identification.

The first theme, experimental bifurcation analysis, is this thesis's main data-collecting method for modelling systems with bifurcations. Control-based continuation (CBC) is the experimental bifurcation analysis that we focus on and has been successfully used in a wide range of forced systems from previous studies. However, CBC has not yet been applied to self-excited systems; developing and implementing a new CBC scheme for self-excited systems is the main novelty of the first theme.

For the second theme, we first discuss parameter identification methods of ordinary differential equations (ODEs) undergoing Hopf bifurcations using linear system identification techniques and normal form theory to capture the bifurcation structure of the experiment qualitatively. Then, we use machine learning (ML) techniques to identify ODE models using the bifurcation structure as domain knowledge to improve the quantitative agreement between the model and the measured data. Finally, the bifurcation-based ML technique is extended to harmonically forced systems.

We focus on two types of dynamical systems, self-excited systems with Hopf bifurcations and harmonically forced systems with an asymptotically stable equilibrium, representing a wide range of applications in aerospace engineering, biological systems, and mechanical systems.

The primary outcome of the thesis is to develop a bifurcation-based ODE model identification procedure along with associated experimental techniques. The bifurcation structure is the core information of the data-driven modelling in this thesis, and we can accurately predict the response of the system that depends on a parameter. The data efficacy and the accuracy of the predictions are shown in numerical experiments and data-driven modelling examples using physical experiments. One potential application of the method is the development of digital twins that require accurate mathematical models to predict steady-state response depending on a control parameter.

Dedication and acknowledgements

During my PhD study, I faced numerous academic and personal challenges. Despite these difficulties, I am grateful for the many people and experiences that have enriched my life and helped me complete this journey.

I am deeply grateful to my PhD supervisors, Dr. David Barton and Dr. Ludovic Renson, for their invaluable guidance and support throughout my research. Their feedback and suggestions have been instrumental in shaping my academic development, and I appreciate the freedom they gave me to explore different aspects of my work. I am also thankful for the opportunity to study in Bristol, which has been an unforgettable experience.

I would like to express my gratitude to my friends in team DB, Alessandra, Andrea, Sandor, Thiago, Max, and Roussell. I had a great time hanging out with you all and discussing various topics. I hope you all have a happy journey through life.

I must also thank Hong Tang and the Chinese basketball crew for the wonderful times we spent playing basketball together. Those weekly games were the highlight of my week.

I would like to acknowledge my Korean mates, Yoo-chul and Sang-won, for the time we spent living together. The memories we created together are priceless and will stay with me forever.

Special thanks go to my neighbors, Francis Greenacre and Mary Greenacre, for being the best neighbors in the world. Your friendship meant the world to me, and I will never forget your kindness.

I am also deeply grateful to my parents and my sister, Hyun Gee, for their unwavering love and support. Without their help, I would not have been able to start or finish my studies.

Finally, I would like to express my deepest gratitude to Jisuk. You were the one who motivated me to begin this journey, and your constant encouragement made me feel special every day. Every moment in Bristol was interesting because of you.

Author's declaration

I declare that the work in this dissertation was carried out in accordance with the requirements of the University's Regulations and Code of Practice for Research Degree Programmes and that it has not been submitted for any other academic award. Except where indicated by specific reference in the text, the work is the candidate's own work. Work done in collaboration with, or with the assistance of, others, is indicated as such. Any views expressed in the dissertation are those of the author.

SIGNED: Kyoung Hyun Lee, DATE: 1 May 2023

Table of Contents

Page

List of Tables **xi**

List of Figures **xiii**

1 Introduction **1**

2 Background and literature review **5**

2.1 Introduction . . . 5
2.2 ODE model identification . . . 5
2.2.1 Identifiability of ODE models from data . . . 6
2.2.2 Functional structure of the vector field . . . 7
2.2.3 ODE parameter estimation strategies . . . 11
2.2.4 Recent advance in data-driven modelling of ODEs . . . 12
2.3 Invariant manifold of dynamical systems . . . 13
2.3.1 Centre manifold . . . 14
2.3.2 Invariant manifold of a forced mechanical systems . . . 16
2.4 Topological equivalence and the normal form . . . 20

3 Experimental bifurcation analysis **22**

3.1 Introduction . . . 22
3.2 CBC scheme for harmonically forced systems . . . 24
3.2.1 Measuring S-curves using CBC . . . 25
3.3 CBC scheme for self-excited systems . . . 28
3.3.1 Elliptic projected phase-plane case . . . 30
3.3.2 General polar curve projected phase-plane case . . . 33
3.3.3 PP-CBC of a flutter rig . . . 35
3.4 Conclusion . . . 39

4 Parameter estimation of the mechanistic model with Hopf bifurcation **44**

4.1 Introduction . . . 44
4.2 Mathematical model . . . 46

4.2.1 Calculation of the unstable LCOs . . . 46
4.3 Parameter estimation . . . 47
4.3.1 Parameters of underlying linear model . . . 47
4.3.2 Parameters of the nonlinear model . . . 50
4.3.3 Nonlinear parameter updating using collocation methods . . . 51
4.4 Conclusion . . . 54

5 Bifurcation-based data-driven modelling of ODEs with centre manifolds 56
5.1 Introduction . . . 56
5.2 Model structure . . . 58
5.3 Model training . . . 60
5.3.1 Closed orbit representation . . . 60
5.3.2 Functional form of the map . . . 62
5.3.3 Oscillation speed . . . 63
5.3.4 Learning stages . . . 64
5.4 Numerical demonstration . . . 64
5.4.1 Van der Pol oscillator . . . 64
5.4.2 Aeroelastic model . . . 65
5.5 Experimental demonstration on a flutter rig . . . 69
5.5.1 The hybrid M/ML model . . . 69
5.6 Conclusions . . . 71

6 Bifurcation-based data-driven modelling of ODEs with spectral-submanifolds 76
6.1 Introduction . . . 76
6.2 Training ML model for system with invariant manifold . . . 78
6.2.1 Invariant manifold of forced mechanical systems . . . 78
6.2.2 Observation and the bifurcation diagram . . . 78
6.2.3 Data-driven modelling of reduced dynamics on the invariant manifold . . . 79
6.2.4 Summary of the data-driven modelling . . . 84
6.3 ML modelling examples . . . 84
6.3.1 Numerical model: 2-DOF nonlinear oscillator . . . 85
6.3.2 Physical model: nonlinear electromagnetic oscillator . . . 87
6.4 Conclusion . . . 90

7 Conclusion 92
7.1 Conclusions . . . 92
7.2 Limitations of current work and future research suggestions . . . 94
7.3 Possible future application of the thesis . . . 95

A Aeroelastic model 97

Bibliography **99**

List of Tables

Table **Page**

4.1 Measured and identified parameter values of the linearized model. 49

A.1 Descriptions of the parameters of Eq. (A.1) and their values where applicable. Non-dimensional units are indicated by 'nd'. 98

List of Figures

Figure **Page**

2.1 Phase portrait of a three-dimensional system near the supercritical Hopf bifurcation at $\lambda = 0$ 16

3.1 The modified Shaw-Pierre example in [14]. $m = 1$, $k = 1$, $c_1 = \sqrt{3}$, $c_2 = 0.003$ and $\kappa = 0.5$. W is mass, k is linear stiffness coefficient, c is linear damping coefficient, κ is quadratic stiffness coefficient, $f_1 = A\cos(\Omega t)$. $f_2 = 0$ 26

3.2 S-curves of systems studied in Example 3.1. (a) $\Omega = 1.004$. (b) $\Omega = 1.005$. (—) a system without CBC computed using spectral collocation methods, (—) system with CBC computed using numerical integration and algorithm explained in Section 3.2.1. 27

3.3 Nonlinear electromagnetic oscillator (Left) Schematic (Right) Picture [11] 28

3.4 S-curve measured using CBC on an electromagnetic oscillator at forcing frequency 21.3 Hz 29

3.5 24 S-curves measured using CBC on an electromagnetic oscillator 29

3.6 Parametrisation of an elliptic curve 31

3.7 Stabilising control using PP-CBC (left) phase portrait of a system with PP-CBC and uncontrolled system computed via Fourier collocation method. (—) a system without CBC, (•) system with CBC (right) time series of system with PP-CBC and uncontrolled system computed via numerical integration. (—) system without CBC, (—) system with CBC 32

3.8 Bifurcation diagram of PP-CBC compared with numerical continuation of the uncontrolled system. (—) numerical continuation of system without CBC, (•) numerical continuation of system with CBC. 35

3.9 Comparison between system with PP-CBC vs system without control at the wind speed 16 m/s (Left) phase portrait. (—) numerical continuation of system without CBC, (—) numerical continuation of system with CBC, (right) Floquet multipliers. (▲) system with CBC (○) system without CBC. 36

3.10 The nonlinear flutter rig with a rigid NACA-0015 wing profile and two mechanical degrees of freedom (pitch and heave; that is, rotational and vertical motion). Panel (a) is a photograph of the experiment looking towards the trailing edge of the aerofoil; the airflow is from left to right. Panel (b) is a schematic drawing of the experiment. 37

3.11 The response of the flutter rig in open-loop mode (no control active) measured across multiple days. Bistable behaviour is evident for flow velocities between approximately 14 m/s and 25 m/s where a stable limit cycle oscillation in heave and pitch coexists with a stable equilibrium. 38

3.12 Residuals of PP-CBC in amplitude at Wind speed = 17.5 m/s 40

3.13 Measurement of time series at Wind speed = 20 m/s 40

3.14 Multiple measurements of frequency and control error of phase-locked periodic solutions at different amplitudes of control target (a) frequency and (b) error. . . . 41

3.15 CBC results (a) Heave amplitude of LCO (mm), (b) Pitch amplitude of LCO (rad), (c) Frequeny of LCO (Hz). (●) is measured stable LCO and (○) is the measured unstable LCO. 41

3.16 Heave amplitude of measured LCOs (a) Unstable LCO (U=14.9 m/sec), (b) Unstable LCO (Wind speed = 15.6 m/sec), (c) Unstable LCO (Wind speed = 6.5 m/sec), (d) Stable LCO (Wind speed = 14.9 m/sec), (e) Stable LCO (Wind speed = 15.6 m/sec), (f) Stable LCO (Wind speed = 16.5 m/sec). (——) is the heave response of the rig, (——) is the control target. 42

3.17 Pitch amplitude of measured LCOs (a) Unstable LCO (U=14.9 m/sec), (b) Unstable LCO (Wind speed = 15.6 m/sec), (c) Unstable LCO (Wind speed = 16.5 m/sec), (d) Stable LCO (Wind speed = 14.9 m/sec), (e) Stable LCO (Wind speed = 15.6 m/sec), (f) Stable LCO (Wind speed = 16.5 m/sec). 42

3.18 Response of the LCO after the controller was turned off at $t = 3$ sec (a) stable LCO (Wind speed = 16.4 m/sec), (b) unstable LCO (Wind speed = 16.4 m/sec). . . . 43

3.19 CBC results of a different leaf spring setup (a) Heave amplitude of LCO (mm), (b) Frequency of LCO (Hz). (●) is measured stable LCO and (○) is the measured unstable LCO. 43

4.1 Estimation of flutter properties based on normal form (a) flutter speed estimation, (b) flutter frequeny estimation. (——) is the linear regression curve of the measured square of the amplitude of the heave, and (○) is the measured response of system 1, and (△) is the measured response of system 2. (——) indicates x-axis in (a) and the estimated flutter speed of two systems in (b). 49

4.2 Eigenvalues of identified linearised system (a) real eigenvalue, (b) imaginary eigenvalue. (- - -) is mode 1 and (——) is mode 2. (- - -) in (a) is x-axis and (- - -) in (b) is the flutter speed. 50

4.3 Comparison between the bifurcation diagram obtained from numerical continuation of the identified model of system 1 (—) and the CBC result of the system 1 (●). . 52

4.4 Comparison between the bifurcation diagram obtained from numerical continuation of the identified model of system 2 (—) and the CBC result of the system 2 (●). . 52

4.5 Visual description of $\|\mathbf{v}_7\|_h$ and h_7. Numerical continuation of the model(—) and the LCOs measured from CBC experiment (●). $\|\cdot\|_h$ denotes the amplitude of the periodic solution in the heave direction calculated from the periodic grid of $\mathbf{v}_i$. . . 53

4.6 Bifurcation diagram of a mathematical model with updated nonlinear stiffness. Unperturbed model (—) and updated model (—). 55

5.1 Geometric illustration of the coordinate transformation $\mathbf{U}_{12}(u_1, u_2, \mu)$ applied to a LCO of a supercritical Hopf bifurcation. 60

5.2 Combined effect of the different components included in the transformation from normal form coordinates $\mathbf{u}$ to physical space $\mathbf{z}$. (—) LCO obtained after transformation. (●) Experimental data. 63

5.3 Comparison between the Van der Pol model (—) and the physics-guided ML model (—). (a) Bifurcation diagram where (●) are the LCOs used for model training. (b-1-d-1) Phase portrait and (b-2-d-2) time series at the untrained locations are reported on the bifurcation diagram. 66

5.4 Comparison between the phase portraits of the aeroelastic model (—) and the hybrid M/ML model (—) for a stable LCO at $\mu = 15.5\ m/s$. Coordinate transformation (a) without and (b) with the neural network. 67

5.5 Comparison between the aeroelastic model (—) and the physics-guided ML model (—). (a) Bifurcation diagram (●) are stable LCOs and (▲) are unstable LCOs used for model training) (b-d) Phase portrait and (e-g)the time series at the locations reported on the bifurcation diagram. 68

5.6 Comparison between the bifurcation diagram obtained from the hybrid M/ML model with increased model accuracy (—) and the stable (●) and unstable (▲) LCOs used for model training. Labels (a)-(f) denote the corresponding phase portraits and time series plots in Fig. 5.7 and Fig. 5.8, respectively. 70

5.7 Comparison of phase portraits between the measured LCOs (—) and the hybrid M/ML model (—). (a) stable LCO at wind speed 17.3 m/sec, (b) stable LCO at wind speed 16.5 m/sec, (c) stable LCO at wind speed 15.6 m/sec, (d) unstable LCO at wind speed 14.9 m/sec, (e) unstable LCO at wind speed 15.6 m / sec, and (f) unstable LCO at wind speed 16.5 m/sec. 71

5.8 Comparison of heave time series between the measured LCOs (—) and the hybrid M/ML model (—). (a) stable LCO at wind speed 17.3 m/sec, (b) stable LCO at wind speed 16.5 m/sec, (c) stable LCO at wind speed 15.6 m/sec, (d) unstable LCO at wind speed 14.9 m/sec, (e) unstable LCO at wind speed 15.6 m/sec and (f) unstable LCO at wind speed 16.5 m/sec. 72

5.9 Illustration of model overfitting. Bifurcation diagram obtained from the hybrid M/ML model (—), stable (●) and unstable (▲) LCOs used for model training. . . 72

5.10 Effect of excluding one data point from the training data set on the hybrid M/ML model accuracy. (a) Bifurcation diagrams obtained when removing the data point of the same colour. For example, the blue bifurcation curve is obtained when the model is trained with a data set that excludes the blue point. (- - -) Bifurcation diagram obtained from a model trained with all measured data without removing any data points. (b-1) – (e-1) Prediction of the phase portrait at the excluded data point. (b-2) – (e-2) Prediction of time series at the excluded data point. 73

5.11 Mapping $\mathbf{U}_{12}(\mathbf{u},\mu) = (U_1(\mathbf{u},\mu), U_2(\mathbf{u},\mu))$ between normal form and measured coordinates. (a) U_1 at μ=15.0 m/sec, (b) U_2 at μ=15.0 m/sec, (c) U_1 at μ=17.0 m/sec and (d) U_2 at μ=17.0 m/sec. 74

6.1 The modified Shaw-Pierre example in [14]. $m = 1$, $k = 1$, $c_1 = \sqrt{3}$ $c_2 = 0.003$ and $\Gamma = 0.5$. m is mass, k is linear stiffness coefficient, c is linear damping coefficient, κ is quadratic stiffness coefficient, $f_1 = f_2 = F_0 \cos(\Omega t)$. 85

6.2 FRC computation at (a) training data sets (b) at untrained data sets with forcing amplitudes $F_0 = 0.003, 0.006, 0.009$ and 0.012. (—) is computed FRC from the ground truth model, (—) is computed FRC from the ML model, (- - -) is computed backbone curve from the ML model, and (●) are training data sets. 86

6.3 Predicting observation at trained data sets (a) $F_0 = 0.01$, $\Omega = 1.003$ rad/sec (b) $F_0 = 0.01$, $\Omega = 0.966$ rad/sec. (—) is the predicted time series from the model, and (●) is the time series of the ground truth model. 86

6.4 Predicting observation at untrained data sets (a) $F_0 = 0.005$, $\Omega = 1.002$ rad/sec (b) $F_0 = 0.009$, $\Omega = 1.00$ rad/sec. (—) is the predicted time series from the model, and (●) is the time series of the ground truth model. 87

6.5 Predicting observation at untrained data sets with high forcing amplitudes (a) $\Gamma = 0.012$, $\Omega = 0.0988$ rad/s (b) $\Gamma = 0.012$, $\Omega = 1.008$ rad/s. (—) is the predicted time series from the model, and (●) is the time series of the ground truth model. . 87

6.6 S-curves computed from an ML model trained using 24 measured S-curves. (●) are training data sets, (●) are validation data sets, and (—) are computed S-curves from the ML model. 88

6.7 S-curves computed from an ML model trained using 12 measured S-curves. (●) are training data sets, (●) are validation data sets, and (—) are computed S-curves from the ML model. 89
6.8 S-curves computed from an ML model trained using 5 measured S-curves. (●) are training data sets, (●) are validation data sets, and (—) are computed S-curves from the ML model. 89
6.9 Prediction of backbone curve from ML model. (—) are computed backbone curves from the ML models, and (●) is a measured backbone curve. The measured backbone curve is measured between 18.59 Hz to 24.36 Hz using 47 points in frequency domain. S-curves used for ML model training ranges from 17.5 Hz - 23.4 Hz which are computed using numerical continuation. 90
6.10 Prediction of time-series at validation sets (a) frequency 18.5 Hz, forcing amplitude 0.42 (b) frequency 20.8 Hz, forcing amplitude 0.16 (c) frequency 22.8 Hz, forcing amplitude 0.21. (—) is measured time series, and (—) is predicted time series from the model. 90

A.1 Schematic of an aeroelastic system of Eq. (A.1). 98

CHAPTER 1

Introduction

In the presence of nonlinearity, dynamical systems can exhibit bifurcations, leading to a wide range of dynamic behaviours. For example, the system can exhibit completely different dynamic responses depending on a system parameter, such as stability change of equilibrium and periodic solutions. A mathematical model that can accurately predict the response is crucial in these systems. The model prediction can be completely wrong when the model does not accurately capture the stability change of the limit sets depending on a parameter.

Mechanistic models are a common choice for researchers working on systems with bifurcations. Mechanistic models are derived from physical principles, which makes them interpretable and also provides physical insights. However, predicting the dynamic response from mechanistic models can be inaccurate, as the typical model derivation neglects complex nonlinear effects from the assumptions.

Data-driven modelling, i.e. deriving a mathematical model from data, offers many valuable tools that remove the limitations of mechanistic models. Model identification of dynamical systems from data has been studied for decades under the name of system identification [55]. System identification uses statistical methods to identify unknown parameters of dynamical system models. Much literature on system identification is focused on discrete-time dynamical systems because of its usefulness with digital control systems. Recently, advanced numerical solvers [77], auto differentiation packages [58], and machine learning packages [28, 41] have allowed us to identify differential equation models with a high degree of model flexibility compared to traditional system identification approach. However, these existing dynamical system model identification methods focus on fitting measured time series data, making it challenging to generate a model with the same bifurcation structure as the experiment. Data-driven modelling of ODEs with multiple time series can easily end at a local minimum of the data-fitting criteria that do not necessarily have the same bifurcation structure as the physical

system. It is also challenging to train the model to reproduce unstable limit sets that nonlinear parameter-dependent systems commonly have, which limits the amount of information provided during training.

We aim to develop an ordinary differential equation (ODE) identification method that captures the bifurcation of an experiment to address the limitations of existing dynamical system model identification methods. Furthermore, we develop a comprehensive modelling approach, including data collection methods, employing control-based continuation (CBC). The main idea is to combine dynamical system studies, invariant manifolds and normal form theories with recent advances in data-driven modelling techniques. Therefore, the thesis has two themes, experimental bifurcation analysis and bifurcation-based model identification, considering two types of dynamical systems: self-excited systems with Hopf bifurcation and harmonically forced mechanical systems with an asymptotically stable equilibrium.

Limit-cycle oscillations (LCOs), periodic responses in self-excited systems, are present in many engineered systems. For example, the flutter of aircraft wings [1], the shimmy of towed wheels [12], and the chatter of machine tools [44] are self-excited systems with LCOs. These systems are typically modelled with autonomous ODEs that contain a control parameter. The family of LCOs arising from a Hopf bifurcation can be subcritical or supercritical. The subcritical case is more problematic than the supercritical case as it leads to sudden jumps to other solution branches from the stable equilibrium under random perturbations. This can have catastrophic consequences, such as the failure of NASA helios [64] and Facebook's Aquila UAV [107], when they are not accurately modelled and understood.

Another fundamental type of dynamical system in engineering systems is harmonically forced mechanical systems. Harmonically forced systems are ubiquitous as rotating machines apply harmonic forces to the system, which are the primary excitation source in many engineered systems. Predicting accurate resonant responses where the excitation frequency is close to one of the linear modal frequencies is vital to the system's functionality. Predicting a precise frequency response of the system by considering forcing amplitude and frequency as control parameters is especially crucial in lightweight engineering systems such as microelectromechanical systems (MEMS). However, predicting the system's frequency response is challenging when the system's nonlinearity is not negligible. In this case, the system can have a bistable frequency response that can cause sudden jumps.

The thesis's overall structure is as follows. In Chapter 2, the theoretical background of the thesis and associated literature reviews are presented. For the first theme, experimental bifurcation analysis, we discuss the scheme for bifurcation analysis in an experiment, control-based continuation (CBC), in Chapter 3. For the second theme, we introduce three bifurcation-based ODE model identification methods. One is the model identification method developed to identify the parameters of the mechanistic models, which is discussed in Chapter 4. The other two methods are the ML-based approach which uses the invariant manifold and the bifurcation

structure as domain knowledge. Different ML approaches are applied for a system with Hopf bifurcation and for harmonically forced systems with an asymptotically stable equilibrium. The ML-based approach to model the Hopf bifurcation is discussed in Chapter 5, and harmonically forced systems with an asymptotically stable equilibrium are discussed in Chapter 6.

In previous studies, CBC was studied and applied to various harmonically forced systems [11, 84–86], which we introduce the scheme with numerical and experimental examples in Chapter 3. However, CBC was not previously applied to self-excited systems. Therefore, the development and application of CBC for the bifurcation analysis of self-excited systems with Hopf bifurcation is the main contribution of Chapter 3. The difference between CBC for the self-excited system and the forced system is that we parametrise the control target using a phase angle, whereas the forced system parametrises the control target using the external force. We provide numerical examples of developed CBC schemes for self-excited systems and an experimental demonstration applied to a flutter rig in a wind tunnel.

In Chapter 4, we develop a parameter identification method for the system with Hopf bifurcation that can be applied to mechanistic models. We suggest a three-stage parameter identification process in which we identify the linearisation of the model in the initial stage using linear system identification techniques. In the second stage, we parameterise the LCOs near the Hopf bifurcation point by unknown nonlinear stiffness parameters using centre manifold reduction and normal form analysis. Finally, the parameters are updated using spectral collocation methods considering the high-amplitude LCOs that were not considered in the initial optimisation of the nonlinear stiffness parameters. We provide a model identification example from a CBC experiment result discussed in Chapter 3.

In Chapter 5, we develop data-driven modelling of a system with a centre manifold using ML. This research is initially motivated by the desire to improve the prediction quality of the model identification method developed in Chapter 4. A normal from-like equation is the basis of the model that captures the bifurcation structure of the experimental system. Mapping between the centre manifold and the measured signals is modelled using a neural network. We provide data-driven modelling examples from synthetic data of the van der Pol oscillator and an aeroelastic flutter model. The results of the CBC experiment discussed in Chapter 3 are also used to train an ML model in Chapter 5.

In Chapter 6, we developed data-driven modelling of harmonically forced mechanical systems with asymptotically stable equilibrium using ML. The ML approach developed in Chapter 6 also focuses on capturing the bifurcation of the experimental system. However, the ML modelling approach developed in Chapter 6 is slightly different from the ML approach in Chapter 5 as the phase of the external force and the phase-lag of the periodic response give the core information of the modelling. Moreover, the input-output map is generated from frequency responses of a harmonically forced system where kernel ridge regression is used for data-driven modelling. The developed ML approach is demonstrated on synthetic numerical data generated from a

2-DOF nonlinear oscillator model, which shows good agreement with the ground-truth model. It is also demonstrated in an experimental CBC result shown in Chapter 3, which also shows good prediction results in validation data sets and the prediction of the backbone curve.

Finally, the conclusions of the research work presented in this thesis are discussed in Chapter 7 with further discussions on the limitations of the study and future work suggestions.

Publications

- The contents of Chapters 3 and 4 are in preparation for submission to the journal.
  - Title: Analysis of self-excited flutter oscillations with control-based continuation
  - Authors: K.H. Lee, I. Tartaruga, D. Rezgui, L. Renson, S.A. Neild, and D.A.W. Barton
- Contents of Chapter 5 is published in a journal.
  - Title: Modelling of physical systems with a Hopf bifurcation using mechanistic models and machine learning
  - Authors: K.H. Lee, D.A.W. Barton, and L. Renson
  - Journal: Mechanical system and signal processing
- The contents of Chapter 6 are in preparation for submission to the journal.
  - Title: Data-driven modelling of the forced system using experimental bifurcation analysis
  - Authors: K.H. Lee, D.A.W. Barton, and L. Renson
- Part of Chapter 5 is published in conference proceedings.
  - Title: Reduced-order modelling of flutter oscillations using normal forms and scientific machine learning
  - Journal: Advances in Nonlinear Dynamics, Proceedings of the Second International Nonlinear Dynamics Conference (NODYCON 2021)
  - Authors: K.H. Lee, D.A.W. Barton, and L. Renson

CHAPTER 2

Background and literature review

2.1 Introduction

In this chapter, we review the research and theoretical background of the thesis. The main subject of the thesis is the mathematical modelling of ODEs with bifurcations using experimental data. Therefore, we discuss the data-driven modelling of ODEs in Section 2.2. Invariant manifold theories, centre manifold and spectral submanifolds used throughout the thesis are discussed in Section 2.3. Topological equivalence is the key idea to define the dynamics of the invariant manifold in Chapters 4 to 6 using the information on the bifurcation structure. Therefore, we will explain the topological equivalence in Section 2.4.

2.2 ODE model identification

In this thesis, we consider ODE models depending on a parameter to study data-driven modelling of systems with bifurcations. The ODE model identification problem in this thesis considers two equations:

$$\dot{\mathbf{x}} = \mathbf{F}(\mathbf{x};\theta), \tag{2.1a}$$

$$\mathbf{y} = \varphi(\mathbf{x};\theta), \tag{2.1b}$$

where $\mathbf{x} \in \mathbb{R}^N$ is the state space vector, $\theta \in \mathbb{R}^p$ is the model parameters vector, $\mathbf{y} \in \mathbb{R}^m$ is the vector of observations, $\mathbf{F} : \mathbb{R}^N \times \mathbb{R}^p \to \mathbb{R}^N$ is the vector field, and $\varphi : \mathbb{R}^N \times \mathbb{R}^p \to \mathbb{R}^m$ is an observation function. Note that Eq. (2.1a) does not have a time-dependent term; however, the time-independent vector field can cover a wide range of dynamic problems, including self-excited

systems and harmonically excited systems. We can also consider the control parameter as a state variable with time derivative zero.

The first step in identifying the model is to choose the functional structure of the vector field $\mathbf{F}$. Solutions of Eq. (2.1a) uniquely exist given initial condition $\mathbf{x}(0) = \mathbf{x}_0$ if $\mathbf{F}$ is Lipschitz continuous with respect to $\mathbf{x}$. The identification of the ODE model is to estimate θ from observed data $\mathbf{y}_1, \ldots, \mathbf{y}_n$ at the measured time $t = t_1, \ldots, t_n$ by minimising or maximising certain data-fitting criteria.

In Section 2.2.1, we review the study of the identifiability of ODE models. Identifiability of ODE models is still an ongoing field, and theoretical work is limited to ODE models with particular model classes and may not provide answers to complex structures [99]. However, we can learn many valuable concepts and conditions that make parameter identification of the ODE a well-defined problem. The process of data-driven ODE modelling follows by choosing the vector field's functional structure and identifying the system's unknown parameters from the data. We will discuss the types of functions that are applicable to modelling the vector field $\mathbf{F}$ in Section 2.2.2. In Section 2.2.3, we review the strategy for training ODE models using data-fitting criteria. Finally, we review recent research on the data-driven modelling of ODEs.

2.2.1 Identifiability of ODE models from data

Here, we will review an important concept for the model identification of ODEs, namely identifiability. We consider the parameter identification problem of Eqs. (2.1a) and (2.1b) with a given initial condition $\mathbf{x}_0$ with a time-independent parameter θ. The dynamical system given by Eqs. (2.1a) and (2.1b) is said to be **structurally locally identifiable** [61] if there exists a neighbourhood of θ_p, $\mathcal{N}(\theta_p) \subset \mathbb{R}^p$, such that the model parameters are one-to-one with the measured output, i.e. $\varphi(\mathbf{x}(t, \mathbf{x}_0); \theta) = \varphi(\mathbf{x}(t, \mathbf{x}_0); \bar{\theta})$ if and only if $\bar{\theta} = \theta$ for $\theta, \bar{\theta} \in \mathcal{N}(\theta_p)$ where $\mathbf{x}(t, \mathbf{x}_0)$ is a solution of an initial value problem with a given initial condition $\mathbf{x}_0$ in a time interval $t \in [0, T]$. **Structurally globally identifiable** [61] system is when $\mathcal{N}(\theta_p)$ covers the whole parameter space.

Åström [9] used Laplace transform to study the structural identifiability of linear ODE models. For nonlinear ODE models, the differential algebra approach is widely used by researchers where $\mathbf{F}, \varphi$ are rational functions in Eqs. (2.1a) and (2.1b). Using the theory of differential algebra, Eqs. (2.1a) and (2.1b) is transformed into a finite set of a nonlinear algebraic equation, which is called a characteristic set. The characteristic set gives a summary of the input-output map generated by Eqs. (2.1a) and (2.1b) where we can analyse the identifiability. However, the differential-algebra approach has limitations on high-dimensional systems and is only applicable to systems with rational functions. The general concept of structural identifiability research, including the differential algebra approach and other identifiability studies, is reviewed in [61].

We do not study identifiability, e.g. Laplace transformation and differential algebra approach, in this thesis, as the developed schemes for identifiability analysis are only available for limited

functions. Structural identifiability makes data-driven modelling a well-defined problem, and the identified parameters physically meaningful. However, we will assume local structural identifiability for data-driven modelling problems for the rest of the thesis.

2.2.2 Functional structure of the vector field

Choosing the functional structure of the data-driven model is an essential step in mathematical modelling. One option is to use a mechanistic model, such as the Lotka-Volterra model, to model the dynamics of biological systems. We can also use universal approximators, such as neural networks or kernel functions, which will generally work for smooth dynamical systems. The universal approximation is a property of a class of functions that can approximate a bounded continuous function with a given accuracy defined by the maximum norm. Deep neural networks and kernel functions in reproducing Hilbert kernel spaces (RKHs) (Definition 2.1) can approximate any bounded continuous function in this sense [37, 63].

Neural networks are functions with free parameters called weight vectors, and kernel functions are nonparametric functions defined from kernels and the input-output map. Neural networks are computationally effective compared to kernel methods when there is a large set of training data. However, neural networks perform poorly when there is a small set of training data, and it is not easy to control the complexity of the model. Kernel methods that use kernel functions perform reasonably well with small training data, and it is convenient to control the complexity of the model using hyperparameters. However, the computational cost increases when the training data set is large, and it is not easy to use kernel functions when there are no entire input-output data of a model.

This subsection will review three important classes of functions in this thesis, linear time-invariant systems, neural networks, and kernel functions. The linear time-invariant system is one of the essential function classes for modelling the vector field. Neural networks and kernel functions are important functional structures in data-driven modelling used in Chapters 5 and 6.

Linear time-invariant systems

Linear time-invariant systems are often the first choice for dynamic modelling of scientific problems. For example, coupled spring-mass systems, LR-electric networks, and pesticide models in soil and trees can be modelled using linear systems.

$$\mathbf{F}(\mathbf{x};\theta) = \mathbf{A}(\theta)\mathbf{x}, \tag{2.2}$$

where $\mathbf{A} : \mathbb{R}^p \to \mathbb{R}^{N\times N}$. Time-invariant linear systems have more options, such as frequency domain parameter identification methods [59], for parameter identification than nonlinear systems and time-varying systems, as the solution is a linear superposition of eigenvectors of $\mathbf{A}$.

Feedforward neural network

The feedforward neural network is a nonlinear function structured with nodes and layers, which is a powerful function approximator. The nodes are the location where the real number is stored in each layer. Let $a^{n-1} \in \mathbb{R}^k$ be the k length vector of the nodes in the $n-1$ -th layer. The weight matrix $W \in \mathbb{R}^{j \times k}$ connects the vector of length j of the nodes in the n -th layer $a^n \in \mathbb{R}^j$ using the formula

$$a^n = \sigma(W a^{n-1} + b_n), \tag{2.3}$$

where $b_n \in \mathbb{R}^j$ is a bias and σ is an activation function that passes the scalar stored in each node in the n-th layer. We employ the following notation for vector input for activation functions:

$$\sigma([x_1, \ldots, x_l]) = [\sigma(x_1), \ldots, \sigma(x_l)]^T, \text{ for } x_1, \ldots, x_l \in \mathbb{R}. \tag{2.4}$$

Hyperbolic tangent, softmax, and rectified linear unit (ReLU) are examples of common activation functions in machine learning.

The deep neural network is a universal approximator [40] which means that it can approximate any continuous function defined in a compact domain up to the desired accuracy with a sufficiently large depth or length. Therefore, we can model the vector field $\mathbf{F}$ or an observation φ using a neural network. For example, neural ODE [23] is the modelling of the vector field using a neural network as

$$\dot{\mathbf{x}} = \sigma(W_l \sigma(\ldots \sigma(W_2 \sigma(W_1[\mathbf{x}] + b_1) + b_2) \ldots) + b_l), \tag{2.5}$$

$$\theta = [\mathrm{vec}(W_1); \ldots; \mathrm{vec}(W_l); b_1; \ldots; b_l], \tag{2.6}$$

where $\mathrm{vec}(\cdot)$ denotes the vector that collects the columns of the matrix. For example, $vec(I) = [1, 0, 0, 1]^T$ where I is 2×2 identity matrix. The model parameter θ consists of weights and biases.

In Chapter 4, neural networks are used to model the mapping between the invariant manifold and the measured signals. Also, neural networks are used to model the oscillation speed of self-excited systems.

Functions in reproducing kernel Hilbert space (RKHS)

Two popular nonparametric regression approaches use positive definite kernels in machine learning. One is Bayesian machine learning with a Gaussian process that models problems producing a posterior distribution as output [81]. Another approach is frequentist kernel methods, kernel ridge regression, which searches optimised solutions of a regression problem in reproducing kernel Hilbert space (RKHS) [45]. In this subsection, we review the general concept of kernel ridge regression.

RKHS is a Hilbert space of functions with point evaluation and is a linear representation called a representer (Definition 2.1).

Definition 2.1. Reproducing kernel Hilbert space (RKHS) [106]
A reproducing kernel Hilbert space (RKHS) is a Hilbert space in which $\forall x \in \mathcal{X}$, $\exists R_x \in \mathcal{H}$ such that all functions in RKHS, f, can be evaluated as $f(x) = \langle R_x, f \rangle_{\mathcal{H}}$ where $\mathcal{X}$ is a nonempty feature space which is the space that input data lives and $\mathcal{H}$ is a Hilbert space of real-valued functions on $\mathcal{X}$. That is, function evaluation has a linear representation in the Hilbert space $\mathcal{H}$. R_x is the representative of the evaluation for x.

Definition 2.2. Positive semi-definite (PSD) Kernels [106]
A function $k : \mathcal{X} \times \mathcal{X} \to \mathbb{R}$ is a positive semidefinite (PSD) kernel if $\forall n \in \mathbb{N}$ and $x_i \in \mathcal{X}$, the matrix $K \in \mathbb{R}^{n \times n}$ with $K_{ij} = k(x_i, x_j)$ is symmetric and positive semidefinite. A matrix $K \in \mathbb{R}^{n \times n}$ is positive semidefinite if $\forall a \in \mathbb{R}^n$, $a^T K a \geq 0$.

Every positive semidefinite (PSD) kernel k produces a unique RKHS, $\mathcal{H}_k$, which means that RKHS and positive definite kernels are one-to-one. Square-exponential kernels, polynomial kernels, Matern kernels [45] are popular kernels used in ML applications. We can construct an RKHS, $\mathcal{H}_k$, for a given positive definite kernel k. First, let $\mathcal{H}_0$ be the linear span of representers as

$$\mathcal{H}_0 := \text{span}\{k(\cdot, x) : x \in \mathcal{X}\}$$

$\mathcal{H}_0$ is a Hilbert space with inner product

$$\langle f, g \rangle_{\mathcal{H}_0} = \sum_{i=1}^{n} \sum_{j=1}^{m} a_i b_j k(x_i, y_j).$$

RKHS $\mathcal{H}_k$ associated with k is defined as $\mathcal{H}_k = \overline{\mathcal{H}_0}$ which can be written as

$$\Big\{ f = \sum_{i=1}^{\infty} c_i k(\cdot, x_i) \ : c_i \in \mathbb{R}, x_i \in \mathcal{X}, \quad s.t. \quad \|f\|^2_{\mathcal{H}_k} = \sum_{i=1}^{\infty} \sum_{j=1}^{\infty} c_i c_j k(x_i, x_j) < \infty \Big\}.$$

RKHS, $\mathcal{H}_k$, gives us a nice function space where we can find a solution to a regression problem defined by minimising the data fitting criteria. Given a nonempty set $\mathcal{X}$, a positive definite real-valued kernel $k : \mathcal{X} \times \mathcal{X} \to \mathbb{R}$, training samples $(x_1, y_1), \ldots, (x_m, y_m) \in \mathcal{X} \times \mathbb{R}$, $f \in \mathcal{H}_k$ minimising the following

$$\frac{1}{m} \sum_{i=1}^{m} (f(x_i) - y_i)^2 + \lambda \|f\|^2_{\mathcal{H}_k},$$

where λ is a regularisation constant, admits a representation of the form

$$f(\cdot) = \sum_{i=1}^{m} \alpha_i k(\cdot, x_i).$$

This result is called the representer theorem [92]. Using the representer theorem, we can solve a regression problem using functions in RKHS $\mathcal{H}_k$, which minimises the prediction error at the data points. Moreover, kernel functions provide a smooth function in feature space by interpolating and extrapolating the input data, as in the following example.

Example 2.1. ***Kernel ridge regression*** *[106]*

We assume a model of the form $y = f(x) + \varepsilon$, where ε is an additive noise. The goal is to identify f from observed data sets $(x_i, y_i) \in (\mathbb{R}^d \times \mathbb{R})$ are observed. Kernel ridge regression seeks $\hat{f}$ such that $y_i = \hat{f}(x_i) + w_i$ for $i = 1, \ldots, n$. Given RKHS, $\mathcal{H}_k$, with kernel k, we find $\hat{f}$ by solving an optimisation problem:

$$\hat{f} = \underset{f \in \mathcal{H}_k}{\operatorname{argmin}} \frac{1}{m} \sum_{i=1}^{m} (y_i - f(x_i))^2 + \lambda \|f\|^2_{\mathcal{H}_k}$$

The first term is the data fit term and the second term is a regularisation term. By the representer theorem, $\hat{f}$ takes the form

$$\hat{f}(\cdot) = \sum_{j=1}^{n} \alpha_j k(\cdot, x_j)$$

let $\mathbf{y} = [y_i, \ldots, y_n]^T \in \mathbb{R}^n$ and $\mathbf{K} \in \mathbb{R}^{n \times n}$ with $K_{ij} = k(x_i, x_j)$. Then, the original problem is equivalent to

$$\hat{\alpha} = \underset{\alpha \in \mathbb{R}^n}{\operatorname{argmin}} \frac{1}{m} \|\mathbf{y} - \mathbf{K}\alpha\|_2^2 + \lambda \alpha^T \mathbf{K} \alpha.$$

Taking the gradient of the loss function and using the symmetric property of $\mathbf{K}$, we have

$$\hat{\alpha} = (\mathbf{K} + \lambda \mathbf{I})^{-1} \mathbf{y},$$

which is one solution to the optimisation problem.

We can model the vector field $\mathbf{F}(x; \theta)$ of an autonomous ODE using functions in RKHS $\mathcal{H}_k$ as shown in Example 2.1 by setting the output vector $\mathbf{y}$ as a model parameter [39] as

$$\mathbf{F}(\mathbf{x}) = \mathbf{K}(\mathbf{x}, \mathbf{Z})(\mathbf{K}(\mathbf{Z}, \mathbf{Z}) + \lambda \mathbf{I})^{-1} \mathbf{U}^{\mathrm{T}}, \tag{2.7}$$

where $\mathbf{Z} = [\mathbf{z}_1, \ldots, \mathbf{z}_M]$ is the inducing location and $\mathbf{U} = [\mathbf{u}_1, \ldots, \mathbf{u}_M]$ is the inducing vectors. Inducing vectors, $\mathbf{u}_1, \ldots, \mathbf{u}_M$, define the vector field of the differential equation as in Eq. (2.7). In this case, the model parameters vector is $\theta = [\theta_h, \mathbf{U}]^T$ where θ_h is a kernel hyperparameter, such as a length scale and the scale factor. $\mathbf{K}(\mathbf{x}, \mathbf{Z})$ in the above equation allows us to evaluate

the function $\mathbf{F}(\mathbf{x})$ at the points $\mathbf{x} \neq \mathbf{Z}$ which is called interpolation if the evaluation point is between the input data and extrapolation if not.

Choosing a type of kernel and optimising the kernel's hyperparameters is the most important procedure of data-driven modelling using kernel functions. The interpolation and extrapolation of the training data sets using the model strongly depend on the hyperparameters of the kernel. Hyperparameter tuning techniques are discussed in [81].

In this thesis, kernel ridge regression is used to model the dynamics of forced mechanical systems in Chapter 6, where we can construct an input-output map using the response of forced mechanical systems.

2.2.3 ODE parameter estimation strategies

Typically, parameter identification of ODE problems is transformed into an optimisation problem using data-fitting criterion $\mathcal{L}$. For example, we can use the mean squared error (MSE) as a data-fitting criterion

$$\mathcal{L}(\theta) = \frac{1}{N}\sum_{i=1}^{N} \|\mathbf{y}_i - \varphi(\mathbf{x}_i(\theta), \theta)\|^2, \tag{2.8}$$

where subindex i denote i-th time step of the training data, and $\mathbf{x}_i$ is the numerical solution of Eq. (2.1a) at time $t = t_i$. The optimised value $\hat{\theta} = \underset{\theta}{\operatorname{argmin}}\, \mathcal{L}$ gives us the parameter of the ODE model that fits the data best in the sense of a minimum MSE. Once the data fitting criterion $\mathcal{L}$ is defined, we can use standard optimisation packages to identify the unknown parameters of the model.

The data fitting criterion in Eq. (2.8) typically requires a numerical solution of the ODE defined in Eq. (2.1a). The classical way of solving this optimisation problem is by using numerical integration, such as the Runge-Kutta methods [19]. Other strategies estimate unknown parameters θ of the ODE model, using different approaches such as matching the gradients or expanding the solution using basis functions. In this section, we will introduce several strategies.

Explicit numerical integration of ODEs

Data fitting by numerical integration is often used to identify parameters of ODE models. Data fitting criteria are a function of $\mathbf{x}_\theta$ and θ as $\mathcal{L} = \mathcal{L}(\mathbf{x}_\theta, \theta)$. Note that we use the subscript θ since $\mathbf{x}(t)$ depends on the model parameter θ. Differentiating $\mathbf{x}_\theta$ from θ for optimisation is inefficient since we need differentiation over a numerical integration. Alternatively, we can define an adjoint problem to compute the gradient of $\mathcal{L}$ as (see [23])

$$\frac{d\mathcal{L}}{d\theta} = -\int_{t_0}^{t_N} \mathbf{a}(t)\frac{\partial \mathbf{F}(\mathbf{x}, t; \theta)}{\partial \theta}\, dt \tag{2.9}$$

where $\mathbf{a}(t) = \frac{d\mathcal{L}}{d\mathbf{x}}$. The numerical solution of Eq. (2.9) gives a Jacobian of $\mathcal{L}$, which is much more efficient than differentiating $\mathbf{x}_\theta$ directly with θ. Julia package DiffEqFlux.jl [75, 76] offers advanced features of adjoint sensitivity analysis for parameter identification of ODE models. This scheme is used to identify the speed of the oscillations of self-excited systems in Chapter 5.

Matching time-derivatives

Two-step methods are indirect parameter estimation methods that do not use numerical integration, as suggested by Varah [103] and developed by Chen [22], Brunel [15]. The first step identifies the time-dependent function from the measured time series to compute the time derivatives at the sampling points. Then, the parameters of the ODE model are estimated to fit the estimated time derivatives to the vector field of the model. Two-step methods are generally computationally efficient compared to schemes using numerical integration. However, two-step methods show poor parameter estimation results when the measured data contain relatively high noise.

Poyton [71] improved two-step methods to address measured noise problems by adding a model-based roughness penalty. This approach improves the smoothness of the time derivatives and estimates physically reliable parameters as a result.

Generalised profiling method [80]

The generalised profiling method computes the solution of ODEs by expanding the solution as a basis function expansion as

$$\mathbf{x} = \Phi\mathbf{c},$$

where Φ is the basis function matrix and $\mathbf{c}$ is the coefficient of basis expansion. There are two loss functions for parameter identification. One is the so-called inner fitting criterion to evaluate the basis expansion quality, and another is a typical data-fitting criterion.

Generalised profiling methods are reported to be robust to noise and computationally efficient. However, the generalised profiling method performs poorly when the chosen bases Φ do not approximate the solution properly.

2.2.4 Recent advance in data-driven modelling of ODEs

Neural ODE [23] has received significant attention from the data-driven modelling community and inspired many related studies. The initial study of neural ODE modelled the vector field using only neural networks. We can train any smooth ODE model by choosing a sufficiently deep neural network that reproduces the measured data. However, the training is computationally expensive when the model has a high-dimensional state space.

One way to overcome the issue of neural ODE is to use domain knowledge by making a hybrid model of a mechanistic model and an ML structure. Research [26, 60] show that adding ML structure improves traditional disease models. It is also shown in [76] that these hybrid models are also easier to train than black-box models and have superior extrapolation quality. DiffEqFlux.jl is one of the most advanced ODE model identification packages that covers neural ODEs to hybrid ODE models. However, data-driven ODE modelling methods using a neural network lack interpretability, as a neural network does not give any physical meanings. Furthermore, controlling the complexity of the model under noisy data is a challenge.

The sparse identification of nonlinear dynamics(SINDy) [43] algorithm is also a recently developed data-driven ODE modelling method. SINDy uses a library of functions to model the vector field of the ODE and identifies the model through sparsity-promoting optimisation, which selects the fewest possible terms from a library of functions. SINDy gives a model that is interpretable compared to methods that use neural networks and are less prone to overfitting issues. However, the limitation of SINDy is that the design of the function library can make model identification ill-conditioned when the library is too extensive and make a model less descriptive when the library is too small.

The data-driven ODE modelling methods mentioned above focus on fitting time series data using numerical solvers. Here, we focus on fitting a system's bifurcation diagram using the results of the CBC experiment. For systems undergoing bifurcation, unstable periodic solutions also convey essential information about the system, which is problematic to use as training data sets when numerical integration solvers are used. Developing data-driven ODE modelling methods capable of training unstable periodic solutions is one of the contributions of this thesis. For this purpose, we use the information of bifurcation and invariant manifold as domain knowledge, which will be discussed in the later sections.

2.3 Invariant manifold of dynamical systems

An invariant manifold is a geometrical object contained in the state space of a dynamical system. For example, let us say that there is a surface in a three-dimensional state space where the response remains if the initial condition is on this surface. Then, we call this surface an invariant manifold.

In many models of dynamical systems, reduced-order models are derived using an invariant manifold when the dimension of the invariant manifold is smaller than the entire state space. Two types of dynamical systems considered in this thesis have invariant manifolds, centre manifolds, and spectral submanifolds. Throughout this thesis, we use these invariant manifolds as the core information for data-driven ODE modelling.

We can generalise this concept to a compact manifold that has a boundary. Let M be a compact manifold with a boundary embedded in $\mathbb{R}^N$ and let $\phi^t(\cdot)$ denote the flow defined by

the vector field. M is called **invariant manifold** if for every $p \in M$, we have $\phi^t(p) \in M$ for all $t \in \mathbb{R}$. Similarly, we call M **overflowing invariant manifold** if the flow in the boundary of M, ∂M, flows out from M and **inflowing invariant manifold** if the flow flows into M at the boundary (see [48]).

Invariant manifolds used in this thesis– centre manifold and spectral submanifold– can be understood as extensions of linear subspaces defined near the equilibrium. We can understand this concept more precisely by Fenichel's theorem for the invariant manifold [32]. General Fenichel's Theorem considers two dynamical systems:

$$\dot{\mathbf{x}} = \mathbf{F}(\mathbf{x}), \tag{2.10a}$$

$$\dot{\mathbf{x}} = \mathbf{F}^{\text{pert}}(\mathbf{x}), \tag{2.10b}$$

where $\mathbf{F}^{\text{pert}}$ is a perturbed vector field of $\mathbf{F}$ where the perturbation is small. Small perturbation means that $\|\mathbf{F}(\mathbf{x}) - \mathbf{F}^{\text{pert}}(\mathbf{x})\|$ is small (see [48] for the precise definition of small perturbation).

Fenichel's first theorem indicates that a perturbed vector field, Eq. (2.10b), has an overflowing invariant manifold, which is a smooth deformation of the overflowing invariant manifold of Eq. (2.10a). The necessary condition for Fenichel's first theorem is that the dynamics of the normal direction of the invariant manifold is faster than the tangential dynamics of the invariant manifold (see [48, 109] for the formal condition, which is called normally hyperbolic invariant manifold (NHIM)). In this case, we say that the invariant manifold of Eq. (2.10a) persists under the perturbation.

According to Feinichel's first theorem, a stable and unstable manifold near a hyperbolic equilibrium of a linear dynamical system $\dot{\mathbf{x}} = \mathbf{A}\mathbf{x}$, where $\mathbf{A} \in \mathbb{R}^{n\times n}$ is a constant matrix with no zero real eigenvalues, persists under adding small nonlinear perturbations to the vector field. See [109] for details, where it uses Fenichel's first theorem to prove the existence of classical stable and unstable invariant manifolds near hyperbolic equilibrium.

2.3.1 Centre manifold

A dynamical system with a nonhyperbolic equilibrium also has an invariant manifold. Consider a dynamical system $\dot{\mathbf{x}} = \mathbf{A}\mathbf{x}$, where $\mathbf{A} \in \mathbb{R}^{n\times n}$ has n_c zero real eigenvalues and n_s negative real eigenvalues and n_u positive real eigenvalues. The centre subspace of this linear system is NHIM, and this persists under small nonlinear perturbations using Fenichel's theorem (see [109] for a detailed explanation). This invariant manifold is called the centre manifold.

Moreover, the centre manifold is locally represented as a graph; the stable-unstable subspace defined by the Jacobian of the vector field at equilibrium is a function of the centre subspace (see [49] for the proof), near the equilibrium as the following theorem.

Theorem 2.1. ***Centre manifolds for ODEs*** *[49]*
Consider a C^k-smooth system

$$\begin{aligned} \dot{\mathbf{x}} &= \mathbf{B}\mathbf{x} + \mathbf{f}(\mathbf{x}, \mathbf{y}), \\ \dot{\mathbf{y}} &= \mathbf{C}\mathbf{y} + \mathbf{g}(\mathbf{x}, \mathbf{y}), \end{aligned} \tag{2.11}$$

where $\mathbf{x} \in \mathbb{R}^{n_c}$, $\mathbf{y} \in \mathbb{R}^{n_s+n_u}$, *and* $\mathbf{f}(\mathbf{x}, \mathbf{y})$, $\mathbf{g}(\mathbf{x}, \mathbf{y})$ *have neither constant nor linear terms. Suppose that the matrix* $\mathbf{B} \in \mathbb{R}^{n_c \times n_c}$ *has* n_c *critical eigenvalues (i.e. eigenvalues with* $Re\,(\lambda) = 0$*) and* $\mathbf{C} \in \mathbb{R}^{n_h \times n_h}$ *has* n_u *eigenvalues with* $Re\,(\lambda) > 0$, n_s *eigenvalues with* $Re\,(\lambda) < 0$, *and* $n_h = n_s + n_u$.

The system 2.11 has a locally defined invariant manifold

$$W^c = \{(\mathbf{x}, h^c(\mathbf{x})) : \mathbf{x} \in \mathbb{R}^{n_c}, \| \mathbf{x} \| \leq \varepsilon\}$$

where $\varepsilon > 0$ *is sufficiently small and* $h^c : \mathbb{R}^{n_c} \to \mathbb{R}^{n_s+n_u}$ *is a* C^k*-map satisfying*

$$h^c(0) = 0,\ D_{\mathbf{x}} h^c(0) = 0.$$

The centre manifold theorem is particularly useful when studying bifurcation problems with control parameter λ as in Chapter 5. We can add $\dot{\lambda} = 0$ to Eq. (2.11) and compute the parametrised version of the central manifold as in the following example.

Example 2.2. ***Families of centre manifolds*** *[49]*
Consider a smooth parameter-dependent system of ODEs

$$\begin{aligned} \dot{\mathbf{x}} &= P(\mathbf{x}, \mathbf{y}, \lambda) \\ \dot{\mathbf{y}} &= Q(\mathbf{x}, \mathbf{y}, \lambda), \end{aligned} \tag{2.12}$$

where $\mathbf{x} \in \mathbb{R}^{n_c}$, $\mathbf{y} \in \mathbb{R}^{n_s+n_u}$, $\lambda \in \mathbb{R}^m$ *and suppose that 2.12 coincides with 2.11 at* $\lambda = 0$

The system 2.12 has a family of invariant manifolds, locally representative for small $\| \lambda \|$ *as*

$$W^c_\lambda = \{(\mathbf{x}, w(\mathbf{x}, \lambda)) : \xi \in \mathbb{R}^{n_c},\ \| \mathbf{x} \| \leq \varepsilon\}$$

where $\varepsilon > 0$ *is sufficiently small and* $w : \mathbb{R}^{n_c} \times \mathbb{R}^m \to \mathbb{R}^{n_s+n_u}$ *is smooth. Moreover,* $w(\mathbf{x}, 0) = h^c(\mathbf{x})$*, i.e.* W^c_0 *conincides with a centre manifold* W^c *at* $\lambda = 0$.

Example 2.2 shows that we can reduce the dynamics to parametrised centre manifold W^c_λ near $\lambda = 0$. For example, assume that the three-dimensional system has a supercritical Hopf at $\lambda = 0$. We can reduce the dynamics to a planar system on a parametrised centre manifold W^c_λ as in Fig. 2.1.

As in Fig. 2.1, the centre manifold is an attracting manifold for systems with Hopf bifurcation. Therefore, the centre manifold has the core information of the system, as a final steady-state

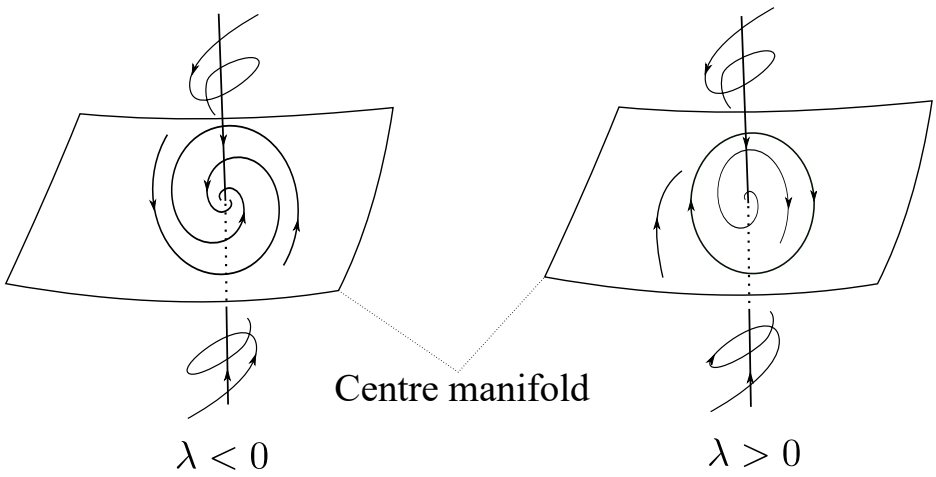

Figure 2.1: Phase portrait of a three-dimensional system near the supercritical Hopf bifurcation at $\lambda = 0$

response is on the centre manifold in these systems. In Chapter 4, a mechanistic model with Hopf bifurcation is reduced to a parametrised centre manifold as in Example 2.2. The mathematical model is defined on the centre manifold in Chapter 5, where we use the existence of the centre manifold as domain knowledge.

2.3.2 Invariant manifold of a forced mechanical systems

A mathematical model of harmonically forced mechanical systems with an asymptotically stable equilibrium also has invariant manifolds called spectral submanifolds (SSMs). We can understand spectral submanifolds as perturbed NHIM of the linear modal subspace spanned by the slowest decaying modes (see [36] for details). However, SSMs exist not only for the slowest decaying modes, as any modal subspace persists under small nonlinear perturbations under conditions called non-resonance conditions. We will briefly introduce the theoretical background of SSMs and how we derive reduced-order models of harmonically forced systems.

Let us consider a mathematical model of a mechanical system of N degrees of freedom with a single harmonic external force represented as

$$\begin{aligned} &\mathbf{M}\ddot{\mathbf{q}} + \mathbf{C}\dot{\mathbf{q}} + \mathbf{K}\mathbf{q} + \mathbf{f}_n(\mathbf{q}, \dot{\mathbf{q}}) = \varepsilon \mathbf{f}_{ext}(\Omega t), \quad \mathbf{q} \in \mathbb{R}^N \\ &\mathbf{f}_n = \mathcal{O}(|\mathbf{q}|^2, |\mathbf{q}||\dot{\mathbf{q}}|, |\dot{\mathbf{q}}|^2), \quad \mathbf{f}_{ext}(\Omega t) = \mathrm{Re}\,(\mathbf{f}^d e^{i\Omega t}). \end{aligned} \tag{2.13}$$

where $\mathbf{M} \in \mathbb{R}^{N\times N}$ is a symmetric positive definite matrix that models the mass, $\mathbf{K} \in \mathbb{R}^{N\times N}$ is the stiffness matrix, $\mathbf{C} \in \mathbb{R}^{N\times N}$ is the damping matrix. $\mathbf{f}_n$ is the nonlinear force that characterises nonlinear stiffness and nonlinear damping that is at least quadratic in order; therefore, $\mathbf{q} = 0$ is an equilibrium. $\mathbf{f}^d \in \mathbb{C}^N$ is a direction vector with phase information of the

external force $\mathbf{f}_{ext}$, which is a single harmonic function. Note that a more general mechanical setting considering the gyroscopic effect, follower forces, and multi-harmonic excitation can be considered as in [36].

Transforming Eq. (2.13) into a functional system of first-order ODEs offers more information on the system by extending the state space as $\mathbf{x} = [\mathbf{q}, \dot{\mathbf{q}}]^T$ and defining the matrices as

$$\mathbf{A} = \begin{bmatrix} 0 & \mathbf{I} \\ -\mathbf{M}^{-1}\mathbf{K} & -\mathbf{M}^{-1}\mathbf{C} \end{bmatrix}, \quad \mathbf{G}(\mathbf{x}) = \begin{bmatrix} 0 \\ -\mathbf{M}^{-1}\mathbf{f}_n(\mathbf{x}) \end{bmatrix}, \quad \mathbf{G}_{ext}(\phi) = \begin{bmatrix} 0 \\ -\mathbf{M}^{-1}\mathbf{f}_{ext}(\phi) \end{bmatrix} \tag{2.14}$$

where $\phi = \Omega t$. Eq. (2.13) is transformed into a first-order autonomous ODE using Eq. (2.14) as

$$\begin{aligned} \dot{\mathbf{x}} &= \mathbf{A}\mathbf{x} + \mathbf{G}(\mathbf{x}) + \varepsilon \mathbf{G}_{\text{ext}}(\phi) \\ \dot{\phi} &= \Omega, \end{aligned} \tag{2.15}$$

where $n = 2N$, $A \in \mathbb{R}^n \times \mathbb{R}^n$ is a matrix with all eigenvalues having negative real part, $\mathbf{G} : \mathbb{R}^n \to \mathbb{R}^n$ is a nonlinear function with $\mathbf{G}(0) = 0$, $D\mathbf{G}(0) = 0$, harmonic force $\mathbf{G}_{ext} : \mathbb{S}^1 \to \mathbb{R}^n$ is a trigonometric function having a form $\mathbf{a}\cos(\phi) + \mathbf{b}\sin(\phi)$ where $\mathbf{a}, \mathbf{b} \in \mathbb{R}^n$, and $\phi \in \mathbb{S}^1$ is a phase variable of the harmonic force, $\varepsilon \ll 1$ is a small parameter.

We are interested in the solutions of Eq. (2.15) that have the form $(K(\phi), \phi) \in \mathbb{R}^n \times \mathbb{S}^1$. This type of solution is called an invariant torus, and note that periodic solutions of Eq. (2.15) also form an invariant torus. For $\varepsilon = 0$, the invariant torus of Eq. (2.15) is $\{0\} \times \mathbb{S}^1$ and the study of the persistence of this invariant torus under perturbations and invariant manifolds attached to the invariant torus is in [38], which states that invariant manifolds attached to $\{0\} \times \mathbb{S}^1$ persist under small perturbation made by $\varepsilon \mathbf{G}_{\text{ext}}(\phi)$ in Eq. (2.15).

Haller [36] restated Haro's result in [38] for systems described in the form of Eq. (2.15) under non-resonance conditions. Let us define a spectral subspace, a vector space spanned by the eigenvectors of $\mathbf{A}$, as

$$E = span\{\mathbf{v}_1, \bar{\mathbf{v}}_1, \ldots, \mathbf{v}_s, \bar{\mathbf{v}}_s\}, \tag{2.16}$$

where $\mathbf{v}_i$ denotes the eigenvector of i-th eigenvalue, s is the number of modes contained in E, and the upper bar denotes the complex conjugate. Note that since A is a real matrix, the spectral subspace is always spanned by a pair of complex conjugate eigenvectors.

We can parameterise an invariant manifold of Eq. (2.15) that is tangent to the spectral subspace of dimension $2s$ of $\mathbf{A}$, E, with its spectrum $\lambda_1, \bar{\lambda}_1, \ldots, \lambda_s, \bar{\lambda}_s$ at the origin when $\varepsilon = 0$. Under nonresonance conditions, a perturbed invariant manifold ($\varepsilon > 0$) is a $2s + 1$ dimensional manifold where the phase variable ϕ is an additional parameterisation variable, as stated in the following theorem.

Theorem 2.2. ***Invariant manifolds of harmonically forced systems*** *[14, 36]*
Consider a spectral subspace E and assume that the low-order nonresonance conditions are

$$< m, \lambda >_E \neq \lambda_l, \quad \lambda_l \notin Spect(E), \quad 2 \leq |m| \leq \sigma(E) \tag{2.17}$$

hold for all eigenvalues of λ_l of $\mathbf{A}$ that are outside the spectrum of E, where $Spect(E) := \{\lambda_1, \ldots, \lambda_s\}$, $|m| := m_1 + \ldots + m_s$ and

$$< m, \lambda >_E := m_1\lambda_1 + \ldots + m_s\lambda_s, \quad where \quad \lambda_1, \ldots, \lambda_s \in Spect(E), \tag{2.18}$$

and spectral quotient $\sigma(E)$ is defined as

$$\sigma(E) = Int\Big(\frac{Re(\lambda_{min})}{\max_{j=1,\ldots,s} Re(\lambda_j)}\Big), \tag{2.19}$$

where λ_{min} denotes the eigenvalue corresponding to the fastest decaying mode, and λ_j corresponds to the eigenvalues corresponding to spectral subspace E and $Int(\cdot)$ denote the integer part of the real number.

Then the following statements hold:

1. *A parameterisation $\mathbf{W} : \mathbb{R}^{2s} \times \mathbb{S}^1 \to \mathbb{R}^{2N}$ of the invariant manifold W can be approximated in a neighbourhood of the origin as a polynomial in the parameterisation variable $\mathbf{z} \in \mathbb{R}^{2s}$ and the phase variable $\phi \in \mathbb{S}^1$, i.e.*

$$\mathbf{x} = \mathbf{W}(\mathbf{z}, \phi).$$

2. *Reduced dynamics, $\mathbf{R}(\mathbf{z}, \phi)$, defined in an open neighbourhood of $\mathbf{x} = 0$, such that the invariance condition*

$$\mathbf{A}\mathbf{W}(\mathbf{z}, \phi) + \mathbf{G}(\mathbf{W}(\mathbf{z}, \phi)) + \varepsilon\mathbf{G}_{ext}(\phi) = D_{\mathbf{z}}\mathbf{W}(\mathbf{z}, \phi)\mathbf{R}(\mathbf{z}, \phi) + D_{\phi}\mathbf{W}(\mathbf{z}, \phi)\Omega \tag{2.20}$$

   holds. Therefore, the dynamics on the invariant manifold is governed by

$$\dot{\mathbf{z}} = \mathbf{R}(\mathbf{z}, \phi).$$

3. *The parametrisation, $\mathbf{W}(\mathbf{z}, \phi)$, as well as the reduced dynamics $\mathbf{R}(\mathbf{z}, \phi)$ persists under small vector field perturbations.*

4. *W is at least of class $C^{\sigma(E)+1}$ with respect to $\mathbf{x}$.*

Theorem 2.2 indicates that we can reduce the dimension of Eq. (2.15) to a reduced system if we study the invariant manifold $\mathbf{W}$ and the reduced dynamics $\mathbf{R}$ under nonresonance condition Eq. (2.17).

The parameterisation of the invariant manifold $\mathbf{W}$ can be chosen by balancing Eq. (2.20). Dynamics of the invariant manifold reduce our computational load when studying the frequency response near resonance. This can be done by choosing a two-dimensional E that corresponds to a single mode spectral subspace as in [14].

As we consider small ε, the parameterisation of the invariant manifold, $\mathbf{W}$, and the reduced dynamics, $\mathbf{R}$, is represented as [14]

$$\mathbf{W}(\mathbf{z},\phi) = \mathbf{W}_0(\mathbf{z}) + \sum_{l=1}^{\infty} \varepsilon^l \mathbf{W}_l(\mathbf{z},\phi), \tag{2.21}$$

$$\mathbf{R}(\mathbf{z},\phi) = \mathbf{R}_0(\mathbf{z}) + \sum_{l=1}^{\infty} \varepsilon^l \mathbf{R}_l(\mathbf{z},\phi), \tag{2.22}$$

where the subscript l of $\mathbf{W}$ and $\mathbf{R}$ indicate the order of expansion of ε. $\mathbf{W}_0$, $\mathbf{R}_0$ corresponds to the invariant manifold and the reduced dynamics of the autonomous system with $\varepsilon = 0$ in Eq. (6.1). The perturbed invariant manifolds and the reduced dynamics $\mathbf{W}_l$, $\mathbf{R}_l$ are also expressed in polynomial expansion as

$$\mathbf{W}_l(\mathbf{z},\phi) = \sum_{m=0} \mathbf{w}_l^m(\phi)\mathbf{z}^m, \tag{2.23}$$

$$\mathbf{R}_l(\mathbf{z},\phi) = \sum_{m=0} \mathbf{r}_l^m(\phi)\mathbf{z}^m, \tag{2.24}$$

using this expression, $\mathbf{W}$ and $\mathbf{R}$ are expressed upto $\mathcal{O}(\varepsilon|\mathbf{z}|,\varepsilon^2)$ accuracy as

$$\mathbf{W}(\mathbf{z},\phi) = \mathbf{W}_0(\mathbf{z}) + \varepsilon\mathbf{w}_1^0(\phi) + \mathcal{O}(\varepsilon|\mathbf{z}|,\varepsilon^2), \tag{2.25}$$

$$\mathbf{R}(\mathbf{z},\phi) = \mathbf{R}_0(\mathbf{z}) + \varepsilon\mathbf{r}_1^0(\phi) + \mathcal{O}(\varepsilon|\mathbf{z}|,\varepsilon^2), \tag{2.26}$$

The parameterisation variable $\mathbf{z} = [z, \bar{z}]^T$ can be chosen as a complex conjugate pair $z, \bar{z} \in \mathbb{C}$. Using $\mathbf{W}_0$ being tangent to the corresponding eigenspace [36], $\mathbf{R}_0(\mathbf{z})$ is expressed as

$$\mathbf{R}_0(\mathbf{z}) = \begin{bmatrix} \lambda_l z \\ \bar{\lambda}_l \bar{z} \end{bmatrix} + \mathcal{O}(\mathbf{z}^2). \tag{2.27}$$

In principle, it is possible to model $\mathbf{R}_0(\mathbf{z})$ as a polynomial up to $j_0 - 1$ order if the following nonresonance condition is satisfied [97].

$$\lambda_l^{s_1}\bar{\lambda}_l^{s_2} \neq \lambda_l, \bar{\lambda}_l, \; j_0 \leq s_1 + s_2 \leq \sigma(E), \tag{2.28}$$

However, in low damping system (i.e. $|\lambda_l| \simeq 1$), the non-resonance condition approximately fails. Therefore, a broad domain of validity near the equilibrium can be ensured by looking for $\mathbf{R}_0(\mathbf{z})$ as (see [97] for details)

$$\mathbf{R}_0(\mathbf{z}) = \begin{pmatrix} \lambda_l z + \beta_3 z^2 \bar{z} + \beta_5 z^3 \bar{z}^2 + \dots \\ \bar{\lambda}_l \bar{z} + \bar{\beta}_3 z \bar{z}^2 + \bar{\beta}_5 z^2 \bar{z}^3 + \dots \end{pmatrix} \tag{2.29}$$

The typical reduced-order modelling problem is solving Eq. (2.20) using Eqs. (2.25) and (2.29) as a functional form of $\mathbf{W}$ and $\mathbf{R}$. The unknown coefficients of Eq. (2.25) are calculated in each polynomial order by balancing each side of Eq. (2.20).

Using Eqs. (2.25) and (2.29) reduced dynamics on the invariant manifold can be transformed into a polar coordinate system $z = \rho e^{i\theta}$ as [14]

$$\begin{aligned} \dot{\rho} &= a(\rho) + \Gamma \sin(\psi), \\ \dot{\theta} &= b(\rho) + \Gamma/\rho \cos(\psi), \\ \dot{\phi} &= \Omega, \end{aligned} \tag{2.30}$$

where $a(\rho)$ is the unforced vector fields of the reduced dynamics in the radius direction, $b(\rho)$ is the unforced vector fields of the reduced dynamics in the angle direction, Γ is the forcing amplitude projected in the tangent direction of the invariant manifold, $\psi = \theta - \phi$, $\phi = \Omega t$ is the phase of the external forcing. Transforming the reduced dynamics to Eq. (2.30) makes computing periodic solutions and stability properties much more convenient (see [14, 21]).

Theorem 2.2 is the theoretical background of the data-driven modelling scheme developed in Chapter 6, where we use the existence of the SSM as domain knowledge. We generate an input-output map to train reduced dynamics on SSM from a rotationally symmetric parameterisation of W in Chapter 6 motivated by Eq. (2.30). Rotationally symmetric means that the reduced dynamic is invariant under rotational transformations applied to $\mathbf{z}$.

2.4 Topological equivalence and the normal form

We call two dynamical systems topologically equivalent if one system is transformable to other systems via an invertible transformation. This transformation preserves the invariant sets and the stability properties.

By letting $\phi_{\mathbf{F}}^t$ be a flow direction by $\dot{\mathbf{x}} = \mathbf{F}(\mathbf{x})$, we can define the topological equivalence as follows.

Definition 2.3. Topological equivalence [27]
Two flows $\phi_{\mathbf{F}}^t : \mathbf{X} \to \mathbf{X}$ and $\phi_{\mathbf{G}}^\tau : \mathbf{Y} \to \mathbf{Y}$ are **t**opologically equivalent if there is a homeomorphism $\mathbf{h} : \mathbf{X} \to \mathbf{Y}$ and a continuous time-rescailing function $\tau(\mathbf{y}, t)$, satisfying $\partial\tau/\partial t > 0 \forall \mathbf{y} \in \mathbf{Y}$, such that

$$\phi_{\mathbf{F}}^{t} = \mathbf{h}^{-1} \circ \phi_{\mathbf{G}}^{\tau} \circ \mathbf{h}$$

We can use the topological equivalent dynamical system to study bifurcation qualitatively by deriving a simple type of equation called normal form. Normal forms of bifurcation involving periodic solutions are typically converted to polar coordinates. For example, the principal idea is to transform a trajectory of a periodic solution into a circle where the periodic solution corresponds to a fixed point in polar coordinates. We typically need a coordinate transformation, parameter rescaling, and time rescaling to remove unnecessary terms, the so-called secular terms. The following example shows how we can study a bifurcation problem using a normal form of the Hopf bifurcation.

Example 2.3. ***Normal form of the Hopf bifurcation*** *[49]*
Suppose a two-dimensional system

$$\dot{\mathbf{x}} = \mathbf{F}(\mathbf{x}, \alpha), \quad \mathbf{x} \in \mathbb{R}^2, \ \alpha \in \mathbb{R} \tag{2.31}$$

with smooth $\mathbf{F}$*, has for all sufficiently small* $|\alpha|$ *the equilibrium* $\mathbf{x} = 0$ *with eigenvalues of the Jacobian of* $\mathbf{F}$ *in the associated equilibrium*

$$\lambda_{1,2}(\alpha) = \mu(\alpha) \pm i\omega(\alpha)$$

where $\mu(0) = 0$*,* $\omega(0) = \omega_0 > 0$*. Let the following conditions be satisfied:*

(1) The first Lyapunov coefficient is nonzero (see [49] for definition).

(2) $\dot{\mu}(0) \neq 0$*.*

Then, there are invertible coordinate and parameter changes and a time rescaling transforming Eq. (2.31) into

$$\begin{aligned} \dot{y}_1 &= \beta y_1 - y_2 \pm (y_1^2 + y_2^2) y_1 \\ \dot{y}_2 &= \beta y_2 + y_1 \pm (y_1^2 + y_2^2) y_2, \end{aligned} \tag{2.32}$$

where $\pm$ *sign depends on the sign of the first Lyapunov coefficient. We can easily calculate the amplitude of the LCO of Eq. (2.32) as* $\sqrt{|\beta|}$*, and the stability of this LCO is stable when the first Lyapunov coefficient is negative.*

The normal form gives us qualitative information about the flow near the invariant sets, as shown in Example 2.3. Topological equivalence is the essential concept used in Chapters 4 and 5 in data-driven modelling of reduced dynamics on the invariant manifold. In Chapter 4, we used a normal form to parameterise the bifurcation diagram using the unknown coefficients in Chapter 4. In Chapter 5, the bifurcation structure revealed from the CBC is used to set topologically equivalent dynamics on the centre manifold as the basis model.

CHAPTER 3

Experimental bifurcation analysis

In this chapter, we

- introduce control-based continuation (CBC) that tracks bifurcation in a physical experiment,
- discuss the CBC scheme for tracking periodic solutions of harmonically forced mechanical systems with numerical and experimental demonstration,
- develop the CBC scheme for tracking LCOs in self-excited systems with numerical and experimental demonstration.

3.1 Introduction

Tracking parameter-dependent periodic solutions in an experiment provide extensive dynamic information about a system. For example, the frequency sweep of a mechanical system under harmonic forcing gives a frequency response curve with critical information about the resonance behaviour. Similarly, a flutter test of an aerofoil in a wind tunnel can reveal a bifurcation diagram when a system has a supercritical Hopf bifurcation. However, there can be unstable periodic responses when a system's nonlinearity is not negligible. In the case of a flutter test, unstable LCOs have critical information about the system when there is a subcritical Hopf bifurcation. A simple parameter sweep experiment does not provide sufficient information about the system.

Previous investigations have revealed the potential benefit of exploiting unstable LCOs when estimating the parameters of a mathematical model. For instance, the amplitudes of unstable LCOs were used to constrain model parameter optimisation and improve model

predictions in [100]. However, without control, the authors could not directly measure the unstable LCOs, and the LCO amplitudes were estimated by applying perturbations to the system and identifying the smallest perturbation leading to a transition to the large-amplitude stable LCOs. In [87], a conceptually-similar perturbation approach was used to estimate the unstable LCOs of autogyro blades. A simple model was then developed and analysed using the numerical continuation to qualitatively reproduce the experimentally measured bifurcation diagrams. Besides the lack of accurate measurements of the unstable LCOs, the estimation of the unstable LCOs using perturbations does not scale well with the number of DOFs in the system and would not be applicable to complex systems.

Feedback control can be used to measure unstable LCOs in an experiment. Time-delayed feedback control [72, 94] uses a signal proportional to $x(t) - x(t - T)$, where x is one of the measurable state variables, to stabilise the periodic solution with a period T. The measured periodic response is identical to the uncontrolled system when the controller is properly designed. The major application of time-delayed feedback control is controlling chaos [73, 74] where a large number of unstable periodic orbits are embedded. Some of these unstable periodic orbits may correspond to the desired response where delayed feedback stabilises [72]. However, dealing with delayed signals in an experiment can cause numerous problems, such as controller stability issues and memory. Furthermore, correctly determining the period T to use can be a significant challenge, especially for non-autonomous systems.

For forced systems, Phase-locked loops (PLL) are used to maintain the $\pi/2$ phase lag between the fundamental harmonic of the excitation and the response [69], which allows fast measurement of backbone curves and unstable periodic responses. However, PLLs are applicable only for the experiment of harmonically forced systems where the phase of the harmonic force parametrises the response curve.

CBC is an experimental method that relies on feedback control to steer the response of a physical system towards behaviours of interest and then uses path-following techniques to track their evolution as experimental parameters (such as wind speed) are changed. The fundamental idea behind CBC is to make the control system *non-invasive* such that observed responses correspond to the behaviour of the underlying uncontrolled experiment of interest [8, 95]. If properly designed, the feedback controller makes unstable orbits stable and hence observable.

Here, we will show that CBC offers a systematic methodology to identify unstable LCOs. However, the CBC method has until now been only applied to a wide range of harmonically-forced systems, including nonlinear energy harvesters [6, 7, 83], a bilinear oscillator [17, 18, 30] and a nonlinear beam with harmonically-coupled modes [85], and the notable difference with the previous application is that the system considered in this chapter is autonomous. As such, the system's oscillation frequency is not determined by an external excitation and is a priori unknown. Therefore, we suggest a new CBC scheme, phase-plane CBC (PP-CBC), which uses a planar curve parametrised by phase angle as a control target.

In Section 3.2, we first introduce the CBC scheme for forced systems with numerical and experimental examples. We develop two parametrisation methods for setting a control target in PP-CBC in Section 3.3 with numerical examples to show the robustness of the developed PP-CBC method. Finally, an experimental demonstration of PP-CBC is presented in Section 3.3.3.

3.2 CBC scheme for harmonically forced systems

In this section, we will discuss CBC schemes for harmonically forced systems that have been applied to many applications. We will first discuss the fundamental concept of stabilising unstable periodic solutions. Then, we will explain a simplified strategy to track the bifurcation diagram of forced systems where we can avoid Newton iterations.

A harmonically forced system can be represented as

$$\dot{\mathbf{x}} = \mathbf{F}(\mathbf{x}) + \mathbf{f}_{ext}(A\cos(\Omega t) + B\sin(\Omega t) + u(t)) \tag{3.1}$$

where Ω is the excitation frequency, $\mathbf{f}_{ext} \in \mathbb{R}^N$ is the direction unit vector of the force, and $u(t)$ is a feedback control in the form of

$$u(t) = k_p(x^*(t) - x(t)) + k_d(\dot{x}^*(t) - \dot{x}(t)), \tag{3.2}$$

where $x, \dot{x}$ are measured scalar signals, $x^*(t)$ is the control target, $\dot{x}^*(t)$ is the time-derivative of the control target, k_p is the proportional control gain, k_d is the derivative control gain.

We can set the bifurcation parameter of the system as $\lambda = \Omega$ or $\lambda = \gamma$ where $\gamma = \sqrt{A^2 + B^2}$ is the amplitude of the harmonic force. We refer to a bifurcation diagram as a frequency response curve (FRC) when the bifurcation parameter is the frequency Ω, or an S-curve when the bifurcation parameter is forcing amplitude γ.

The choice of $x^*(t)$ that makes the controller noninvasive, i.e. $u(t) = 0$, is a solution of zero problem defined by input-output map $x^*(t) - x(t) = 0$, where $x^*(t)$ is the input and $x(t)$ is the output over one period of oscillation. Specifically, we can discretise the input-output map by projecting $x^*(t)$ and $x(t)$ to the truncated Fourier series of first $q+1$ modes as

$$\begin{aligned} x(t) &= A_0/2 + \sum_{j=1}^{q} A_j\cos(j\Omega t) + B_j\sin(j\Omega t), \\ x^*(t) &= A_0^*/2 + \sum_{j=1}^{q} A_j^*\cos(j\Omega t) + B_j^*\sin(j\Omega t). \end{aligned} \tag{3.3}$$

We can rewrite $x^*(t) - x(t) = 0$ using Fourier coefficients as

$$\mathbf{p}(\mathbf{p}^*) - \mathbf{p}^* = 0, \tag{3.4}$$

where $\mathbf{p}^* = [A_0^*, \ldots, A_q^*, B_1^*, \ldots, B_q^*]^T$ is the control target vector and $\mathbf{p} = [A_0, \ldots, A_q, B_1, \ldots, B_q]^T$ is the response vector.

We can solve Eq. (3.4) using zero problem-solving methods such as Newton-like methods [91] or Picard iteration [5] when the control gains k_p and k_d are suitably chosen.

Newton-like methods are essential while tracking Frequency Response Curves (FRCs) when a bistable region exists. However, Newton-like methods are extremely time-consuming in the experiment since we need to evaluate the Jacobian every step. We will explain a continuation scheme where Newton-like methods can be replaced by Picard iterations that work on S-curves.

3.2.1 Measuring S-curves using CBC

An S-curve is a bifurcation diagram plotted using $\gamma = \sqrt{A^2 + B^2}$ as a bifurcation paramter. The CBC continuation problem for S-curves is formulated as Eq. (3.4). To avoid this issue in the presence of folds in the solution branch, we add the arclength equation to Eq. (3.4) given by

$$\tilde{\mathbf{p}}_j^T[\mathbf{p}_j - \mathbf{p}_{j-1}] + \tilde{\gamma}_j[\gamma_j - \gamma_{j-1}] = \Delta s, \quad \text{for} \quad j \geqq 2, \tag{3.5}$$

where $\mathbf{p}_j$ is the vector of Fourier coefficients of the j-th step defined in Eq. (3.4). $\mathbf{p}_{j-1}$ is the Fourier coefficient of the previous point of continuation with forcing amplitude γ_{j-1}, $\tilde{\mathbf{p}}_j = \mathbf{p}_{j-1} - \mathbf{p}_{j-2}$ is the direction vector calculated from two previous experiments and $\tilde{\gamma}_j = \gamma_{j-1} - \gamma_{j-2}$ is the searching direction of the control parameter γ, and Δs is the arclength parameter that user sets for a continuation problem. The zero problems can be solved in the experiment using Newton's methods as in [91].

The zero-problem of S-curves (Eq. (3.4)) is relatively easy to solve as we can use Picard (fixed-point) iterations for the higher harmonics as in [11]. First, initial control target is set as $\mathbf{p}_{j,0}^* = \mathbf{p}_{j-1}^*$ where $\mathbf{p}_{j-1}^*$ is the successful control target vector of last step, $j-1$-th step, of S-curve continuation and subscript 0 of $\mathbf{p}_{j,0}^*$ indicates the step number of iteration for noninvasive control. We can use a simple trick to avoid zero problems for main harmonic components by computing γ as

$$\begin{aligned}
\hat{A} =& A + k_p\pi_1 \circ (\mathbf{P}_{j+1,0}^* - \mathbf{P}_{j+1,0}) + \Omega k_d \pi_{q+1} \circ (\mathbf{P}_{j+1,0}^* - \mathbf{P}_{j+1,0}),\\
\hat{B} =& B + k_p\pi_{q+1} \circ (\mathbf{P}_{j+1,0}^* - \mathbf{P}_{j+1,0}) - \Omega k_d \pi_1 \circ (\mathbf{P}_{j+1,0}^* - \mathbf{P}_{j+1,0}),\\
\gamma =& \sqrt{\hat{A}^2 + \hat{B}^2},
\end{aligned} \tag{3.6}$$

where we treat the control error's main harmonic components as the forcing amplitude increase.

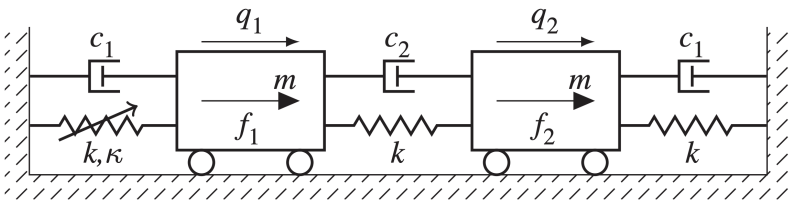

Figure 3.1: The modified Shaw-Pierre example in [14]. $m = 1$, $k = 1$, $c_1 = \sqrt{3}$, $c_2 = 0.003$ and $\kappa = 0.5$. W is mass, k is linear stiffness coefficient, c is linear damping coefficient, κ is quadratic stiffness coefficient, $f_1 = A\cos(\Omega t)$. $f_2 = 0$

The fixed-point problem for noninvasive control is defined by

$$\pi_k \circ \mathbf{p}^*_{j+1} - \pi_k \circ \mathbf{p}_{j+1} = 0, \quad \text{for} \quad k = 1, \ldots, 2q+1, \tag{3.7}$$

where π_k is a projection function to a k-th component of a vector. Eq. (3.7) can be solved via Picard (fixed point) iteration in the experiment by updating the control target for the higher harmonics as

$$\pi_k \circ \mathbf{p}^*_{j+1,l} = \pi_k \circ \mathbf{p}_{j+1,l-1} \quad \text{for} \quad k \in \{0, 1, \ldots, 2q+1\}/\{1, q+1\}, \tag{3.8}$$

where iteration step, l, is increased until the zero tolerance is satisfied. However, Eq. (3.7) for $k = 1, q+1$, which corresponds to the main harmonic components, is not solvable via Picard (fixed point) iteration. This is the main reason for introducing a scheme in Eq. (3.6).

We can plot the S-curve by plotting $(\gamma(\Lambda), \Lambda)$ where we assume the amplitude of periodic responses, Λ, can be approximated using main harmonic components as $\Lambda = \sqrt{A^2 + B^2}$. the Following example shows a numerical demonstration of the CBC scheme explained in this subsection.

Example 3.1. ***Numerical demonstration of measuring S-curve using CBC***
The CBC is applied to a system in Fig. 3.1. The feedback control, $u(t)$, is added to this system to the same point f_1 is applied as

$$\begin{aligned} u(t) &= k_p(q^*(t) - q_1(t)) + k_d(\dot{q}^*(t) - \dot{q}_1(t)), \\ q^*(t) &= A^*_0/2 + \sum_{j=1}^{5} A^*_j \cos(j\Omega t) + B^*_j \sin(j\Omega t), \end{aligned} \tag{3.9}$$

where $k_p = k_d = 0.01$ and the Picard iteration is applied as in Eq. (3.8) to achieve noninvasiveness at higher harmonics with zero tolerance 10^{-5}. We can obtain S-curves as in Fig. 3.2 by updating the forcing amplitude as in Eq. (3.6). We can see the agreement of the S-curve is good with the S-curve of the system without CBC computed using numerical continuation. Moreover,

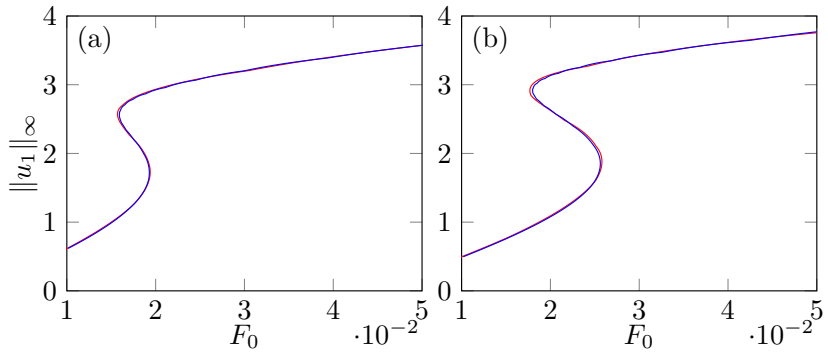

Figure 3.2: S-curves of systems studied in Example 3.1. (a) $\Omega = 1.004$. (b) $\Omega = 1.005$. (—) a system without CBC computed using spectral collocation methods, (—) system with CBC computed using numerical integration and algorithm explained in Section 3.2.1.

we can increase the accuracy of the CBC scheme by increasing the number of harmonics used in Eq. (3.9).

3.2.1.1 CBC experiment of an electromagnetic oscillator

This subsection provides CBC experimental results of a forced electromagnetic system [82] (see Fig. 3.3 for the schematic and picture) that are used in data-driven modelling of Chapter 5.

A thin steel cantilever beam plate is clamped to an armature at one end (see Fig. 3.3), where two sets of neodymium magnets are attached at the other end of the plate. The experimental system is a single-degree-of-freedom (SDOF) oscillator which is fixed vertically to avoid transverse deformation to the plate thickness. The permanent magnets induce electromagnetic force that affects the stiffness of the system. The stiffness characteristic is softening at the low amplitudes and hardening at the higher amplitudes. The stiffness characteristic of the system can be adjusted by changing the air gap between the magnet and the iron coil. However, only one configuration of the air gap experimental result is considered here. We track the frequency response of this system with the variation of the amplitude of the base excitation amplitude, γ, with fixed forcing frequency, Ω, which is called S-curves.

Base and plate tip displacements are measured using laser sensors, Omron ZX2-LD50 and Omron ZX2-LD100. The electromagnetic oscillator is excited at the base using a shaker, model APS 113, controlled by the Maxon ADS-50/10- 4QDC controller.

Control gains are selected as $k_p = 0.065$ and $k_d = 0.005$ for the CBC control. During the CBC, the zero problems were solved for higher harmonics as in Eq. (3.8), and the forcing amplitude was updated using Eq. (3.6) to measure S-curves. Fig. 3.4 shows an S-curve measured at forcing frequency 20.3 Hz. The fold bifurcation point of the S-curve shown in Fig. 3.4 is located at the forcing amplitude 0.4 where the lower stable branch is connected with the unstable higher branch. At forcing amplitude 0.05, the lower unstable branch is connected

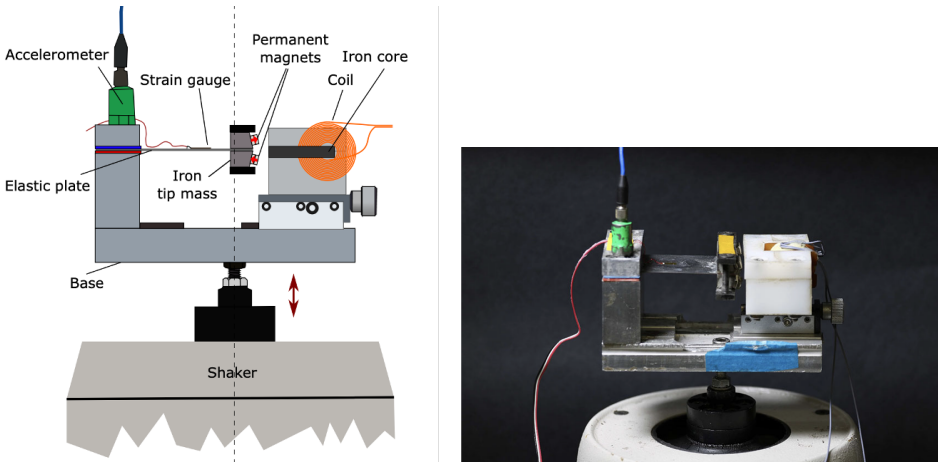

Figure 3.3: Nonlinear electromagnetic oscillator (Left) Schematic (Right) Picture [11]

with the stable higher branch. The proposed CBC scheme makes unstable periodic response observable and tracks the curve using the method introduced in Eq. (3.6). Fig. 3.5 shows 24 S-curves which are measured at different forcing frequencies using the scheme explained in this section.

S-curves can be used to identify unknown parameters of the system as in [11] where the S-curve is parametrised using unknown parameters of a polynomial function using multiple time scale methods. In [11], a model was identified for a single S-curve, and training with multiple S-curves is discussed in [10]. From studies [10, 11], it is shown that the polynomial functions are not flexible enough to capture multiple S-curves and using a neural network improves the model flexibility to capture a wider range of frequency responses with multiple S-curves. However, it is shown in [10] that it is challenging to deal with overfitting issues using a neural network as the model does not give smooth S-curves.

In Chapter 5, we identify a model from 24 S-curves using kernel ridge regression, where we can deal with model complexity much more easily than the neural network. Also, we can extract critical information, such as the backbone curve, from the model, which is discussed in detail in Chapter 5.

3.3 CBC scheme for self-excited systems

For forced systems, the control target for CBC is parametrised using the phase of the harmonic force as in Eq. (3.3). However, there are no phase signals in the experiment of self-excited systems. We suggest an alternative geometric way of setting a control target for stabilising periodic solutions of self-excited systems, called phase-plane CBC (PP-CBC). The main idea of PP-CBC is to set a curve parametrised by an angle of a two-dimensional plane as a control target.

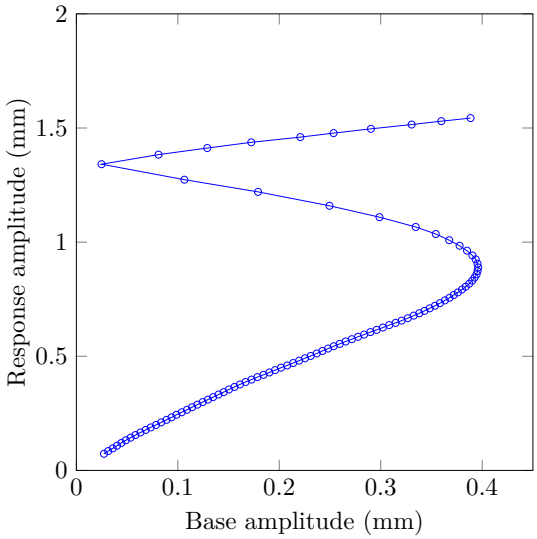

Figure 3.4: S-curve measured using CBC on an electromagnetic oscillator at forcing frequency 21.3 Hz

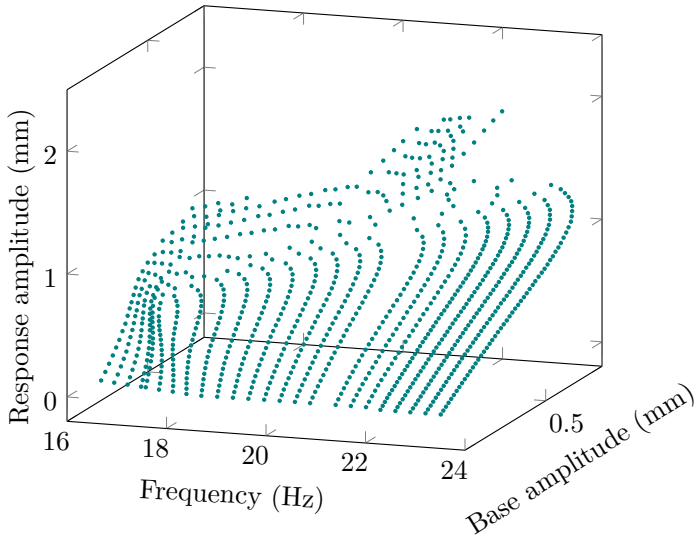

Figure 3.5: 24 S-curves measured using CBC on an electromagnetic oscillator

Let $\Gamma \subset \mathbb{R}^N = \{\Phi^t(\gamma_0) | 0 \leq t < T_\Gamma\}$ be a trajectory of a periodic solution with period T_Γ, evolution map Φ^t of the system, and γ_0 is a point of a periodic solution. PP-CBC stabilises the LCO by projecting Γ to a two-dimensional phase plane (x_1, x_2) where we assume x_1, x_2 are two measurable state variables.

Two-dimensional coordinates have a smooth transition map between Cartesian coordinates, (x_1, x_2), and the polar coordinates, (r, ϕ), in $\mathbb{R}^2/\{(0,0)\}$. The polar representation, (r, ϕ), is not unique; however, we aim to parametrise the control target in a plane using ϕ of suitably

chosen polar coordinates.

We assume Γ projected to (x_1, x_2) coordinate, $\Gamma_\pi \subset \mathbb{R}^2$, is a polar curve. The polar curve is a parameterizable curve using the angle $\phi \in [0, 2\pi)$ defined in polar coordinate (r, ϕ). This assumption generally means we can parametrise Γ_π as

$$\Gamma_\pi = \{(\hat{x}_1(\phi), \hat{x}_2(\phi)) | \phi \in [0, 2\pi)\}, \tag{3.10}$$

where $\hat{x}_1, \hat{x}_2$ are 2π-periodic functions

$$\begin{aligned} \hat{x}_1(\phi) =& o_1 + r(\phi)\cos(\phi), \\ \hat{x}_2(\phi) =& o_2 + r(\phi)\sin(\phi), \end{aligned} \tag{3.11}$$

where (o_1, o_2) is the origin of polar coordinates.

The fundamental idea of PP-CBC is feeding $k_p(\hat{x}_1(\phi) - x_1) + k_d(\hat{x}_2(\phi) - x_2)$ to the system to stabilise the unstable LCOs where ϕ is a function of x_1 and x_2. To explain the concept of PP-CBC in detail, we need to discuss the parameterisation method of $\hat{x}_1$ and $\hat{x}_2$ before introducing zero-problem-solving strategies for PP-CBC.

Here, we suggest two different ways of parametrisation of Γ_π. One is an elliptic curve, and the other one is a general polar curve. The following subsections will explain two different parametrisation methods with numerical examples.

3.3.1 Elliptic projected phase-plane case

When the trajectory of Γ_π is an ellipse centered at (o_1, o_2), width A, height $|A\omega|$. The ellipse also can be parameterised as in Eq. (3.11); however, we can further simplify the parametrisation in this case by introducing linear transformation on original coordinates (x_1, x_2) as

$$\begin{aligned} x_1 &\mapsto o_1 + x_1/\omega \\ x_2 &\mapsto o_2 + x_2, \end{aligned} \tag{3.12}$$

then transform Cartesian coordinates to polar coordinates where we can parameterize the ellipse using ϕ as

$$\begin{aligned} \hat{x}_1(\phi) &= o_1 + A\cos(\phi) \\ \hat{x}_2(\phi) &= o_2 + \omega A\sin(\phi), \end{aligned} \tag{3.13}$$

where angle is represented as $\phi = \tan^{-1}\left(\frac{x_2 - o_2}{\omega(x_1 - o_1)}\right)$ (see Fig. 3.6).

The elliptic parametrisation can be used when the projected trajectory of the periodic solution is an elliptic curve. This parametrisation is particularly useful when we project periodic

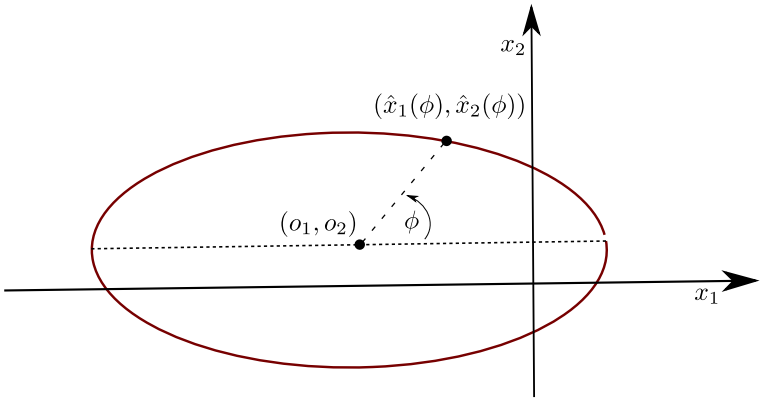

Figure 3.6: Parametrisation of an elliptic curve

solutions that can be approximated to a single harmonic function, i.e. $x = o_1 + A\cos(\omega t)$, to a plane of a state variable and the time derivative of a state-variable $(x, \dot{x})$. In this case, we can parameterize the elliptic curve as

$$\begin{aligned} \hat{x}_1(\phi) &= o_1 + A\cos(\phi), \\ \hat{x}_2(\phi) &= -\omega A \sin(\phi), \end{aligned} \tag{3.14}$$

which is useful in many practical experiments. Note that the sign of ω governs the direction of the rotation along the elliptic trajectory with respect to the direction of the angle.

We can stabilise the original uncontrolled system by adding control force as

$$\begin{aligned} \dot{\mathbf{x}} =& \mathbf{F}(\mathbf{x}, \lambda) + \mathbf{e}_c(k_p(\hat{x}_1(\phi) - x_1) + k_d(\hat{x}_2(\phi) - x_2)), \\ \phi =& \tan^{-1}\left(\frac{x_2 - o_2}{\omega(x_1 - o_1)}\right), \end{aligned} \tag{3.15}$$

where $\mathbf{F}(\mathbf{x}, \lambda)$ defines the vector field of the uncontrolled system, λ is a control parameter, $\mathbf{e}_c$ is the direction vector of the control force and k_p, k_d are the control gains. We can successfully measure unstable periodic orbits when k_p, k_d are appropriately chosen and $|k_p(\hat{x}_1(\phi) - x_1) + k_d(\hat{x}_2(\phi) - x_2)| \ll 1$.

The following example shows PP-CBC stabilising an unstable LCO of a subcritical Hopf normal form.

Example 3.2. ***PP-CBC applied to a Hopf normal form***

Suppose PP-CBC is added to the subcritical Hopf normal form as

$$\begin{aligned} \dot{u}_1 &= \lambda u_1 - u_2 + u_1(u_1^2 + u_2^2) + k_p(r_0\cos\phi - u_1) + k_d(r_0\sin\phi - u_2), \\ \dot{u}_2 &= \lambda u_2 + u_1 + u_2(u_1^2 + u_2^2), \end{aligned} \tag{3.16}$$

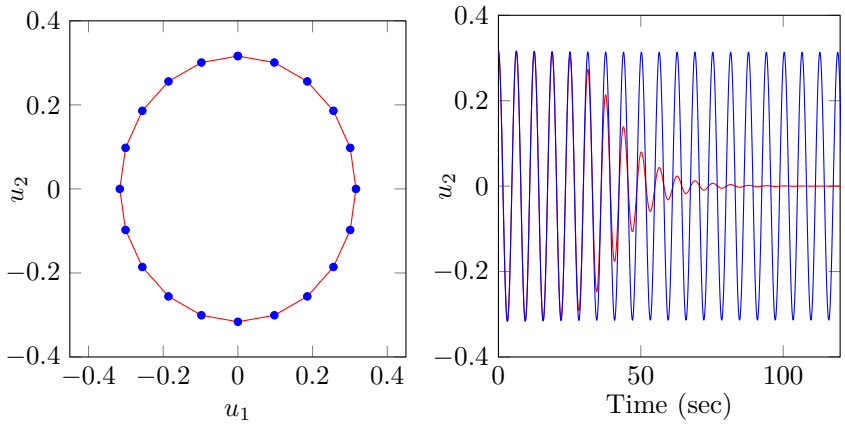

Figure 3.7: Stabilising control using PP-CBC (left) phase portrait of a system with PP-CBC and uncontrolled system computed via Fourier collocation method. (—) a system without CBC, (•) system with CBC (right) time series of system with PP-CBC and uncontrolled system computed via numerical integration. (—) system without CBC, (—) system with CBC

where $\phi = \tan^{-1}\left(\frac{u_2}{u_1}\right)$. $r_0 = \sqrt{-\lambda}$ *is the amplitude of the LCO of the Hopf normal form.*

At $\lambda = -0.1$, *we can stabilise the LCO of the uncontrolled system using* $k_p = 0.5$, $k_d = -0.5$. *Fig. 3.7 (Left) compares the phase-portrait of the system with PP-CBC and the system without PP-CBC computed by the Fourier collocation methods, and Fig. 3.7 (Right) shows the time-series comparison computed by numerical integration. Computing the periodic solution of the system with CBC and the uncontrolled system with the collocation method is identical. However, we can see that the error in numerical integration perturbs the solution from the unstable periodic solutions for the uncontrolled system. In contrast, the system with CBC persists in its periodic motion in numerical integration, suggesting the periodic solution is stabilised.*

In physical experiments, the parametric representation of Γ_π is priori unknown. Therefore, we suggest a scheme to achieve noninvasive control in the experiment by solving a zero problem. Let $\mathbf{p}^* = [A^*, \omega^*, o_1^*, o_2^*]^T$ which is the control target vector that sets the control target as

$$\begin{aligned} x_1^*(\phi) &= o_1^* + a^* \cos(\phi), \\ x_2^*(\phi) &= o_2^* + \omega^* A^* \sin(\phi), \end{aligned} \tag{3.17}$$

where $\phi = \tan^{-1} \frac{x_2 - o_2^*}{\omega^*(x_1 - o_1^*)}$. The response is also assumed to be an elliptic curve as

$$\begin{aligned} x_1(\phi) &= o_1 + a \cos(\phi), \\ x_2(\phi) &= o_2 + \omega A \sin(\phi), \end{aligned} \tag{3.18}$$

where we can find the elliptic coefficients of the response $\mathbf{p} = [A, \omega, o_1, o_2]^T$ by fitting the measured signal with Eq. (3.18) as in [35] using least squares fitting.

We can achieve noninvasiveness when the measured elliptic curve is approximately the same with the control target as

$$\mathbf{p}(\mathbf{p}^*) - \mathbf{p}^* = 0. \tag{3.19}$$

We can compute root of Eq. (3.19) using zero-problem solving methods discussed in Section 3.2.

In practice, we can use Picard iteration for the noninvasive control when we project the periodic solution to $(x, \dot{x})$ and when x is represented as a single harmonic signal. The parameters o_1^* and ω^* are first found separately from A^* using Picard iterations. At steady state, o_1^* and ω^* are set equal to o_1 and ω calculated from the measured response. This procedure is repeated until it converges, i.e., the difference between measured and target parameter values is lower than the zero tolerance. Different coefficient values are imposed to determine the unknown coefficient A^*, and the control error $\Xi = A^* - A(A^*)$ is observed. The value for which the control error and, thus, the control signal become zero indicates the presence of a periodic orbit of the underlying uncontrolled experiment.

3.3.2 General polar curve projected phase-plane case

We can also apply PP-CBC to track unstable periodic orbits for more complex shaped polar curves. Since Γ_π is a closed curve, we have 2π-periodic $\hat{r}(\phi) = \sqrt{\hat{x}_1(\phi)^2 + \hat{x}_2(\phi)^2}$. Without loss of generality, we assume (o_1, o_2) is the origin. Therefore, $\hat{r}(\phi)$ can be represented as a truncated Fourier series

$$\hat{r}(\phi) \simeq \hat{a}_0 + \sum_{j=1}^{n_h} \hat{a}_j \cos(j\phi) + \sum_{j=1}^{n_h} \hat{b}_j \sin(j\phi), \tag{3.20}$$

where we assume n_h number of harmonics sufficiently represent $\hat{r}(\phi)$, and $\hat{a}_0$, $\hat{a}_j$, $\hat{b}_j$ for $j = 1, \ldots, n_h$ are Fourier coefficients. Similarly, we can set a control target using the Fourier coefficient and add PP-CBC as

$$\dot{\mathbf{x}} = \mathbf{F}(\mathbf{x}, \lambda) + \mathbf{e}_c(k_p(r^*(\phi)\cos\phi - x_1) + k_d(r^*(\phi)\sin\phi - x_2)), \tag{3.21}$$

$$r^*(\phi) = a_0^* + \sum_{j=1}^{n_h} a_j^* \cos(j\phi) + \sum_{j=1}^{n_h} b_j^* \sin(j\phi), \tag{3.22}$$

where $\phi = \tan^{-1}\left(\frac{x_2}{x_1}\right)$, $r = \sqrt{x_1^2 + x_2^2}$, k_p, k_d are control gains.

Now, we can define a zero-problem of PP-CBC as

$$\Phi(r^*(\phi)) - \Phi(r(\phi)) = 0, \quad r = \sqrt{{x_1}^2 + {x_2}^2} \tag{3.23}$$

where Fourier projection is defined as $\Phi(R) : C_p([0, 2\pi], \mathbb{R}) \to \mathbb{R}^{2n_h+1} = [a_0, \ldots, a_{n_h}, b_1, \ldots, b_{n_h}]$ and

$$a_0 = \frac{1}{2\pi} \int_0^{2\pi} R \mathrm{d}\theta, \tag{3.24a}$$

$$a_n = \frac{1}{\pi} \int_0^{2\pi} R \cos(n\theta) \mathrm{d}\theta \qquad \text{for } n = 1, 2, \ldots, n_h, \tag{3.24b}$$

$$b_n = \frac{1}{\pi} \int_0^{2\pi} R \sin(n\theta) \mathrm{d}\theta \qquad \text{for } n = 1, 2, \ldots, n_h. \tag{3.24c}$$

By adding pseudo-arclength equation Eq. (3.5) to Eq. (3.23), we have a typical continuation of zero-problem. The following example shows the numerical demonstration of PP-CBC using a general polar curve as a control target.

Example 3.3. ***PP-CBC applied to a unsteady flutter model***

In this example, we apply PP-CBC to an unsteady aeroelastic flutter model presented in Appendix A. In this model, the state-space vector is composed of heave, the velocity of heave, pitch, the velocity of pitch and two aeroelastic variables to describe an aeroelastic force. The wind speed is a control parameter of the model, and the model has a subcritical Hopf bifurcation at the wind speed 18.3 *m/sec. PP-CBC is applied to a unsteady flutter model as*

$$\begin{aligned} \dot{\mathbf{z}} &= \mathbf{B}(\mu)\mathbf{z} + \mathbf{N_0}(\mathbf{z}) + \mathbf{e}_c(k_p(r^*(\phi)\cos\phi - x_1) + k_d(r^*(\phi)\sin\phi - x_2)), \\ r^*(\phi) &= a_0^* + \sum_{j=1}^{n_h} a_j^* \cos(j\phi) + \sum_{j=1}^{n_h} b_j^* \sin(j\phi), \end{aligned} \tag{3.25}$$

where $\mathbf{e}_c = [0, 1, 0, 0, 0, 0]^T$*, and the first equation without the control force is presented in Appendix A. We use* $k_p = k_d = -100$*,* $n_h = 10$ *and perform a numerical continuation of the zero problems defined by Eq. (3.23) and the pseudo-arclength equation.*

We can see that the system with PP-CBC and without control has an identical bifurcation diagram in the unstable branch emerging from a Hopf point as in Fig. 3.8. Also, PP-CBC does not modify the original phase-portrait but stabilises the unstable response as shown in Fig. 3.9.

Floquet multipliers in Fig. 3.9 are computed from the variational equation of Eq. (3.25) which can be written as

$$\dot{\mathbf{v}} = \mathbf{F}_{\mathbf{z}}(\mathbf{z}^*(t))\mathbf{v}, \tag{3.26}$$

where $\mathbf{z}^*(t)$ *is the noninvasive periodic solution, i.e. solution that makes the control force zero, of Eq. (3.25),* $\mathbf{v} \in \mathbb{R}^6$ *is a small perturbation from the periodic solution and* $\mathbf{F}_{\mathbf{z}}$ *is the linearisation of the vector field of Eq. (3.25). Floquet multipliers are the eigenvalues of the fundamental matrix solution of Eq. (3.1) at the period of the periodic solution with identity matrix as the initial condition [49]. Also, Floquet multipliers are identical to the eigenvalues of the linearised Poincare map constructed at one of the points on the periodic solution which*

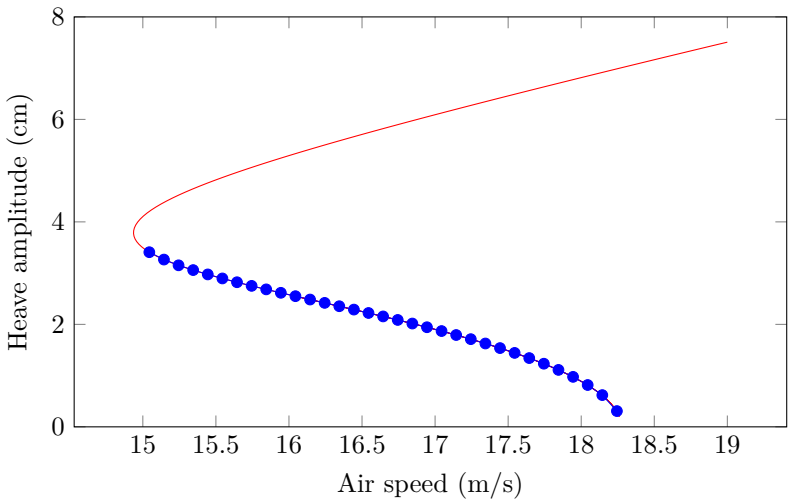

Figure 3.8: Bifurcation diagram of PP-CBC compared with numerical continuation of the uncontrolled system. (—) numerical continuation of system without CBC, (●) numerical continuation of system with CBC.

allows us to study stability of the periodic solutions. As PP-CBC is an autonomous system, trivial Floquet multiplier with value 1 where the eigenvector corresponds to the velocity vector always exists.

Floquet multipliers computed from the variational equation derived from Eq. (3.1), CBC of harmonically forced system, are strictly inside the unit circle. The Poincare section of Eq. (3.1) can be fully described when the state space is extended by the phase of the harmonic force $\phi = \Omega t$*. It should be noted that the system, Eq. (3.1), is autonomous when the state space extended by* ϕ*. The Floquet multipliers of the variational equation of Eq. (3.1) do not include the trivial Floquet multiplier of the extended state space as the Poincare section corresponds to* $\{(\mathbf{x}, \phi) : \phi = \theta_0\}$ *where* θ_0 *is one of the phase points of the harmonic external force. Physically, CBC of a harmonically forced system makes all directions of the unextended state space stable whereas the PP-CBC makes only the direction transverse the periodic solution stable.*

3.3.3 PP-CBC of a flutter rig

This subsection will show an experimental example of PP-CBC applied to a flutter rig in a wind tunnel experiment. This experiment uses parametrisation method discussed in Section 3.3.1. First, we will explain the experimental setting of PP-CBC on a flutter rig. The PP-CBC algorithm used in the experiment is presented in Section 3.3.3.2. In Section 3.3.3.3, the result of the PP-CBC experiment is explained.

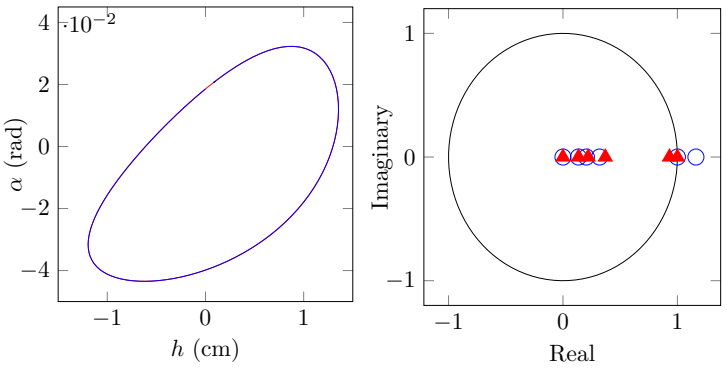

Figure 3.9: Comparison between system with PP-CBC vs system without control at the wind speed 16 m/s (Left) phase portrait. (—) numerical continuation of system without CBC, (—) numerical continuation of system with CBC, (right) Floquet multipliers. (▲) system with CBC (○) system without CBC.

3.3.3.1 Description of the flutter rig

The flutter rig is shown in Fig. 3.10 comprises a NACA-0015 wing profile rigidly attached to a stainless steel shaft, supported at both ends by rotational bearings mounted on supporting plates that are constrained to move vertically by a linear bearing system. As such, the experiment has two mechanical degrees of freedom: pitch (rotational motion) and heave (vertical motion). The semi-chord of the aerofoil is 150 mm with a span of 600 mm.

In the heave direction, linear springs are connected between the supporting plates and the outer frame. In the pitch direction, torsional springs are connected between the shaft and the supporting plates. Both sets of springs provide approximately linear restoring forces in their respective directions. In the pitch direction, there are additional leaf springs connecting the shaft and the supporting plates; these leaf springs provide a hardening nonlinearity, mimicking potential interface effects at the root of the aerofoil.

The leaf springs also add an element of safety to the design, limiting the large amplitude motions that can occur during flutter oscillations.

The dimensions of the flutter rig are such that the wing profile fits in the principal section of the University of Bristol low-turbulence wind tunnel; the supporting plates and outer frame lie outside it (see Fig. 3.10(a)).

Additional control forces are applied in the heave direction by using an APS 113 electro-seis long-stroke electrodynamic shaker connected by a flexible stinger to one of the the supporting plates.

The experiment is instrumented with an Omron ZX1-LD300 laser displacement sensor focused on a supporting plate to capture the heave motion and an RLS AksIM 18 bit absolute magnetic encoder fitted on the shaft to capture the pitch motion. Additionally, accelerometers are mounted on various components, but their outputs are not used in this analysis.

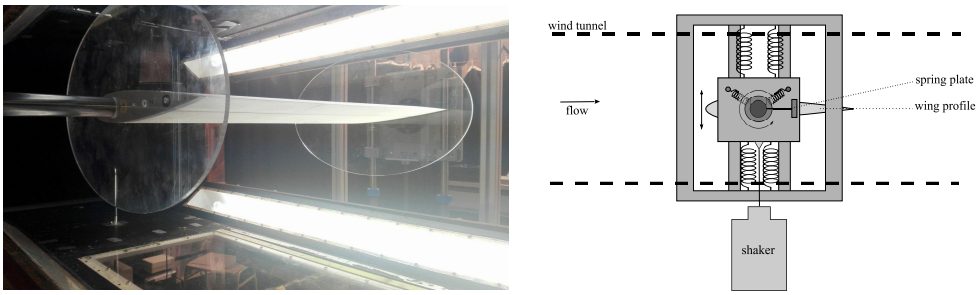

Figure 3.10: The nonlinear flutter rig with a rigid NACA-0015 wing profile and two mechanical degrees of freedom (pitch and heave; that is, rotational and vertical motion). Panel (a) is a photograph of the experiment looking towards the trailing edge of the aerofoil; the airflow is from left to right. Panel (b) is a schematic drawing of the experiment.

Real-time control and data acquisition are performed using a Beaglebone Black single-board computer equipped with an analogue IO cape (18 bit ADC and 16 bit DAC) operating at a sample rate of 5 kHz. Details of the control system are in rtc repository.

The bifurcation of the flutter rig is highly sensitive to the setup of the rig. For example, the stiffness of the leaf spring, which can be modified by the position of the clamp, and the friction in the pitch and the heave direction affect the flutter speed and the flutter frequency. Therefore, feedback control gains to stabilise the system depend on the experimental setup and the temperature of the mechanical parts of the flutter rig. Two big challanges in the experimental setting is making the flutter rig to have a desired Hopf bifurcation and finding the sutiable control gains that stabilises the unstable solutions.

3.3.3.2 Algorithm for tracking LCOs of a flutter rig

The control law is given by

$$u(t) = k_p(z^*(t) - z(t)) + k_d(\dot{z}^*(t) - \dot{z}(t)), \tag{3.27}$$

where $k_p = 15.0$ and $k_d = -0.05$ are the proportional and derivative gains of the controller, $z^*(t)$ is the control reference and $\dot{z}^*(t)$ its time derivative, $z(t)$ is the heave displacement, and $\dot{z}(t)$ its time derivative. We use the parametrisation method presented in Eq. (3.14) for control targets, $z^*(t)$ and $\dot{z}^*(t)$, as

$$z^*(t) = o_1^* + A^* \cos\phi \qquad \text{and} \qquad \dot{z}^*(t) = -A^*\omega^* \sin\phi, \tag{3.28}$$

where

$$\phi = \tan^{-1}\left(\frac{-\dot{z}(t)}{\omega^*(z(t) - o_1^*)}\right). \tag{3.29}$$

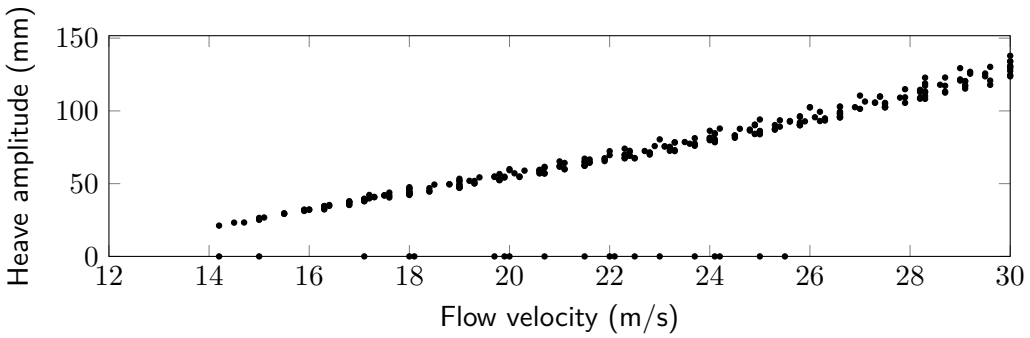

Figure 3.11: The response of the flutter rig in open-loop mode (no control active) measured across multiple days. Bistable behaviour is evident for flow velocities between approximately 14 m/s and 25 m/s where a stable limit cycle oscillation in heave and pitch coexists with a stable equilibrium.

Eq. (3.28) locks the phase of the control reference onto the phase of the measured response. The problem is now to find the unknown control reference parameters o_1^*, A^*, and ω^* such that a non-invasive control signal is achieved (as explained in Eq. (3.19)). As a single-harmonic signal is assumed, geometric coefficients o_1, ω can be calculated from the measured time series $z(t)$. Rather than using Newton's method, which requires a time-consuming Jacobian calculation in the experiment, we use the Picard iteration (fixed-point iteration) in this experiment discussed in Section 3.3.1.

3.3.3.3 PP-CBC results

Open-loop tests were initially performed to investigate the dynamics of the system. Fig. 3.11 shows the response of the system for wind velocities ranging from approximately 14 m/s to 27 m/s. Starting around 14 m/s and increasing the wind velocity, the equilibrium position of the system is stable, and the system does not exhibit any oscillation. After 24 m/s, the equilibrium loses stability, and the system starts to exhibit large-amplitude LCOs. These LCOs are sustained and grow in amplitude for larger wind velocities. Decreasing the wind velocity from 27 m/s, LCOs are maintained until approximately 17 m/s, after which the system returns to its equilibrium position. The sudden transition to finite-amplitude LCOs around 24 m/s and the existence of a range of wind velocities for which stable equilibria and LCOs coexist indicate the presence of a subcritical Hopf bifurcation and a branch of unstable oscillations separating the equilibria from the stable LCOs. A saddle-node bifurcation is also present at approximately 15 m/s.

We now apply CBC to measure the system's LCOs in the range of wind velocities where the system is bistable. As changes to the wind velocity cannot be made automatically and introduce substantial transient effects, we investigate the dynamics of the system for a range of fixed wind velocities. At each wind velocity, the amplitude of the control target A^* is increased iteratively.

Between two increments, the dynamics is left to settle and the control error $\Xi = A^* - A$ is measured. Figure Fig. 3.14(a) shows the control error obtained for 3 repetitions of the same experiment at 15.6 m/s. When the control error crosses zero, which consistently happens between the first two data points, the control signal is noninvasive, and the response of the controlled system corresponds to the response of the underlying uncontrolled experiment. The control error Ξ crosses zero in the low-amplitude, unstable LCO and in the high-amplitude, stable LCO. The solution observed in Fig. 3.14 corresponds to unstable LCO.

Fig. 3.15 (a) shows heave amplitude of the LCOs and Fig. 3.15 (b) shows pitch amplitude of the LCOs measured at four different wind velocities. Unstable and stable LCOs are represented in red (○) and blue (●), respectively. As in Fig. 3.14(a), the evolution of the oscillation frequency across the bifurcation diagram is relatively small (Fig. 3.15(c)).

Fig. 3.16 shows some of the raw time series recorded for the heave motion (—) and Fig. 3.17 shows the raw time series of the pitch motion. For the tolerance considered (1.8 mm), the control reference signals (—) are in excellent agreement with the measured responses, which further shows that the control signal can be considered non-invasive. A further demonstration of the small relative magnitude of the control signal was obtained experimentally by switching off the controller on one of the stable LCOs. This did not affect the dynamic response of the system, as shown in 3.18(a). Repeating the same process on one of the unstable LCOs shows that the dynamics of the system evolve towards the stable equilibrium of the underlying uncontrolled system (Fig. 3.18(b)). After repeating the process several times, we observed that the uncontrolled response could either evolve towards the stable equilibrium or the stable LCOs of the underlying uncontrolled system. Observing both types of responses shows that the identified unstable LCO lies at (or very close to) the boundary between the two coexisting stable behaviours and that the LCOs were accurately captured by PP-CBC.

The same procedure to stabilise unstable LCOs was applied in a different setting with replaced leaf springs, which is in Fig. 3.19. We can see that the flutter speed and frequency were changed by replacing the leaf spring.

3.4 Conclusion

In this chapter, we discussed the CBC scheme to measure bifurcation diagrams in an experiment. We first discussed the CBC scheme to measure S-curves of harmonically forced mechanical systems. We show from a numerical experiment that the Picard iteration scheme to avoid Newton iteration in the experiment is robust. Also, we show an experimental example with an electromagnetic oscillator where CBC is applied to measure S-curves.

The main novelty of this chapter is developing a CBC scheme for self-excited systems, which is fundamentally different from previously developed CBC schemes. The developed PP-CBC uses the geometric parametrisation of the LCO trajectory as a control target for non-invasive

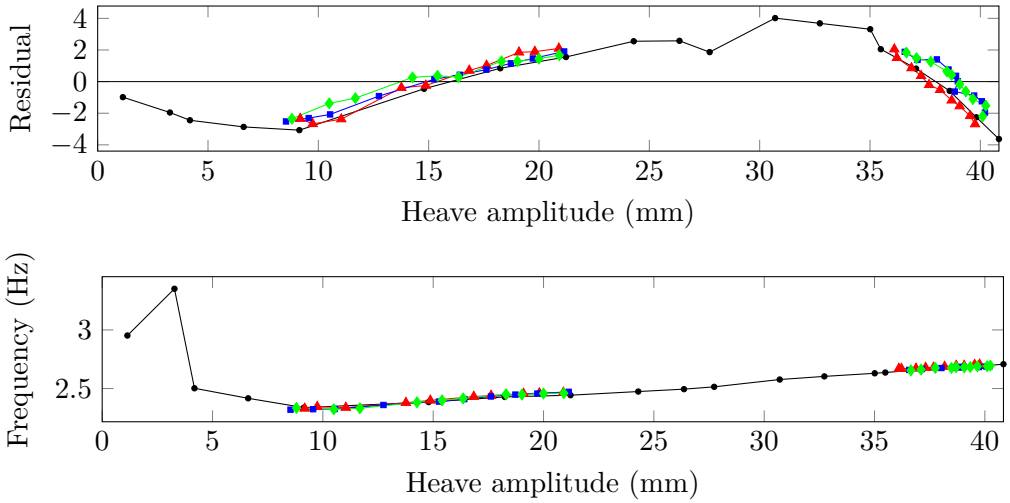

Figure 3.12: Residuals of PP-CBC in amplitude at Wind speed = 17.5 m/s

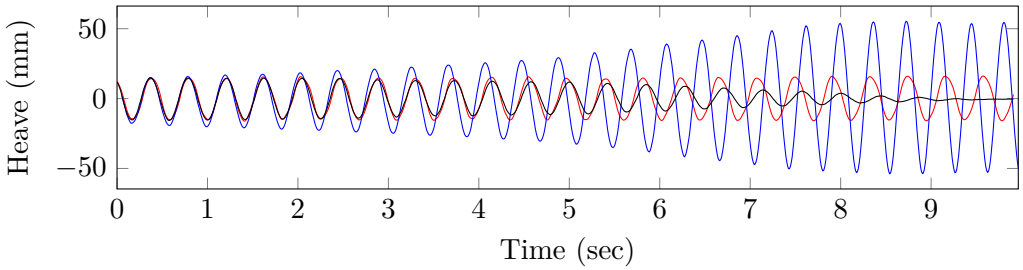

Figure 3.13: Measurement of time series at Wind speed = 20 m/s

control. We suggest two parametrisation methods– elliptic and general polar curves– that show robustness in numerical simulations. We also show an experimental demonstration result of PP-CBC applied to a flutter rig in a wind tunnel experiment.

Acknowledgement

The original concept of PP-CBC was developed by David Barton and Irene Tartaruga. Initial experimental rig setup of PPCBC was developed by Irene Tartaruga, David Barton, and Djamel Rezgui.

Data and code availability

All measured data and the code used in the experiment are stored in the University of Bristol research data storage.

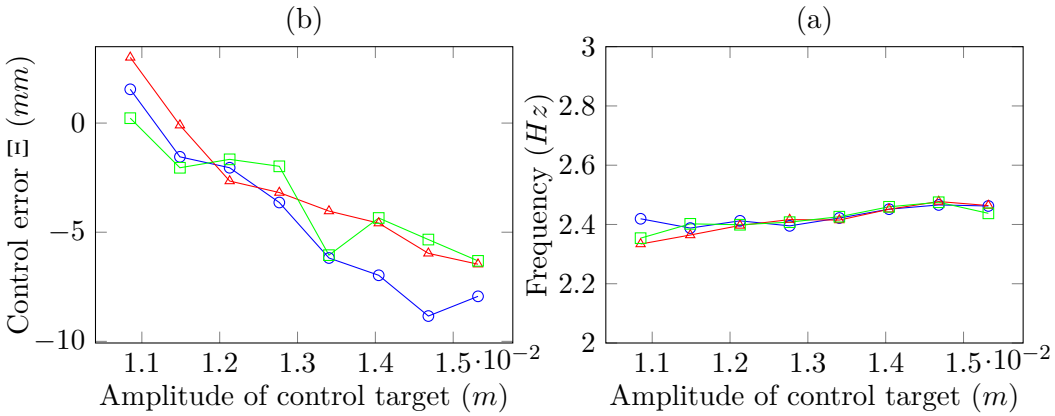

Figure 3.14: Multiple measurements of frequency and control error of phase-locked periodic solutions at different amplitudes of control target (a) frequency and (b) error.

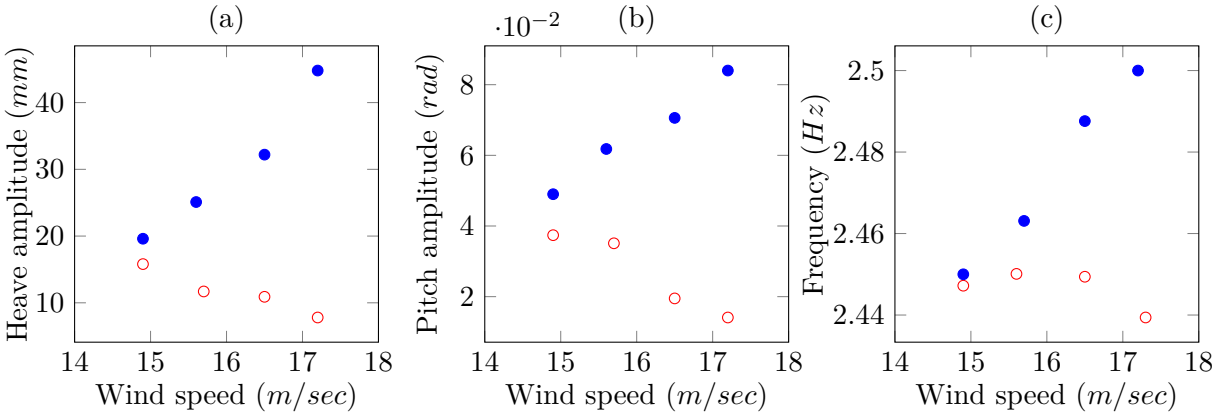

Figure 3.15: CBC results (a) Heave amplitude of LCO (mm), (b) Pitch amplitude of LCO (rad), (c) Frequeny of LCO (Hz). (●) is measured stable LCO and (○) is the measured unstable LCO.

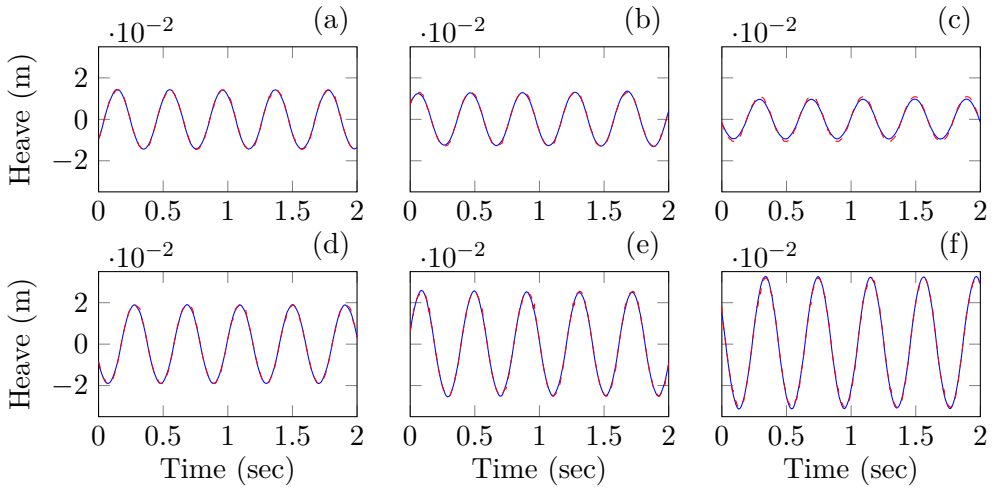

Figure 3.16: Heave amplitude of measured LCOs (a) Unstable LCO (U=14.9 m/sec), (b) Unstable LCO (Wind speed = 15.6 m/sec), (c) Unstable LCO (Wind speed = 6.5 m/sec), (d) Stable LCO (Wind speed = 14.9 m/sec), (e) Stable LCO (Wind speed = 15.6 m/sec), (f) Stable LCO (Wind speed = 16.5 m/sec). (——) is the heave response of the rig, (——) is the control target.

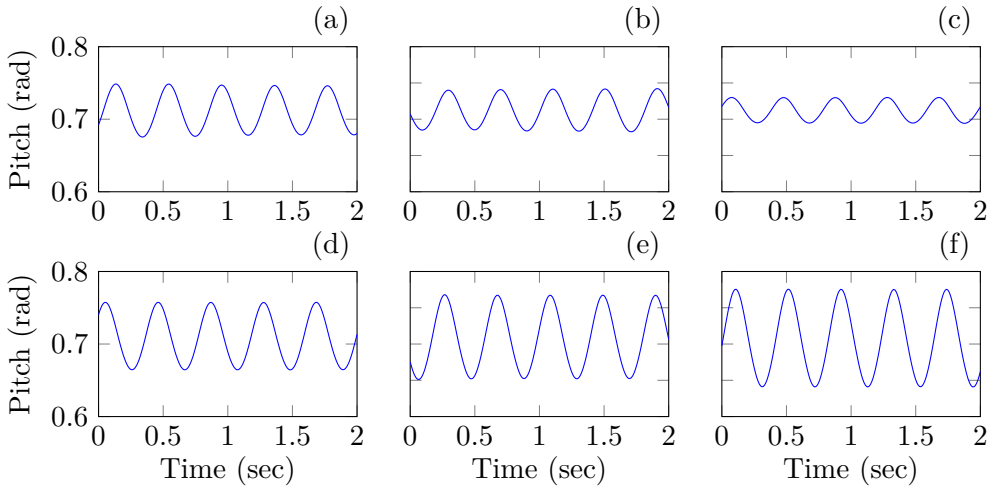

Figure 3.17: Pitch amplitude of measured LCOs (a) Unstable LCO (U=14.9 m/sec), (b) Unstable LCO (Wind speed = 15.6 m/sec), (c) Unstable LCO (Wind speed = 16.5 m/sec), (d) Stable LCO (Wind speed = 14.9 m/sec), (e) Stable LCO (Wind speed = 15.6 m/sec), (f) Stable LCO (Wind speed = 16.5 m/sec).

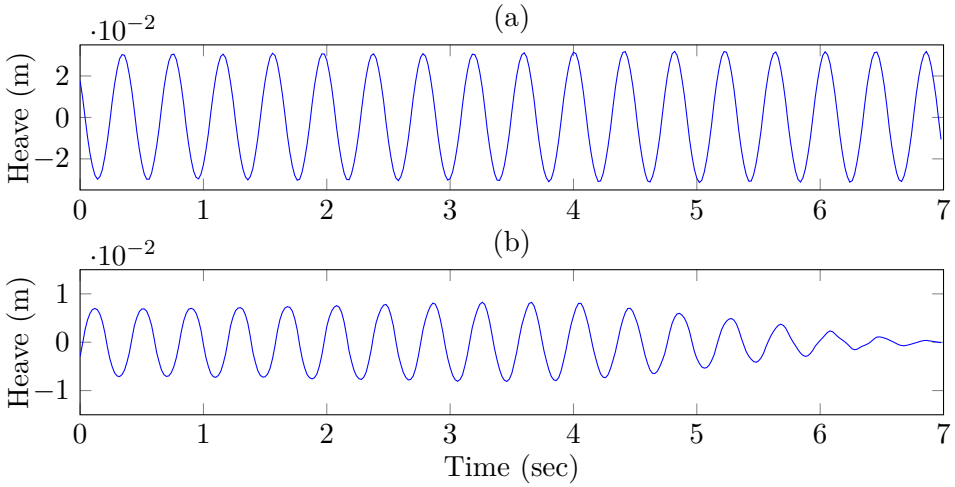

Figure 3.18: Response of the LCO after the controller was turned off at $t = 3$ *sec* (a) stable LCO (Wind speed = 16.4 m/sec), (b) unstable LCO (Wind speed = 16.4 m/sec).

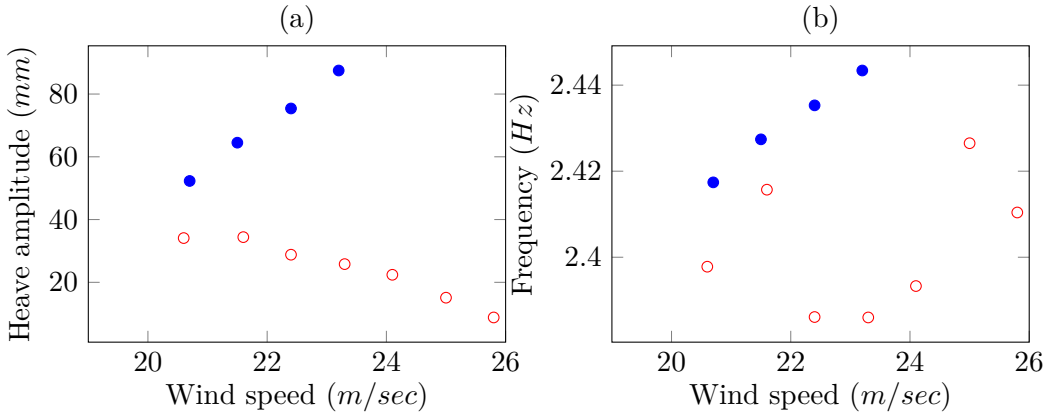

Figure 3.19: CBC results of a different leaf spring setup (a) Heave amplitude of LCO (mm), (b) Frequency of LCO (Hz). (●) is measured stable LCO and (○) is the measured unstable LCO.

Chapter 4

Parameter estimation of the mechanistic model with Hopf bifurcation

In this chapter, we

- develop parameter identification methods for mechanistic models undergoing Hopf bifurcation,
- use linear system identification methods to identify a linearisation of the model using a free-decay response,
- use centre manifold reduction and normal form analysis to parameterise the amplitude of the LCOs,
- identify nonlinear parameters by minimising the prediction error of the amplitude of LCOs near a Hopf bifurcation point,
- update the nonlinear parameters using spectral collocation methods to take into account higher-amplitude branches neglected in normal form analysis,
- apply the developed method to an experiment discussed in Section 3.3.3.3.

4.1 Introduction

Mechanistic models are derived using physical principles. For example, the mass-spring-damper model of mechanical systems can be derived using Newton's second law, which gives a second-order differential equation. The coefficients of the mass-spring-damper model, stiffness and

damping, are physically interpretable. Therefore, estimating the parameters of a mechanistic model using measured data can provide valuable physical insights to researchers.

In this chapter, we develop a parameter identification method for ODE models with Hopf bifurcation that can be applied to mechanistic models. Specifically, we identify the parameters of the aeroelastic flutter model that undergoes a subcritical Hopf bifurcation based on the experimental results of CBC presented in Chapter 3.

The modelling and analysis of LCOs in aeroelastic systems have been and remain an active research area [29]. Obtaining an accurate model of LCOs is challenging as it requires the 'right' balance between energy generation and dissipation in the model (to obtain a periodic response). Furthermore, the presence of LCOs usually cannot be explained by linear models and hence requires introducing and estimating nonlinear parameters. In [42], the nonlinear stiffness parameters of a plunge and pitch aerofoil were estimated using static tests. The identified model was then exploited to suppress LCOs using feedback linearisation. In [2], the method of multiple time scales was used to investigate the LCOs of a 2-DOF aerofoil and determine the supercritical nature of the Hopf bifurcation. The pitch and plunge amplitudes of the experimentally measured LCOs were compared to the model predictions to determine the quadratic and cubic stiffness coefficients in pitch.

The goal of parameter estimation in this chapter is to achieve a qualitative agreement in the bifurcation diagram between the model and the experiment. Compared to previous studies in parameter estimation of aerofoil models, the novelty of this chapter is that we consider both stable and unstable LCO branches that collide at the saddle-node bifurcation. On the other hand, other studies [2, 42] only considered LCO branches emanating from the Hopf bifurcation point. Furthermore, we implemented parameter estimation for a system with subcritical Hopf bifurcation that has rarely been studied in previous model identification studies.

We use a conceptually simple model of our experiment and normal form theory to predict the unstable LCOs of our physical system. We then propose a three-stage methodology to identify the parameters of this model based on experimental data. The first stage considers the use of conventional linear system identification techniques to identify the linear parameters of the model. The second stage estimates the nonlinear parameters of our model by minimising the error between the unstable LCOs predicted using normal form theory and the measured amplitude of LCO. The use of an analytical method is computationally effective. Finally, we update nonlinear parameters using the collocation method to consider stable LCOs that were not considered in the second stage.

We introduce the method to parameterise the amplitude of LCOs using centre manifold reduction and normal form theory in Section 4.2. In Section 4.3, the parameter estimation procedure of the ODE model is discussed.

4.2 Mathematical model

In this chapter, we use the mathematical model presented in Appendix A. We transform Eq. (A.1) into a system of first-order equations by setting $\mathbf{z} = [h, \dot{h}, \alpha, \dot{\alpha}, w, \dot{w}]^{\mathrm{T}}$. Eq. (A.1) is transformed into a more convenient form for the bifurcation analysis by introducing a new parameter $\mu = U - U_f$ where U_f is the flutter speed.

Our final model is

$$\dot{\mathbf{z}} = \mathbf{G}(\mathbf{z}, \mu). \tag{4.1}$$

The type of Hopf bifurcation depends on the first Lyapunov coefficient [49], which depends on the nonlinear part of $\mathbf{G}$. Lyapunov coefficient can be computed from the normal form, which will be explained in the next subsection.

4.2.1 Calculation of the unstable LCOs

In this chapter, the dynamics of the uncontrolled system are analysed near the Hopf bifurcation using centre manifold reduction. The objective of this analysis is to analytically predict the amplitude of unstable LCOs. Analytical predictions will be used to identify the nonlinear parameters of the system.

At the Hopf bifurcation point $(\mathbf{z}, \mu) = (0, 0)$, Eq. (4.1) can be rewritten as

$$\begin{aligned} \dot{\mathbf{x}} &= \mathbf{J}_{\mathrm{c}}\mathbf{x} + \mathbf{f}(\mathbf{x}, \mathbf{y}, \mu), \\ \dot{\mathbf{y}} &= \mathbf{J}_{\mathrm{s}}\mathbf{y} + \mathbf{g}(\mathbf{x}, \mathbf{y}, \mu), \end{aligned} \tag{4.2}$$

where $\mathbf{x} = [x, \bar{x}]^T \in \mathbb{C}^2$ and $\mathbf{y} \in \mathbb{C}^{n-2}$. The matrices $\mathbf{J}_{\mathrm{c}}$ and $\mathbf{J}_{\mathrm{s}}$ are partition of the Jordan canonical form of the Jacobian matrix of $\mathbf{G}(\mathbf{z})$ into its centre and stable subspaces, respectively. For simplicity, the eigenvalues of $\mathbf{J}_{\mathrm{c}}$ are assumed to be equal to $\pm\mathrm{i}$. $\mathbf{f}$ and $\mathbf{g}$ are functions with $\mathbf{f}(0,0) = 0$, $D\mathbf{f}(0,0) = 0$ and $\mathbf{g}(0,0) = 0$, $D\mathbf{g}(0,0) = 0$.

For system (4.2), there exists a local smooth centre manifold that is invariant under the action of the dynamical system [20]. A polynomial approximation of the centre manifold $\mathbf{H}(\mathbf{x}, \mu)$ can be computed recursively by solving

$$D\mathbf{H}(\hat{\mathbf{x}})(\hat{\mathbf{J}}_{\mathrm{c}}\hat{\mathbf{x}} + \mathbf{f}(\hat{\mathbf{x}}, \mathbf{H}(\hat{\mathbf{x}}))) = \mathbf{J}_{\mathrm{s}}\mathbf{H}(\hat{\mathbf{x}}) - \mathbf{g}(\hat{\mathbf{x}}, \mathbf{H}(\hat{\mathbf{x}})), \tag{4.3}$$

at each order of the polynomial expansion. To reduce the order of dynamics in the Hopf bifurcation, we include $\dot{\mu} = 0$ to Eq. (4.2) [49]. As such, $\hat{\mathbf{x}} = [\mu, \mathbf{x}]^T$ and $\hat{\mathbf{J}}_c$ is $\mathbf{J}_c$ extended with a zero on its diagonal [13]. The dynamics of the centre manifold can also be approximated using power series. The expansion considered is

$$\dot{x} = \mathrm{i}x + \sum_k f_k(x, \bar{x}, \mu) \quad \text{where} \quad f_k = \sum_{j+l+m=k} (\mathbf{a}_{1jlm} + \mathrm{i}\mathbf{a}_{2jlm}) x^j \bar{x}^l \mu^m, \tag{4.4}$$

$\mu = [\mu_1, \mu_2, \ldots, \mu_m]^T$, $\mu^m = \mu_1^{m_1}\mu_2^{m_2}\cdots\mu_m^{m_m}$, $\mathbf{a}_{1jlm} = [a_{1jlm_1}, a_{1jlm_2}, \ldots, a_{1jlm_m}]^T$ and $\sum_i m_i = m$.

The method of normal forms can be used to simplify Eq. (4.4). In this chapter, we exploit the so-called simplest normal form [112] (SNF) method that combines a near-identity coordinate transformation with suitable rescaling of the bifurcation parameter and time. The k-th order SNF takes the general form

$$\frac{du}{d\tau} = (\alpha_1\nu + \mathrm{i}\beta_1)u + (\alpha_2 + \mathrm{i}\beta_2)u^2\bar{u} + \mathrm{i}\sum_k g_k(u,\bar{u}), \tag{4.5}$$
$$\text{where } g_k(u,\bar{u}) = (b_{1k} + \mathrm{i}b_{2k})u^{\frac{k+1}{2}}\bar{u}^{\frac{k-1}{2}}, \text{ for odd integer } k \geq 5.$$

where $\alpha_1, \beta_1, \alpha_2, \beta_2 \in \mathbb{R}$. α_2 is the first Lyapunov coefficient, and its sign determines the criticality of the Hopf bifurcation. SNF makes the normal form of a Hopf bifurcation to Eq. (4.5) by removing all unnecessary terms in the equation using the near-identity transformation, the time and parameter re-scalings even if higher-order terms are taken into account in original system. The near-identity transformation, the time and parameter re-scalings are given by $x = h(u,\bar{u},\nu) = u + \sum_k h_k(u,\bar{u},\nu)$, $t = T(u,\bar{u},\nu,\tau)$ and $\mu = p(\nu)$, respectively. The reader is referred to [112] for a detailed derivation of the coefficients α_1, α_2, β_1 and β_2 and functions h, T, g and p. Note that the equation associated with the complex conjugate variable $\bar{u}$ is not shown in Eq. (4.5) for the sake of clarity.

Using $u = Re^{\mathrm{i}\theta}$, Eq. (4.5) can be written in polar coordinates. For the amplitude equation, this leads to the general expression

$$\frac{dR}{d\tau} = \alpha_1\nu R + \alpha_2 R^3. \tag{4.6}$$

The non-trivial fixed point of Eq. (4.6) corresponds to the amplitude of the LCO. The use of the SNF method leads to the presence of a single cubic term in Eq. (4.6), regardless of the order of the transformation [3, 111]. This greatly simplifies the parameterisation of the LCO amplitude used in the nonlinear parameter estimation method (Section 4.3).

4.3 Parameter estimation

The identification is performed in a staged process, starting with the identification of linear parameters using standard linear system identification techniques. Unstable LCOs measured using PP-CBC are then used to estimate the nonlinear stiffness parameters of the model. In the final stage, nonlinear parameters are updated using spectral collocation methods considering stable LCOs.

4.3.1 Parameters of underlying linear model

For small-amplitude responses, the contribution of the nonlinear part of the function Eq. (4.1) can be neglected and the system can be considered linear. The parameters of this underlying

linear model can be identified using conventional system identification techniques [55, 70, 90]. In this chapter, the equations of motion are expressed in state-space form, and model parameters are optimised using a conventional prediction error method (PEM), briefly explained hereunder. Note that other methods that used, for example, modal properties could have been used [33]. The experimental data exploited for the identification of the linear model parameters were obtained from free decay responses where no external force is applied with low-amplitude initial conditions and without airflow.

Without external excitation, the discrete-time equations of motion of the underlying linear model can be written as

$$\begin{aligned} \mathbf{z}(k+1) =& \mathbf{A}_d(\theta)\mathbf{z}(k), \\ \mathbf{y} =& \mathbf{C}\mathbf{z} + \mathbf{w}, \end{aligned} \tag{4.7}$$

where $\mathbf{y}$ is the vector of measured output that corresponds to the first and third state variables of the system (i.e. $\mathbf{C} = diag(1, 0, 1, 0)$). $\mathbf{w}$ is the measurement noise and $\mathbf{A}_d$ is the discrete-time state transition matrix defined as

$$\mathbf{A}_d(\theta) = e^{\mathbf{A}(\theta)T_s}, \tag{4.8}$$

where T_s is the sampling time and $\mathbf{A}(.)$ is the continuous-time state matrix from linearisation of Eq. (4.1). The vector of unknown parameters θ contains $\theta = [I_\alpha, c_\alpha, c_h, \dot{h}(0), \dot{\alpha}(0)]^T$. Note that the initial velocities of the system, $\dot{h}(0)$ and $\dot{\alpha}(0)$, are required to simulate the response of the model. As they were not measured, both velocities need to be estimated along with the other physical parameters of the system. The other parameters of the model, i.e., the air density ρ, the semi-chord of the wing b, the position of the elastic axis relative to the semi-chord a, the mass of the wing m, the mass of the total wing structure including support m_T and the non-dimensional distance between the centre of gravity and the elastic axis x_α, were all directly measurable. The natural frequencies of the modes associated with a motion in pitch $\omega_\alpha = \sqrt{k_\alpha/I_\alpha}$, and in heave $\omega_h = \sqrt{k_h/m_T}$ were also estimated from the frequency response of a shaker test.

The prediction error $\hat{\varepsilon}$ of the model can be defined as

$$\hat{\varepsilon}(k, \theta) = \mathbf{y}(k) - \hat{\mathbf{y}}(k|\theta), \tag{4.9}$$

where $\hat{\mathbf{y}}(k|\theta)$ is the model response calculated from Eq. (4.7). The optimisation is used to find the set of parameters $\hat{\theta}$ that minimises the prediction error (see [55] for additional details on the definition of the optimisation cost function). An optimisation was carried out using Matlab's system identification toolbox [56], and the code and results can be accessed in the Github repository. The initial value of θ is important to avoid reaching local minima during optimisation. The initial guess provided here is estimated from modal tests. The model identification was applied to two different flutter rig setups with different leaf spring setups where we distinguish

Table 4.1: Measured and identified parameter values of the linearized model.

Measured Parameter	Value	Identified Parameter	Value
$b\ (m)$	0.15	$I_\alpha\ (kgm^2)$	0.1724
a	-0.5	$c_\alpha\ (kgm^2/s^2)$	0.5628 (System 1), 0.9426 (System 2)
$\rho\ (kg/m^3)$	1.204	$c_h\ (kg/s)$	14.5756
$m_w\ (kg)$	5.3	$k_\alpha\ (N)$	54.11 (System 1), 61.30 (System 2)
$m_T\ (kg)$	16.9	$k_h\ (N/m)$	3529.4 (System 1), 3318.3 (System 2)
x_α	0.24		

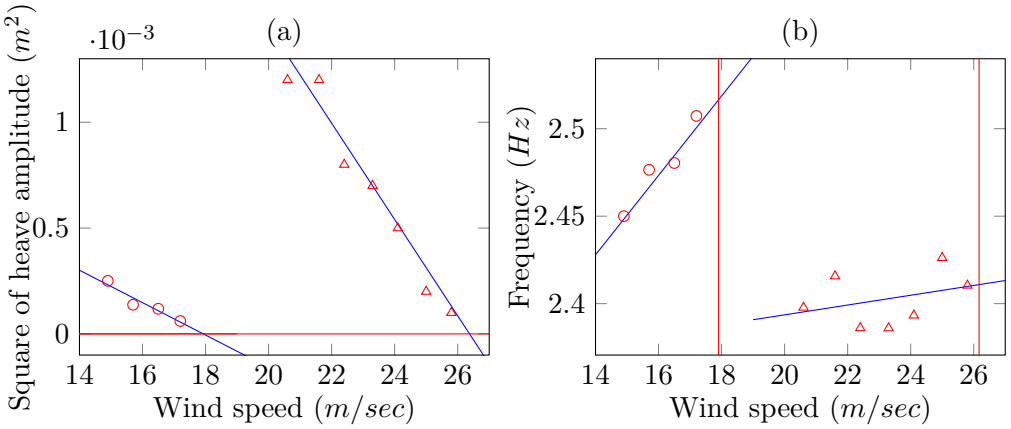

Figure 4.1: Estimation of flutter properties based on normal form (a) flutter speed estimation, (b) flutter frequeny estimation. (—) is the linear regression curve of the measured square of the amplitude of the heave, and (○) is the measured response of system 1, and (△) is the measured response of system 2. (—) indicates x-axis in (a) and the estimated flutter speed of two systems in (b).

these systems as system 1 and system 2.. The free optimisation parameters are I_α, c_α, and c_h for system 1 and c_α, k_α, and k_h for system 2. The values of the parameters measured and identified are given in Table 4.1.

The linear model can be validated by comparing the flutter speed, and frequency predicted by the model to the one predicted using the data collected with PP-CBC and normal forms. The real and imaginary parts of the eigenvalues of the linear model of system 1 are shown in Fig. 4.2 as a function of the wind velocity. Only two modes are shown in Fig. 4.2 because the other eigenvalues have a zero imaginary part and correspond to nonharmonic motions. According to Fig. 4.2, flutter occurs when the real part of the second mode becomes positive at a wind speed of 17.96 m/s. At that wind speed, the oscillation frequency is 2.46 Hz.

Identified linear models are validated using the PP-CBC results. Eq. (4.6) shows that the parameter μ (i.e. the wind velocity) is proportional to the square of the LCO amplitude where we assume $\nu \approx \mu$. Using linear regression, the wind speed at which flutter occurs is therefore directly estimated as the velocity for which the square of the LCO amplitude crosses zero

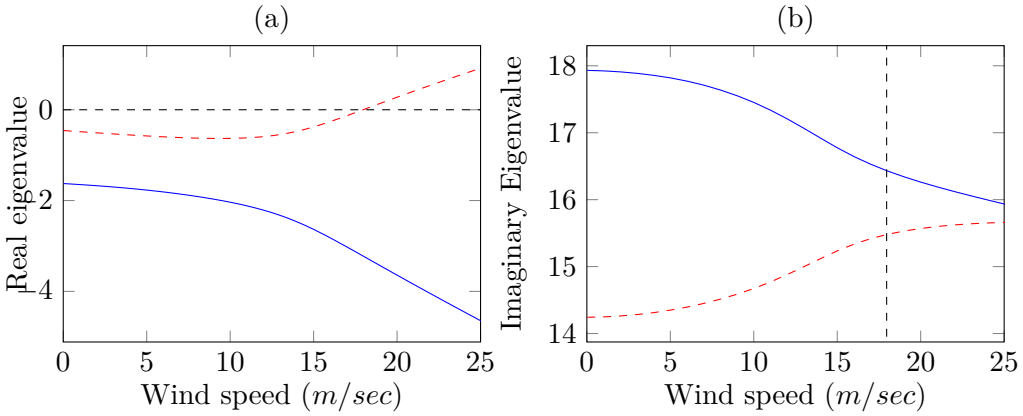

Figure 4.2: Eigenvalues of identified linearised system (a) real eigenvalue, (b) imaginary eigenvalue. (- - -) is mode 1 and (——) is mode 2. (- - -) in (a) is x-axis and (- - -) in (b) is the flutter speed.

(Fig. 4.1 (a)). The flutter speed estimated this way is 17.92 m/s, which is remarkably close to the flutter speed estimated from the linear model. There exists a linear relationship between the oscillation frequency and the wind speed near the Hopf point (if the normal form is truncated to the third order) [112]. The oscillation frequency at the flutter speed is estimated at 2.52 Hz, which again is very close to the value found in the linear model (Fig. 4.1 (b)).

For system 2, the estimated flutter speed from the model is 23.7 m/s, whereas the estimated flutter speed from the CBC experiment is 26.17 m/sec. The estimated flutter frequency of the model is 2.43 Hz, while the estimated flutter frequency of the CBC result is 2.41 Hz. The linear model validation result is in good agreement with the CBC experiment. However, we can see a larger discrepancy in flutter speed estimation for system 2 compared to system 1. We expect this is because linear coefficients estimated at the zero wind speed do not accurately capture the linearisation of the vector field at the higher wind speed, where system 2 has a much higher flutter speed than system 1.

4.3.2 Parameters of the nonlinear model

In this section, the parameters of the nonlinear model are estimated. We estimate the unknown nonlinear parameters using the measured amplitude of unstable LCOs. Amplitude of the unstable LCOs near the Hopf bifurcation are paramterised by unknown nonlinear coefficients using the simplest normal form discussed in Section 4.2.1.

Following the identification of the linear model and the flutter speed, the centre manifold reduction and associated reduced dynamics of system 1 can be calculated (see Section 4.2.1), and Eq. (4.6) becomes

$$\frac{dR}{d\tau} = 8.8 \times 10^{-3}\mu R + (-4.5 \times 10^{-5}k_{\alpha 3} + 8.4 \times 10^{-7}k_{\alpha 2}^2)R^3. \tag{4.10}$$

For system 2

$$\frac{dR}{d\tau} = 7.2 \times 10^{-3}\mu R + (-3.2 \times 10^{-5}k_{\alpha 3} + 4.9 \times 10^{-7}k_{\alpha 2}^2)R^3. \tag{4.11}$$

The amplitude of unstable LCOs, given by the nonzero fixed point of Eq. (4.10), is a function of the nonlinear stiffness parameters $k_{\alpha 2}$ and $k_{\alpha 3}$, and the bifurcation parameter $\mu = U_f - U$ where U is the wind speed and U_f is the flutter speed. μ is calculated using the flutter speed of the model for Eqs. (4.10) and (4.11) and using the estimated flutter speed for the training data sets generated from the CBC results. $k_{\alpha 2}$ and $k_{\alpha 3}$ are identified by minimising the prediction error of the LCO amplitude with a constraint to make a system subcritical. During parameter estimation, the near-identity transformation is approximated as the identity transformation since the points used in parameter estimation are close to the Hopf point and have a small amplitude. The optimised values obtained are $k_{\alpha 2} = 750.6\,Nm,\ k_{\alpha 3} = 5007.38\,Nm$ for system 1, and $k_{\alpha 2} = 771.9\,Nm,\ k_{\alpha 3} = 3222.52\,Nm$ for system 2.

The calculated heave amplitude by numerical continuation and the measured heave amplitude are compared for validation, which is presented in Figs. 4.3 and 4.4. Numerical continuation results are carried out using spectral collocation methods using the same parameters as in the normal form computation. The measured and computed heave amplitudes from the numerical continuation agree well at the unstable LCOs near the Hopf bifurcation point. However, both models as shown in Figs. 4.3 and 4.4 do not accurately predict high amplitude stable LCOs as the parameter estimation approach considers only the amplitude of unstable LCOs. However, the proposed system identification method– linearised model parameter identification from linear state-space model and nonlinear parameter identification using normal form theory– can successfully build a mathematical model that captures bifurcation behaviour in combination with the proposed CBC scheme.

4.3.3 Nonlinear parameter updating using collocation methods

The identified nonlinear parameters in Section 4.3.2 do not take into account the stable limit cycle oscillations in the high-amplitude branch. In this section, we will introduce a scheme to update the nonlinear parameters of the model using collocation methods adding stable LCO measured results in the training data sets. A nonlinear parameter update is applied to system 1.

Periodic solutions $\mathbf{x}_p(t)$ of $\dot{\mathbf{x}} = \mathbf{G}(\mathbf{x}, \mu)$ can be found using the periodic boundary value problem with the boundary condition $\mathbf{x}(0) = \mathbf{x}(T)$. We can solve this periodic boundary value problem using spectral collocation methods [102]. It is convenient to rescale the problem in a fixed time domain, such as $[0, 1]$ for orthogonal polynomial methods or $[-\pi, \pi]$ for spectral collocation methods. Here, we use spectral collocation methods, giving

$$\dot{\mathbf{x}} = \frac{T}{2\pi}\mathbf{G}(\mathbf{x}, \mu), \quad \mathbf{x}(-\pi) = \mathbf{x}(\pi), \tag{4.12}$$

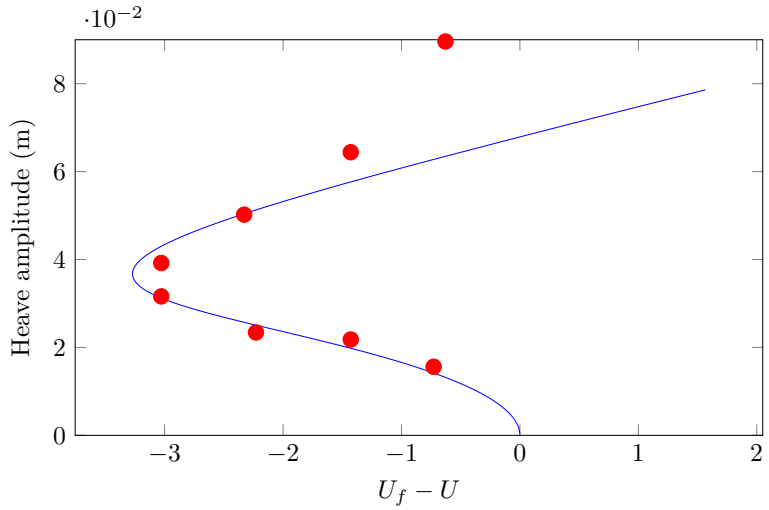

Figure 4.3: Comparison between the bifurcation diagram obtained from numerical continuation of the identified model of system 1 (—) and the CBC result of the system 1 (●).

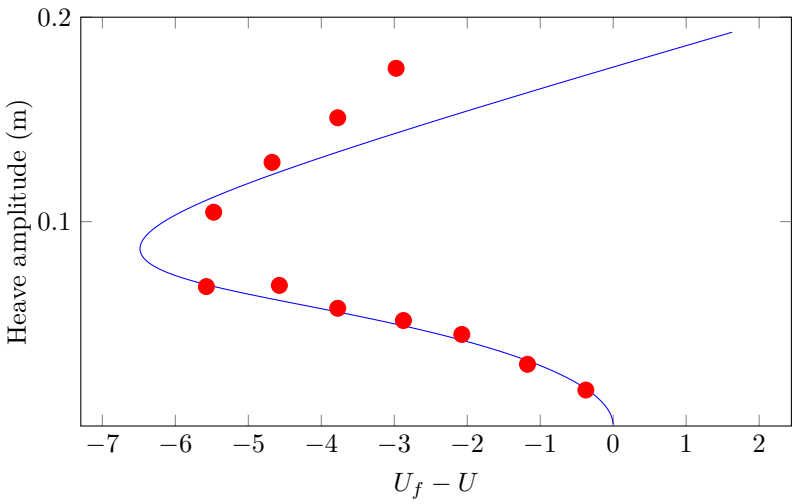

Figure 4.4: Comparison between the bifurcation diagram obtained from numerical continuation of the identified model of system 2 (—) and the CBC result of the system 2 (●).

where T is the period of $\mathbf{x}_p(t)$. Here, we interpolate $\mathbf{x}_p(t)$ as a sum of periodic sinc functions in a periodic grid of M points in the time interval $[-\pi, \pi]$ as

$$\mathbf{x}_p(t) = \sum_{k=1}^{N} = v_k S_M(t - t_k), \tag{4.13}$$

where S_M is a periodic sinc function on the M-point grid [102], t_k is equispaced with M points with $t_1 = -\pi$, $t_M = \pi - 2\pi/N$, and $v_k \in \mathbb{R}^N$ is the evaluation of $\mathbf{x}_p(t)$ at the point of the grid t_k. We can approximate $\dot{\mathbf{x}}$ at the points on the grid using the linear equation $\mathbf{D}_M\mathbf{v}$ where

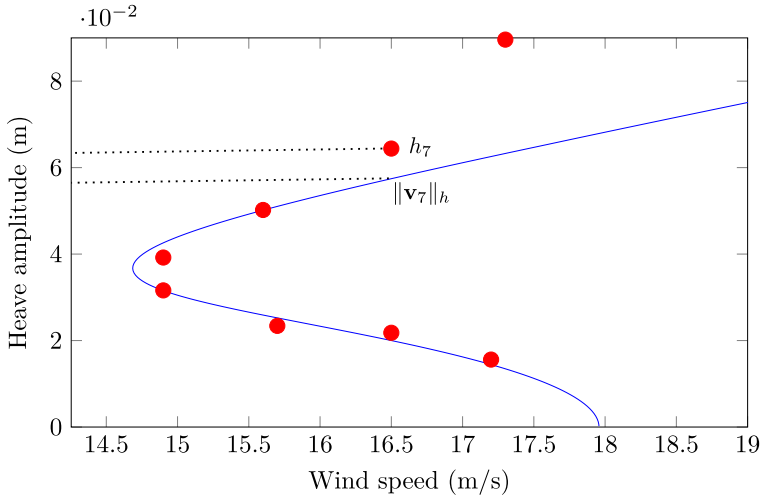

Figure 4.5: Visual description of $\|\mathbf{v}_7\|_h$ and h_7. Numerical continuation of the model(—) and the LCOs measured from CBC experiment (●). $\|\cdot\|_h$ denotes the amplitude of the periodic solution in the heave direction calculated from the periodic grid of $\mathbf{v}_i$.

$\mathbf{D}_M$ is a spectral differentiation matrix (see [102]), $\mathbf{v} = [v_1^T, \ldots, v_M^T]^T$. Therefore, Eq. (4.12) is transformed into a nonlinear fixed-point problem

$$\mathbf{D}_M \mathbf{v} - \begin{bmatrix} \frac{T}{2\pi}\mathbf{G}(v_1, \mu) \\ \vdots \\ \frac{T}{2\pi}\mathbf{G}(v_M, \mu) \end{bmatrix} = 0, \tag{4.14}$$

adding a phase condition equation and a pseudo-arclength equation, we can then track the family of $x_p(t)$ using the numerical continuation [47].

We identified the parameters $k_{\alpha 2}$ and $k_{\alpha 3}$ from the amplitude of unstable LCOs computed via centre manifold reduction and the normal form. Using numerical continuation, we can compute the family of periodic solutions shown in Fig. 4.5.

Let $(\mu_1, h_1), \ldots, (\mu_8, h_8)$ denote the measured periodic responses from the CBC experiment where μ_i is wind speed of i-th measured LCO and h_i is heave amplitude of i-th measured LCO. And let $(\mu_i, \mathbf{v}_i)$ denote the calculated periodic solutions that correspond to the measured response (μ_i, h_i) where $\mathbf{v}_i$ is the solution of Eq. (4.14) at $\mu = \mu_i$ (see Fig. 4.5 for the example of h_7 and $\mathbf{v}_7$). Note that the indices of the periodic solutions are ordered by the length of arclength from the Hopf bifurcation point. For example, the closest solution to the Hopf bifurcation point is $\mathbf{v}_1$.

The perturbation of the parameters is applied as $\theta = [\theta_1, \theta_2]^T$ where $k_{\alpha 2}$ is perturbed by $k_{\alpha 2} + \theta_1$, and $k_{\alpha 3}$ is perturbed by $k_{\alpha 3} + \theta_2$. For a relatively small perturbation with $\|\theta\| \ll 1$, set of periodic solutions $(\mu_1, \mathbf{v}_1), \ldots, (\mu_8, \mathbf{v}_8)$ is smoothly perturbed by θ as $(\mu_1, \mathbf{v}_1^\theta), \ldots, (\mu_8, \mathbf{v}_8^\theta)$ where $(\mu_i, \mathbf{v}_i^\theta) = (\mu_i, \mathbf{v}_i)$ at $\theta = 0$ for $i = 1, \ldots, 8$.

We update the parameters $k_{\alpha 2}$ and $k_{\alpha 3}$ to minimise the prediction of the bifurcation diagram plotted by heave amplitude by setting a cost function as

$$\mathbf{c}(\theta) = \sum_{j=1}^{8} (\|\mathbf{v}_j^\theta\|_h - h_j)^2, \tag{4.15}$$

where $\|\cdot\|_h$ is a function that measures the amplitude of periodic solution in the heave direction from points on the periodic grid. The direction of the new perturbation θ_p is calculated at the perturbation value in the last step θ_0 using gradient decent as

$$\theta_p = -\frac{d\mathbf{c}}{d\theta}(\theta_0)\zeta \tag{4.16}$$

where $\zeta \in \mathbb{R}$ is the damping rate and $\frac{d\mathbf{c}(\theta)}{d\theta}$ is calculated using finite difference. At every iteration step, $\mathbf{v}_j^\theta$ is computed by solving Eq. (4.14) using the last perturbed solution as the initial guess of the Newton iteration. $\mathbf{v}_j^\theta$ is updated until $\|\frac{d\mathbf{c}}{d\theta}(\theta)\| < 10^{-6}$. The model update procedure for nonlinear stiffness parameters $k_{\alpha 2}$ and $k_{\alpha 3}$ is summarised as

1. Perturb $[k_{\alpha 2}, k_{\alpha 3}]$ with $\theta = [\varepsilon, 0]$ and compute $\mathbf{v}^\theta$ and $\frac{\partial \mathbf{c}}{\partial k_{\alpha 2}}$ using a finite difference.
2. Compute $\frac{\partial \mathbf{c}}{\partial k_{\alpha 3}}$ similarly and compute the next perturbation as $\theta_p = -\frac{d\mathbf{c}}{d\theta}(\theta_0)\zeta$
3. Update nonlinear stiffness with θ_p and compute $\mathbf{v}^{\theta_p}$ by solving Eq. (4.14).
4. Check $\|\frac{d\mathbf{c}}{d\theta}(\theta_p)\| < 10^{-6}$ and repeat the procedure if it is not.

The final optimised value of the nonlinear stiffness is $k_{\alpha 2} = 751.2\,Nm$ and $k_{\alpha 3} = 4769.1\,Nm$. However, the resulting bifurcation diagram does not dramatically improve the fitting of the unperturbed system as shown in Fig. 4.6. The updated model slightly reduces the prediction error at the stable LCOs; however, it does not capture the saddle-node bifurcation and the overall bifurcation diagram sufficiently accurately. Fig. 4.6 suggests that the estimated nonlinear stiffness parameters from normal-form computation are approximately a local minimum of data-fitting criteria defined by fitting the bifurcation diagram. This results from a lack of flexibility of the model to capture the bifurcation structure using free parameters $k_{\alpha 2}$ and $k_{\alpha 3}$.

4.4 Conclusion

In this chapter, we developed a method for estimating the system parameters based on a measured bifurcation diagram. First, the parameters of the linearised system are identified using the state-space approach from a free-decay response. Then, the nonlinear parameters are identified using centre manifold reduction and normal form from a measured bifurcation diagram. Finally, nonlinear parameters are updated using collocation methods while considering

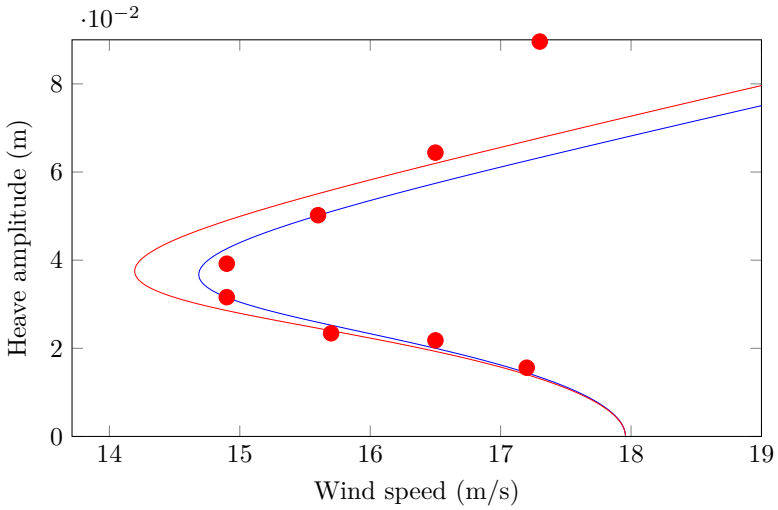

Figure 4.6: Bifurcation diagram of a mathematical model with updated nonlinear stiffness. Unperturbed model (—) and updated model (—).

higher-amplitude LCOs that were not included in the initial nonlinear parameter estimation. The method is applied to the CBC experiment of the flutter rig in Section 3.3.3.3.

The identified model captures the bifurcation structure well, and the model parameters add physical insights to the researcher. However, this chapter shows that mechanistic models with few free parameters are not flexible enough to capture high-amplitude branches generated at the fold. This motivates us to seek models with more flexibility, such as neural networks and kernel functions, which will be discussed in Chapters 5 and 6.

Data and code availability

Julia package developed for study in this chapter is available in repository HopfNormalForm.jl.

CHAPTER 5

Bifurcation-based data-driven modelling of ODEs with centre manifolds

In this chapter, we

- develop bifurcation-based data-driven modelling of parameter-dependent ODEs with centre manifolds,
- use domain knowledge of the modelling: existence and the dimension of the invariant manifold and the bifurcation structure,
- set the basis of the model by combining a normal form like an equation and the observation function,
- demonstrate the developed modelling method on numerical synthetic data sets generated from the Van der Pol equation and the aeroelastic flutter model,
- demonstrate the developed modelling method on an experimental result discussed in Section 3.3.3.3.

5.1 Introduction

For self-excited systems with a Hopf bifurcation, the change in parameter leads to a loss of stability of the equilibrium and the birth of a family of LCOs near the bifurcation point. To analyse the periodic responses of such systems and determine the amplitude of the LCOs, it is customary to reduce the dynamics of the original system near the bifurcation point to a low-dimensional centre manifold. The hybrid modelling methodology proposed here takes advantage of this equivalence. A low-dimensional normal form-like model is used to capture the

phenomenology of the real system, i.e. its bifurcation structure. A data-driven mapping from this model to the full system is then identified using machine learning (ML) and experimentally measured data (here, LCOs).

The use of ML models is attractive because they are theoretically capable of representing any continuous function [110]. However, the use of traditional ML techniques and models presents a number of difficulties. For example, a considerable amount of data is often needed to train ML models [108]. Furthermore, even if such data are available and the obtained ML model accurately represents the training data set, ML models can still fail to generalise to unseen conditions [81] or even fail to capture the fundamental physics of the system [46]. The approach proposed in this chapter is inspired by the recent development of scientific machine learning (SciML), which aims at making ML models more interpretable, more consistent with the known laws of physics, and less data-hungry by combining them with mechanistic (i.e., physics-based) models. Examples of SciML approaches include Physics-Informed Neural Networks (PINNs) [79] where a neural network is used to solve and discover partial differential equations (PDEs) while respecting the laws of physics through constraints incorporated into the training cost function. In [78, 79] linear ordinary differential equations (ODEs) were successfully discovered from the data using probabilistic machine learning and Gaussian process regression. Universal differential equations (UDEs) [76] are differential equation models that combine mechanistic differential equations with universal approximators such as neural networks, Chebyshev expansions, or random forests directly introduced into model equations.

While existing studies have mostly focused on numerical simulations and a quantitative agreement between time series at particular parameter values, the approach proposed here aims to capture the bifurcation diagram of a physical system, which requires the accurate prediction of the system's parameter dependence, its long-term behaviour (here LCOs), and to deal with experimental (i.e. noise-corrupted) measurements. In this context, Beregi et al. [10] combined machine-learnable functions with mechanistic models to capture bifurcation diagrams. The approach proposed here differs in that it uses only knowledge of the bifurcation structure observed in the experiment. The normal form-like model and its associated bifurcation structure form the mechanistic model that captures the "*physics*" of the system and underpins the otherwise data-driven model. The hybrid mechanistic/machine-learnt (M/ML) model obtained does not rely on any problem-specific variables and is therefore applicable to any system exhibiting the bifurcation structure imposed by the underlying mechanistic model, even without any other physical model available.

The use of a model to capture the type of bifurcation observed in the data is very beneficial, as it reduces the amount of data required to train the model and improves the ability of the model to interpolate between data points and even extrapolate outside the range of control parameters used for model training. Moreover, by leveraging the fact that the dynamics of the system evolve on a low-dimensional sub-manifold and using a polar representation, the

training of time series requires the time integration of a single one-dimensional ODE, which is computationally much more efficient than other data-driven modelling procedures using numerical integration of the entire model as in [76]. The hybrid M/ML models developed in this chapter could be exploited in different ways. For instance, machine-learnt mapping could be analysed to improve understanding of the physical system and provide new insights into the derivation of more accurate mechanistic models. The proposed models also have the potential to be used as digital twins where the nature of the system is captured qualitatively using the mechanistic part of the model, and data are continuously used to refine and evolve the model during the system's life. Exploring these applications is beyond the scope of this thesis.

We first explain how we set the structure for the bifurcation-based ML in Section 5.2. In Section 5.3, a strategy of two-stage model training is explained. We show the robustness of bifurcation-based ML using synthetic data generated from the ground truth model in Section 5.4. Finally, the bifurcation-based ML is applied to a CBC experiment results of Chapter 3 in Section 5.5.

5.2 Model structure

Mechanistic model It is assumed that the physical system of interest can be represented by an unknown continuous-time dynamical system (N, Φ^t), where $N \subset \mathbb{R}^{n+1}$ with $n \geq 2$ is the number of states and $\Phi^t : \mathbb{R}^+ \times N \to N$ is the evolution of the flow governed by a set of ODEs. The system (N, Φ^t) is assumed to undergo a Hopf bifurcation at a certain parameter $\mu = \mu_0$ which is not necessarily known, and the sub/supercritical nature of the bifurcation is known (or at least identifiable from experimental data). For instance, PP-CBC discussed in Chapter 3 can be used to obtain such qualitative information. The parameter μ is constant over time and is taken as one of the dimensions of N.

There exists a 3-dimensional centre manifold M^c near the Hopf bifurcation point that can be parametrised as a graph $\mathbf{M}^c_{\mathbf{x}}$ [20]:

$$\mathbf{M}^c_{\mathbf{x}} = \{(\mathbf{x}, \mathbf{y}) | \mathbf{y} = \mathbf{h}(\mathbf{x})\}, \tag{5.1}$$

where $\mathbf{x}$ is the centre subspace, $\mathbf{y}$ is the attracting subspace defined at the equilibrium of $(N, \Phi^t_{\text{full}})$, and $\mathbf{h}$ is a nonlinear function. M^c is an attracting invariant manifold in the state space of the full dynamical system $(N, \Phi^t_{\text{full}})$. The dynamics of the system in the centre manifold is defined as $(M^c, \Phi^t_{\text{red}})$, where $\Phi^t_{\text{red}} : \mathbb{R}^+ \times M^c \to M^c$ is the evolution of the flow in the centre manifold M^c. The system $(M^c, \Phi^t_{\text{red}})$ is a reduced order model of $(N, \Phi^t_{\text{full}})$ with $\dim(M^c) \leq \dim(N)$. The reduced dynamics is usually expressed as $\dot{\mathbf{x}} = \mathbf{f}(\mathbf{x})$ where $\mathbf{f}$ is the system's vector field projected onto the centre manifold parametrised by $\mathbf{x}$. It is also possible to find a smooth, invertible change of coordinates such that the reduced dynamics can be

represented using the modified Hopf normal form

$$\begin{aligned}\dot{u}_1 &= (\mu-\mu_0)u_1 - u_2\Omega(u_1,u_2,\mu) + a_2u_1(u_1^2+u_2^2) - u_1(u_1^2+u_2^2)^2,\\ \dot{u}_2 &= (\mu-\mu_0)u_2 + u_1\Omega(u_1,u_2,\mu) + a_2u_2(u_1^2+u_2^2) - u_2(u_1^2+u_2^2)^2,\\ \dot{\mu} &= 0,\end{aligned} \tag{5.2}$$

which can also be written in polar coordinates as

$$\begin{aligned}\dot{r} &= (\mu-\mu_0)r + a_2r^3 - r^5\\ \dot{\theta} &= \Omega(r,\theta,\mu)\\ \dot{\mu} &= 0.\end{aligned} \tag{5.3}$$

where (u_1, u_2, μ), or (r, θ, μ), are the coordinates parameterising the invariant manifold. The sign of the coefficient a_2 depends on the criticality of the Hopf bifurcation. Fifth-order terms are added to introduce a saddle-node bifurcation of periodic orbits and capture the presence of stable LCOs frequently observed in systems with subcritical Hopf bifurcations. For the latter, stable and unstable LCOs coexist for $\mu \in [\mu_0 - a_2^2/4,\ \mu_0]$. Ω is an a priori unknown function that governs the speed of the oscillations and reproduces the time evolution of the data (see Section 5.3). From Eq. (5.3), it is clear that the oscillation amplitude r is independent of the oscillation speed. This observation will be exploited in Section 5.3 to simplify the training of the ML model by learning the coordinate mapping and the oscillation speed separately.

Eqs. (5.2) and (5.3) are not the only way to represent the dynamics of a system with a Hopf bifurcation followed by a saddle-node bifurcation. An alternative parameterisation of the invariant manifold can be used, using, for example, $\mathbf{x}$ as in Eq. (5.1), can be used. This would result in a set of ODEs that is different from Eqs. (5.2) and (5.3). However, those different reduced systems are topologically equivalent to each other, i.e. one can be transformed to another by a change of coordinates [49]. The choice to take the normal form-like equation as a mechanistic model was made to emphasise the nature of the phenomenon targeted by the model.

Mapping to observations Following the definition of the mechanistic model (5.2), a data-driven transformation from the model to the observation is defined. Let us consider the measured observations $\mathbf{z} = [z_1, \ldots, z_m, \mu]^{\mathrm{T}} \in \mathbb{R}^{m+1}$, where m is the total number of states observed, and the predicted observations $\hat{\mathbf{z}} = [\hat{z}_1, \ldots, \hat{z}_m, \hat{\mu}]^{\mathrm{T}} \in \mathbb{R}^{m+1}$. A function $\mathbf{g}(u_1, u_2, \mu) = \hat{\mathbf{z}}$ can be defined to map the dynamics of the reduced system (5.2) to the predicted experimental observations $\hat{\mathbf{z}}$ made on the centre manifold M^c. The map $\mathbf{g}$ can be defined as a vector of two functions $\mathbf{g} = \left[\mathbf{U}^T,\ g_\mu\right]^T$. The first function, $\mathbf{U}(u_1, u_2, \mu) = [\hat{z}_1, \ldots, \hat{z}_m]^{\mathrm{T}}$, represents the mapping between (u_1, u_2, μ) and the observed states. The LCOs in Eq. (5.2) trace circular trajectories in the plane (u_1, u_2). Therefore, the objective of mapping $\mathbf{U}$ is to transform these circles into the distorted closed curves observed experimentally (as illustrated in Fig. 5.1).

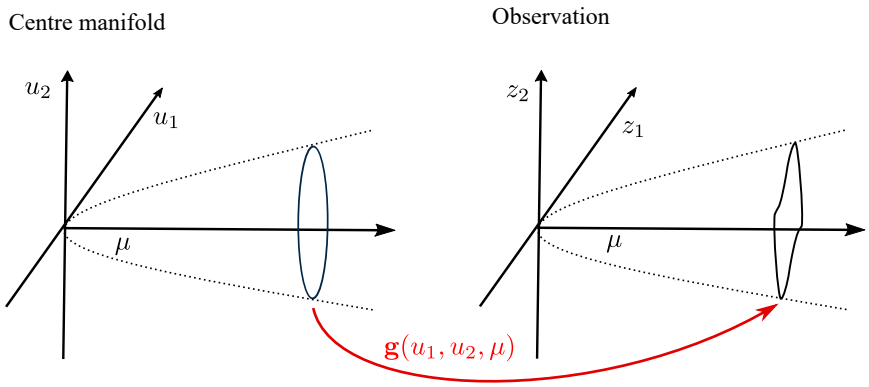

Figure 5.1: Geometric illustration of the coordinate transformation $\mathbf{U}_{12}(u_1, u_2, \mu)$ applied to a LCO of a supercritical Hopf bifurcation.

The second part of the map $\mathbf{g}$, $g_\mu(u_1, u_2, \mu) = \hat{\mu}$, represents the mapping between the model parameter μ and the predicted observed parameter. In the present and common case where the bifurcation parameter is measured directly during the experiment and not rescaled, the mapping reduces to a simple projection, i.e. $g_\mu(u_1, u_2, \mu) = \mu$.

5.3 Model training

5.3.1 Closed orbit representation

We assume there exists a pair of coordinates for which the measured LCOs form closed curves that can be parameterised in polar coordinates, i.e. the measured trajectory of LCOs does not self-intersect and has a unique angular parameterisation in a plane. This assumption is satisfied in the neighbourhood of the Hopf bifurcation point, and it is assumed that it extends to all the measured LCOs. For convenience, this pair of measured coordinates is labelled (z_1, z_2), while the remaining measured signals are $(z_3, ..., z_m)$. The map $\mathbf{U}$ is split accordingly as $\mathbf{U} = \left[\mathbf{U}_{12}^T,\ \mathbf{U}_{3...m}^T\right]^T$. The measured coordinate is translated to have an origin inside the measured closed curves to represent periodic solutions using polar representation.

The map $\mathbf{U}_{12}$ from the normal form coordinates (u_1, u_2, μ) to the predicted observations $(\hat{z}_1, \hat{z}_2)$ is first sought. The particular challenge associated with finding this first map $\mathbf{U}_{12}$ is that the correspondence between points (u_1, u_2) in the normal form coordinates and observations (z_1, z_2) is initially unknown. Therefore, it is not possible to obtain $\mathbf{U}_{12}$ by solving a regression problem since the input and output data points cannot be paired together. However, once this first map is found, the rest of the map $\mathbf{U}$ that addresses the presence of additional states $(\hat{z}_3, \ldots, \hat{z}_m)$ can be easily determined. This will be discussed later in this section.

Finding the first mapping To train $\mathbf{U}_{12}$, the idea is to compare the continuous representation of the predicted and measured LCOs. This approach has the advantage of avoiding any pointwise comparison between the data points and the predictions of the model. The training process starts by taking a user-defined number of points along periodic responses in the normal form coordinates. Those points are mapped to the observation space using the current estimate of the mapping $\mathbf{U}_{12}$. Following the coordinate transformation, the closed curves obtained from the transformed trajectories can be directly compared with the measured LCOs. Comparing closed planar curves is a well-established problem in pattern recognition [88, 114], and a popular way to approach this problem is to use a Fourier representation of the curve along the arc-length [113]. However, with such a representation, it is difficult to define a metric between two distinct curves if they do not share at least one point. For this reason, here we consider the simpler approach of directly using a phase-like angle to parameterise the orbit. This assumption is consistent with the normal form model and the closed curves observed experimentally, which have a much simpler geometry than the one usually investigated in pattern recognition [113]. The polar representation of the planar orbits in terms of amplitude and angle is obtained for the measured and predicted curves as follows.

$$R = \sqrt{z_1^2 + z_2^2}, \quad \theta = \tan^{-1}\frac{z_2}{z_1}, \qquad \text{and} \qquad \hat{R} = \sqrt{\hat{z}_1^2 + \hat{z}_2^2}, \quad \hat{\theta} = \tan^{-1}\frac{\hat{z}_2}{\hat{z}_1}. \tag{5.4}$$

As the polar representations of the LCOs are assumed to be smooth and periodic; they can be represented as a truncated Fourier series

$$R(\theta) = a_0 + \sum_{k=1}^{n_h} a_k \cos(k\theta) + \sum_{k=1}^{n_h} b_k \sin(k\theta), \qquad \text{and} \qquad \hat{R}(\hat{\theta}) = \hat{a}_0 + \sum_{k=1}^{n_h} \hat{a}_k \cos(k\hat{\theta}) + \sum_{k=1}^{n_h} \hat{b}_k \sin(k\hat{\theta}), \tag{5.5}$$

where the number of Fourier modes, n_h, is assumed to be large enough to have a small approximation error. The shape of the closed curves $R(\theta)$ and $\hat{R}(\hat{\theta})$ are thus represented by vectors of coefficients determined by the Fourier projection $\Phi(\cdot)$ as $\Phi(R) : C_p([0, 2\pi], \mathbb{R}) \to \mathbb{R}^{2n_h+1} = [a_0, \ldots, a_{n_h}, b_1, \ldots, b_{n_h}]^{\mathrm{T}}$ where

$$a_0 = \frac{1}{2\pi}\int_0^{2\pi} R\mathrm{d}\theta, \qquad a_n = \frac{1}{\pi}\int_0^{2\pi} R\cos(n\theta)\mathrm{d}\theta, \qquad b_n = \frac{1}{\pi}\int_0^{2\pi} R\sin(n\theta)\mathrm{d}\theta \qquad \text{for} n = 1, 2, \ldots, n_h. \tag{5.6}$$

Alternatively, the vector of the coefficient can be computed in the least squares sense directly using Eq. (5.5) and the pseudoinverse [67].

Taking a family of LCOs from the branch emerging at the Hopf bifurcation point, the error between model predictions and the data is given by

$$\Xi_{\mathbf{U}} = \sum_{i=1}^{m_s} \|\Phi(R_i) - \Phi(\hat{R}_i)\| \tag{5.7}$$

where m_s is the number of LCO measured. This measure of model error is the cost function that is minimised during the training of the coordinate transformation detailed in Section 5.3.2.

Mapping to other measured signals After obtaining $\mathbf{U}_{12}$, it is possible to use the inverse transformation $\mathbf{U}_{12}^{-1}$ to find the points in the normal form coordinates that are associated with the measured data. Taking these points as input, it is then straightforward to train the remaining $m-2$ maps to the output observations $(z_3, \ldots, z_m)$ using standard input-output regression techniques such as kernel ridge regression [45] or neural networks. $\mathbf{U}_{3\ldots m}$ models additional observations that are not used in the normal form model derivations. Also, note that we only provide concepts to model additional observations using $\mathbf{U}_{3\ldots m}$ where we do not provide further modelling examples.

5.3.2 Functional form of the map

Neural networks provide a flexible approach to model mapping $\mathbf{U}_{12}$ [52, 110]. However, it was found that the use of a neural network alone often leads to mappings that do not preserve the topology of the LCOs. Therefore, it is advantageous to use a simpler initial transformation that preserves this topology. This transformation has the additional benefits of reducing the complexity of the neural network and simplifying its training. The planar mapping $\mathbf{U}_{12}(u_1, u_2, \mu) = [\hat{z}_1, \hat{z}_2]^{\mathrm{T}}$ is thus defined as the sum of three separate contributions as

$$\mathbf{U}_{12}(u_1, u_2, \mu) = \underbrace{T_L(u_1, u_2, \mu) \quad + \quad T_s}_{\text{Transforms LCO to an ellipse}} + \underbrace{\mathrm{NN}_{\Theta_{\mathbf{U}}}(u_1, u_2, \mu)}_{\text{Correction}}, \tag{5.8}$$

where

$$T_L(u_1, u_2, \mu) = \begin{bmatrix} l_{11} & l_{12} & l_{13} \\ l_{21} & l_{22} & l_{23} \end{bmatrix} \begin{bmatrix} u_1 \\ u_2 \\ \mu \end{bmatrix} \qquad \text{and} \qquad T_s = \begin{bmatrix} s_1 \\ s_2 \end{bmatrix}. \tag{5.9}$$

The linear transformation performed by $T_L(u_1, u_2, \mu) = [\hat{z}_1, \hat{z}_2]^{\mathrm{T}}$ stretches and rotates the closed curves. This transformation includes six unknown parameters l_{ij} that will be estimated using experimental data. The transformation matrix must be nonsingular. The coordinate transformation $T_s(u_1, u_2, \mu) = [\hat{z}_1, \hat{z}_2]^{\mathrm{T}}$ applies a rigid translation of the trajectories and requires two additional parameters s_1, s_2. Finally, $\mathrm{NN}_{\Theta_{\mathbf{U}}}(u_1, u_2, \mu) = [\hat{z}_1, \hat{z}_2]^{\mathrm{T}}$ is a neural network with unknown weight vector $\Theta_{\mathbf{U}}$.

Including T_L and T_s explicitly in $\mathbf{U}_{12}$ can be interpreted as introducing additional physics or knowledge into the definition of the coordinate transformation. Indeed, shifting and rescaling coordinates must be performed to transform the orbits from the space of the normal-form model to the space of the physical system, and this operation is commonly performed in normal-form calculations in bifurcation analysis. With this approach, the neural network model $\mathrm{NN}_{\Theta_{\mathbf{U}}}$, can be viewed as a "small" correction to the initial transformation performed by $T_L + T_s$ (Fig. 5.2).

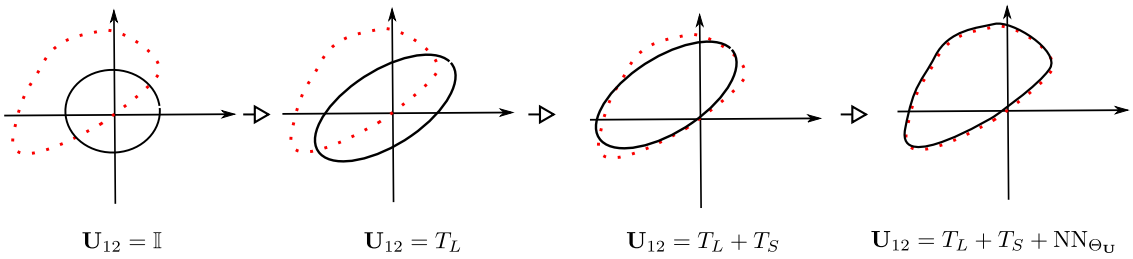

Figure 5.2: Combined effect of the different components included in the transformation from normal form coordinates $\mathbf{u}$ to physical space $\mathbf{z}$. (—) LCO obtained after transformation. (●) Experimental data.

5.3.3 Oscillation speed

The oscillation speed of an LCO trajectory is defined by the general expression

$$\Omega(r\cos\theta, r\sin\theta, \mu) = \omega_0 + \mathrm{NN}_{\Theta_\Omega}(r,\mu)^{\mathrm{T}}[1, \cos\theta, \ldots, \cos n_h\theta, \sin\theta, \ldots, \sin n_h\theta]^{\mathrm{T}}, \tag{5.10}$$

where the first term, ω_0, represents the fundamental oscillation frequency. The second term provides a periodic correction to this fundamental frequency in order to capture state and parameter dependencies. Although this general correction term is particularly useful for capturing systems where multiple timescales occur within the LCO, it can be significantly simplified for systems where only one frequency dominates the response (see Section 5.4).

Following the training of the coordinate transformation, Ω is trained by minimising the prediction error between the predicted and observed time series. To generate time series from the model, suitable initial conditions in the normal form coordinates that correspond to the initial measured data must be obtained. One approach to finding the initial conditions $\mathbf{u}^i(t_1)$ would be to solve

$$[\mathbf{u}^i(t_1), \mu_i] - \mathbf{g}^{-1}(\mathbf{z}^i(t_1), \mu_i) = 0 \tag{5.11}$$

where t_1 represents the first time instant in the time series. However, model inaccuracies and measurement noise perturb the initial point $\mathbf{u}^i(t_1)$, away from the trajectory of the LCO predicted at the parameter value μ_i. Although this is not a significant problem when training stable LCOs; it becomes an issue for unstable LCOs, as the numerical integration of the initial value problem will not approach the trajectory of LCOs. The approach followed to solve this problem is to find the initial conditions $\mathbf{u}^i(t_1)$ for which the prediction of the model $(\hat{z}_1^i, \hat{z}_2^i) = \mathbf{U}_{12}(\mathbf{u}^i(t_1), \mu_i)$ has the same phase angle θ as the initial conditions of the measured signal. The initial conditions in the normal form coordinates, $\mathbf{u}^i(t_1)$, are thus found by solving

$$\mathrm{ang} \circ \mathbf{U}_{12}(\mathbf{u}^i(t_1), \mu_i) - \mathrm{ang} \circ \mathbf{z}^i(t_1) = 0, \tag{5.12}$$

where $\mathrm{ang} : (x, y) \mapsto \tan^{-1}(y/x)$ measures the phase angle of the vector $[x, y]^T$. Eq. (5.12) can be solved using the Newton method.

Once the initial conditions have been determined, the polar form of the normal-form model is considered for numerical integration. In this case, only the second equation of Eq. (5.3) needs to be integrated, as the LCOs correspond to fixed points of the first equation. Only integrating the second equation also has the advantage of avoiding any numerical instability issues, even in unstable solutions. Indeed, this second equation corresponds to the direction of the velocity vector, i.e. the direction vector of the trivial Floquet multiplier that is equal to unity.

The parameters ω_0 and Θ_Ω that define the oscillation speed Ω are then determined by minimising the cost function

$$\Xi_\Omega = \sum_{i=1}^{m_s} \sum_j \|\mathbf{U}_{12}(\mathbf{u}^i(t_j), \mu_i) - \mathbf{z}_i(t_j)\|, \tag{5.13}$$

5.3.4 Learning stages

The model training is a three-stage process. The parameters of the linear transformations T_L and T_s are found first by minimising Ξ_U. During this process, an approximate value of the bifurcation parameter μ_0 is used. After training of the linear transformation, the LCOs in normal-form space can be mapped to ellipses that are "close" to the measured trajectories. During the second training step, the parameters of $\mathrm{NN}_{\Theta_\mathbf{U}}$ and the more precise values for μ_0 and a_2 are found by further minimising Ξ_U. The linear transformation parameters are kept constant during this process. The third training step is to find the parameters associated with the oscillation speed Ω, i.e. ω_0 and Θ_Ω, by minimising Ξ_Ω.

Traditional deep learning packages such as PyTorch[65] and Flux.jl[41] can be used to train $\mathbf{U}$ and the other model parameters using optimisation techniques such as the stochastic gradient decent method [25, 54]. For Ω, the package DiffEqFlux.jl [76] which uses stochastic gradient descent methods in the solutions of differential equations [50, 115] was used.

5.4 Numerical demonstration

In this section, the method developed in Sections 5.2 and 5.3 is numerically demonstrated on a Van der Pol oscillator and a 3-degree-of-freedom model of an aerofoil that undergoes aeroelastic oscillations. The synthetic data used for model training are noise-free and were obtained using time integration. Demonstration of real experimental data is carried out in Section 5.5.

5.4.1 Van der Pol oscillator

The equations governing the dynamics of the Van der Pol oscillator are

$$\begin{aligned} \frac{dz_1}{dt} &= z_2, \\ \frac{dz_2}{dt} &= 2\mu z_2 - z_1^2 z_2 - z_1, \end{aligned} \tag{5.14}$$

where the states (z_1, z_2) and the control parameter μ are all assumed to be measured directly. For this example, a supercritical Hopf bifurcation occurs at $\mu_0 = 0$ and only stable LCOs exist. As such, the parameter a_2 of the mechanistic model (5.2) is set equal to -1 and the fifth-order terms are removed. Training data are generated for six different parameter values $\mu = (0.1,\ 0.28,\ 0.46,\ 0.64,\ 0.82,\ 1.0)$. At each parameter value, the oscillator response is simulated over 10 seconds using initial conditions on the LCOs (i.e., there are no transients in the data) and a sampling time of 0.02 s. This represents 500 samples per time series, and hence 3000 samples for the whole training data set.

Following the procedure described in Section 5.3, the coordinate transformation is trained first by minimising $\Xi_{\mathbf{U}}$. The NN used within $\mathbf{U}$ consists of three inputs, two hidden layers each with 32 neurones and hyperbolic tangent activation functions, and two outputs. Evaluation of each neurone at the first hidden layer can be computed by Eq. (2.3) for $n = 1$ using σ as a hyperbolic tangent. The same evaluation at the neurone can be applied to the second layer and the output layer. Weight matrixes and bais vectors are the parameters that are the unknown coefficients $\Theta_{\mathbf{U}}$ and the Hopf bifurcation point is also an unknown coefficient. Hyper parameters, number of layers and neurones, are manually chosen to keep initial coordinate transformation before the optimisation to be invertible. 300 iterations with ADAM [89] and a learning rate of 0.01 were necessary to estimate the NN parameters $\Theta_{\mathbf{U}}$. A comparison between the bifurcation diagrams of the real and identified models shows that the hybrid M/ML model accurately captures the topological characteristics of the system (Fig. 5.3(a)). Phase portraits are shown in Figs. 5.3(b-1)–(d-1). They further demonstrate that an accurate transformation from the normal-form coordinates to the physical coordinates is achieved for the range of parameter values considered. The parameter value at the bifurcation point was estimated at $\mu = 0.02$, which is very close to the actual value 0.

Following the training of the coordinate transformation, Ω is estimated. The $\mathrm{NN}_{\Theta_\Omega}$ of the model Eq. (5.10) is set to include three inputs, two hidden layers each with 32 neurones and hyperbolic tangent activation functions, and 13 outputs ($n_h = 10$). The parameter of the model is estimated by minimising Ξ_Ω. The training was performed with NADAM [89]. 4000 iterations and a learning rate of 0.002 were necessary. Figs. 5.3(b-2)–(d-2) show a very good agreement between the time series of the reference and identified models. As the bifurcation parameter increases, the separation of the time scale becomes more pronounced, and errors become noticeable in the transition between the fast and slow portions of the time series (Fig. 5.3(d-2)). Similar observations can be made for the other state (not shown for conciseness).

5.4.2 Aeroelastic model

A 3-DOF aeroelastic system in Appendix A [1] is now considered to demonstrate the proposed method. This model is qualitatively representative of the physical system tested in Section 5.5.

This system has a subcritical Hopf bifurcation followed by a saddle-node bifurcation of

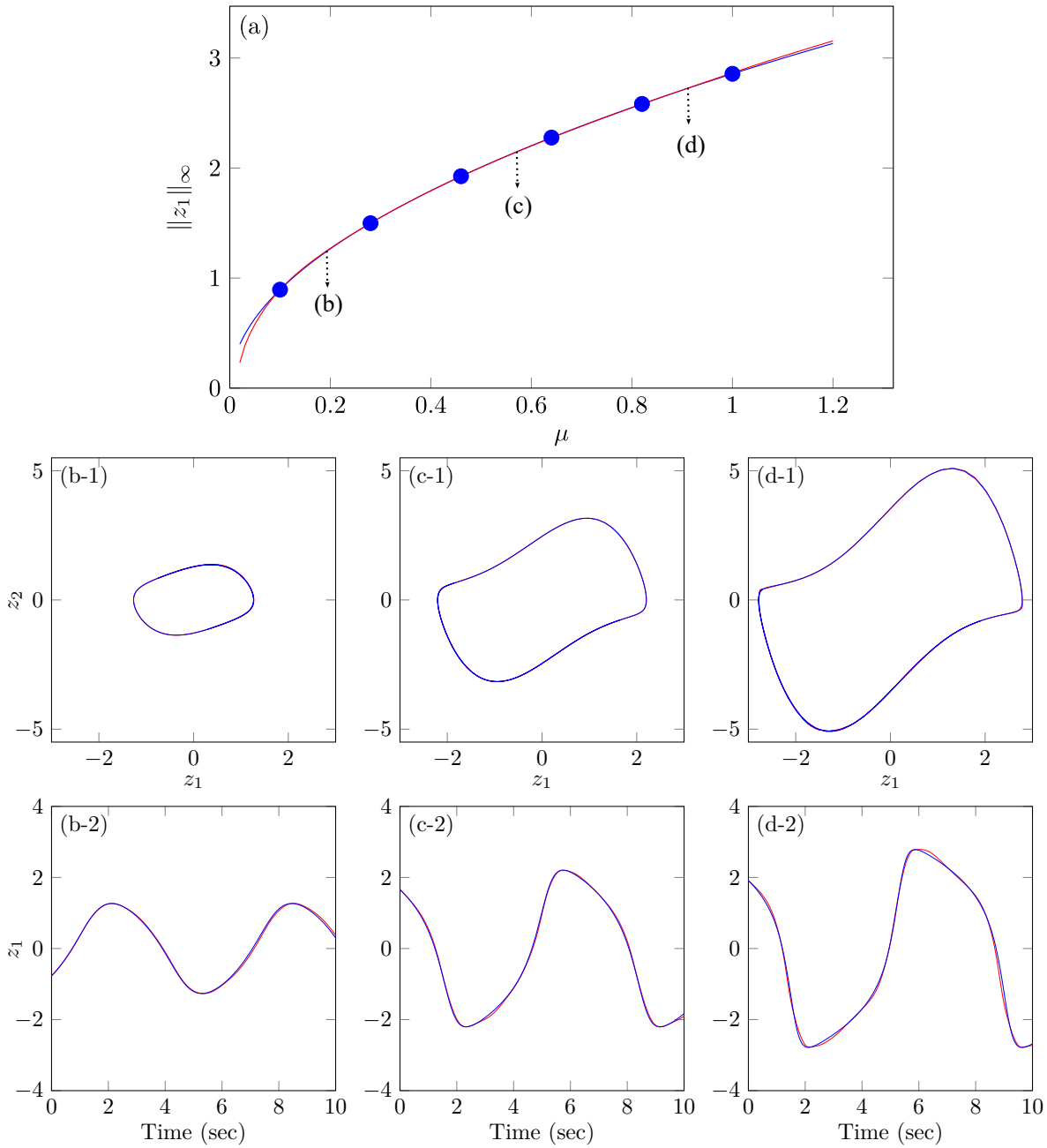

Figure 5.3: Comparison between the Van der Pol model (—) and the physics-guided ML model (—). (a) Bifurcation diagram where (●) are the LCOs used for model training. (b-1-d-1) Phase portrait and (b-2-d-2) time series at the untrained locations are reported on the bifurcation diagram.

periodic orbits. The training data set includes four LCOs recorded in the stable branch and four LCOs recorded in the unstable branch. As discussed in Section 5.5, in an experiment, stable and unstable LCOs can be measured directly using control-based continuation [51]. Here, unstable LCOs were obtained by simulating the model Eq. (A.1) under proportional derivative

feedback control to reproduce the process followed for experimental tests in Section 5.5. Each time series is recorded for one second with a sampling time of $0.001s$.

For this example, $\mathrm{NN}_{\Theta_\mathbf{U}}$ has two inputs, two hidden layers each with 21 neurones and hyperbolic tangent activation functions, and three linear outputs. Fig. 5.4(left) shows that the linear transformation allows the coordinate transformation to capture the overall orientation and size of the LCO, and Fig. 5.4(right) shows that $\mathrm{NN}_{\Theta_\mathbf{U}}$ further improves the accuracy of this coordinate transformation, leading to an excellent visual agreement between the LCO of the hybrid M/ML and reference models.

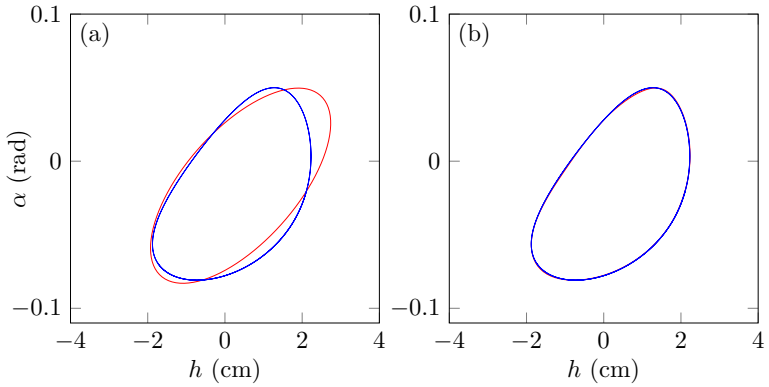

Figure 5.4: Comparison between the phase portraits of the aeroelastic model (—) and the hybrid M/ML model (—) for a stable LCO at $\mu = 15.5\ m/s$. Coordinate transformation (a) without and (b) with the neural network.

Fig. 5.5(a) shows there is an excellent agreement between the bifurcation diagrams computed from the reference and hybrid M/ML models. The bifurcation diagram of the trained model was computed by transforming 100 equispaced points on the periodic solutions of the normal-form model using $\mathbf{U}$. The identified values for the Hopf bifurcation point, μ_0 and the saddle-node bifurcation point, a_2, are 18.28 m/s and 3.64, respectively. This is in excellent agreement with the model values $\mu_0 = 18.28\ m/s$ and $a_2 = 3.65$. The phase portrait of the trained model shows good agreement with the model for both stable and unstable LCOs (Fig. 5.5(b-1)–(d-1)).

The oscillation speed Ω is modelled using Eq. (5.10). For this example, only the constant term in the Fourier expansion is kept such that $\Omega(\mathbf{u}, \mu) = \omega_0 + \mathrm{NN}_{\Theta_\Omega}(\mathbf{u}, \mu)$. The neural network consists of three inputs, two hidden layers with 31 neurones each, a hyperbolic tangent activation function, and one linear output. 300 iterations in ADAM [89] with a learning rate of 0.01 were necessary to train Ω to minimise Ξ_Ω. Fig. 5.5(b-2)–(d-2) show that the model captures the overall time series and frequency of the LCO for the range of wind velocities considered.

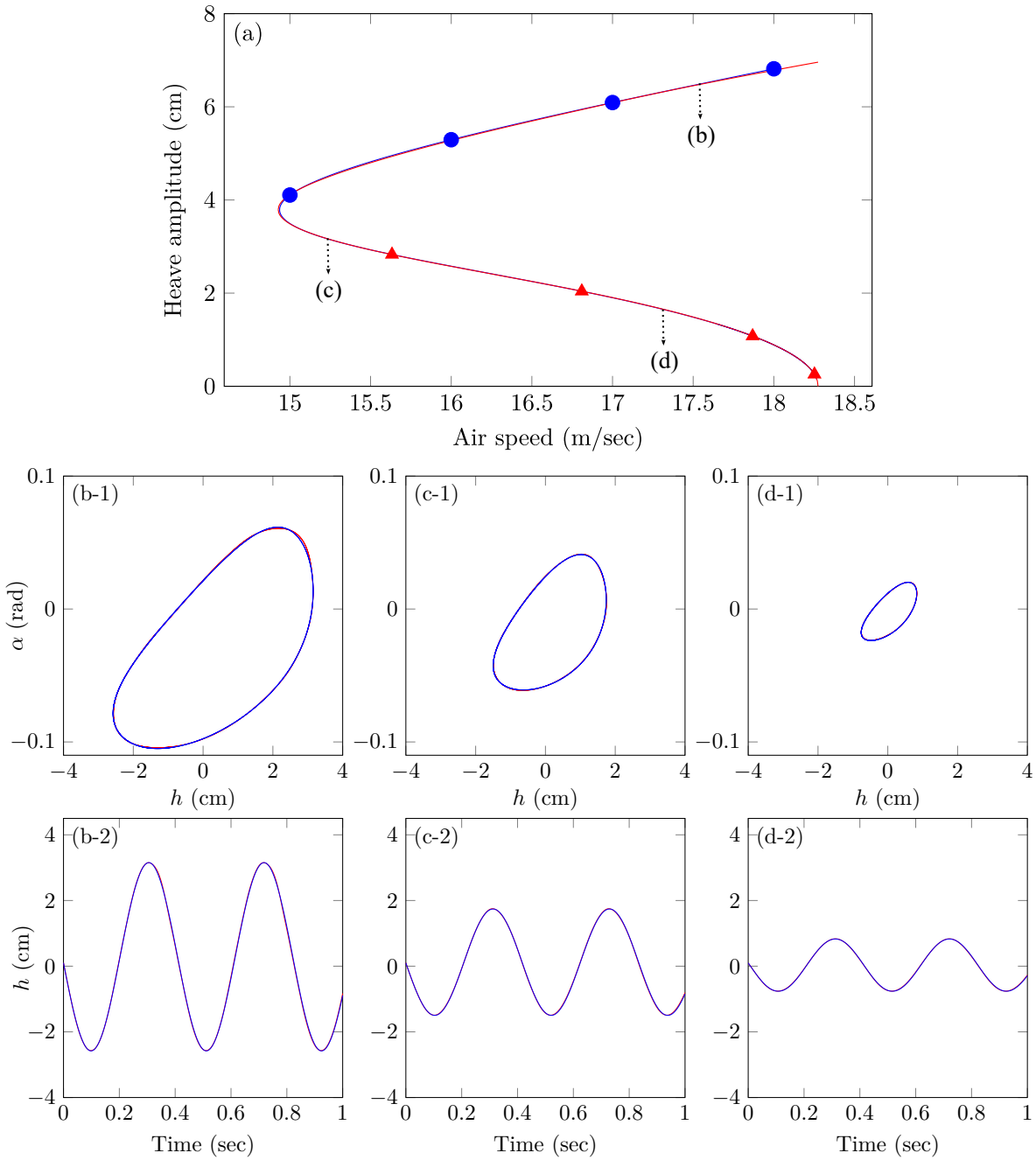

Figure 5.5: Comparison between the aeroelastic model (—) and the physics-guided ML model (—). (a) Bifurcation diagram (●) are stable LCOs and (▲) are unstable LCOs used for model training) (b-d) Phase portrait and (e-g)the time series at the locations reported on the bifurcation diagram.

5.5 Experimental demonstration on a flutter rig

The method developed in this chapter is now demonstrated on a physical aeroelastic system where the experiment is discussed in Section 3.3.3.

5.5.1 The hybrid M/ML model

The dynamics of this aeroelastic system is characterised by a subcritical Hopf bifurcation followed by a saddle-node bifurcation of cycles. Therefore, the mechanistic model used within the hybrid model is the one presented in Eq. (5.2) and already used in Section 5.4.2. Training data sets include four stable LCOs measured at $\mu = (14.9,\ 15.6,\ 16.5,\ 17.3)\ m/s$, and three unstable LCOs measured at $\mu = (14.9,\ 15.6,\ 16.5)\ m/s$. The time series includes 6000-time points per LCO, which represents approximately 12 oscillation periods. To train the oscillation speed, time series were down-sampled to 1000 samples to reduce the computational cost of the training.

For the coordinate map $\mathbf{U}_{12}$, a neural network $\mathrm{NN}_{\Theta_\mathbf{U}}$ with three inputs, two outputs, and two hidden layers each with 11 neurones and hyperbolic tangent activation functions was used. First 1000 ADAM iterations using a 0.001 learning rate followed by 10000 BFGS iterations with a 0.0001 learning rate were necessary to minimise $\Xi_\mathbf{U}$ and find μ_0, a_2 and network parameters $\Theta_\mathbf{U}$.

Fig. 5.6 compares the bifurcation diagram of the hybrid M/ML model with the experimentally measured LCOs. Qualitatively good agreement with the data is obtained despite the limited number of LCOs used for model training. The Hopf bifurcation point is estimated at $\mu_0 = 17.67\ m/s$ and the saddle-node bifurcation point at $14.66\ m/s$. Overall, the trained model accurately predicts the phase portrait of the stable and unstable LCOs, as shown in Fig. 5.7. In the phase portraits, the line associated with the experimentally measured LCOs appears thicker than that from the model predictions. This is an illusion that comes from the presence of multiple oscillation periods in the recorded data and the unavoidable differences that exist between periods due to the presence of noise in the measurements.

For the identification of Ω, a model similar to that used in Section 5.4.2 is considered. The neural network $\mathrm{NN}_{\Theta_\Omega}(\mathbf{u}, \mu)$ includes three inputs, a single linear output, two hidden layers with 21 neurones each, and hyperbolic tangent activation functions. 300 iterations in ADAM with a learning rate of 0.01 were necessary to minimise Ξ_Ω. The time series presented in Fig. 5.8 shows that the model captures the frequency of the measured LCOs. The amplitude error visible in the bifurcation diagram is also clearly visible in the time series.

One potential issue with ML model training is overfitting. This is illustrated in Fig. 5.9 where the model was trained using different initial parameter values and different hyperparameters (number of iterations and learning rate). Although the overall model prediction error is small at the data points, the model presents a large variability between them, which is symptomatic

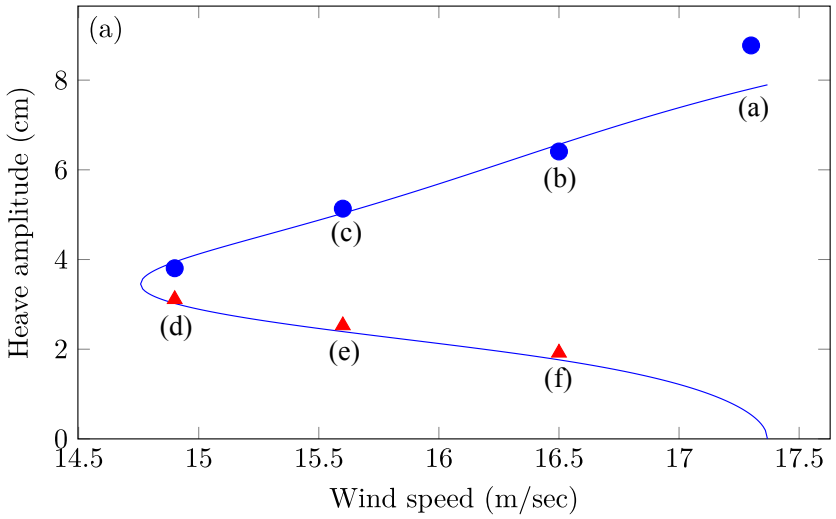

Figure 5.6: Comparison between the bifurcation diagram obtained from the hybrid M/ML model with increased model accuracy (—) and the stable (●) and unstable (▲) LCOs used for model training. Labels (a)-(f) denote the corresponding phase portraits and time series plots in Fig. 5.7 and Fig. 5.8, respectively.

of overfitting. To reduce overfitting and obtain the results presented in Figures 5.6 – 5.8, some hyper-parameters, such as the number of iterations, were manually tuned. Approaches that promote parameter sparsity [57] or a formal optimisation of hyperparameters [16] were not carried out due to associated computational costs and the overall lack of data. Note that the use of physics here, through the model structure (5.2) and the use of linear transformations in $\mathbf{U}_{12}$ can also be viewed as regularisation techniques that reduce ML model complexity and hence help in reducing overfitting.

To assess the robustness of the identified model with respect to the training data, model training was also performed with four different data sets, each with one of the LCO data points removed. This approach is inspired by the leave-one-out cross-validation technique and chosen due to the small number of data points available in the parameter space. Fig. 5.10 shows the bifurcation diagrams obtained after removing the different data points. The colour of the bifurcation curve matches the colour of the data point that was removed from the training data set. The dashed black bifurcation curve was obtained by including all data points in the training set. The phase portraits and time series shown in Fig. 5.10 illustrate the performance of the model at the removed data point. Although most bifurcation curves appear similar, removing the stable LCO in blue appears to have a significant influence on the location of the saddle-node bifurcation and more generally on the bifurcation curve in that area. This also affects the quality of the oscillation speed model Ω, which is unable to capture the LCO oscillation frequency adequately (see Fig. 5.10(c-2)). Overall, these results suggest that sufficient training data near bifurcation points (saddle-node and Hopf) is needed to build a robust model.

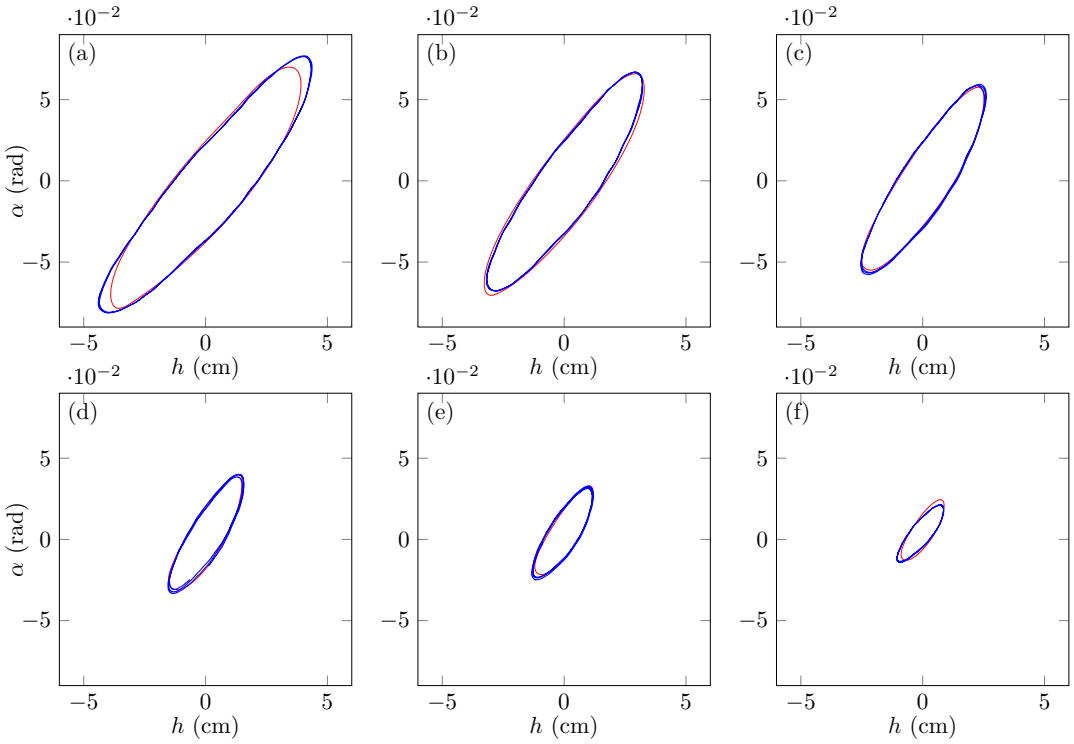

Figure 5.7: Comparison of phase portraits between the measured LCOs (——) and the hybrid M/ML model (——). (a) stable LCO at wind speed 17.3 m/sec, (b) stable LCO at wind speed 16.5 m/sec, (c) stable LCO at wind speed 15.6 m/sec, (d) unstable LCO at wind speed 14.9 m/sec, (e) unstable LCO at wind speed 15.6 m / sec, and (f) unstable LCO at wind speed 16.5 m/sec.

Fig. 5.11 presents the trained mapping $\mathbf{U}_{12}$. Fig. 5.11(a, b) show the transformation $\mathbf{U}_{12}$ for $\mu = 15.0$, and Fig. 5.11(c,d) shows the transformation $\mathbf{U}_{12}$ for $\mu = 17.5$ m/s. The blue dotted lines and the red solid lines correspond to unstable and stable LCOs, respectively. The coordinate transformations are smooth transformations and locally invertible. The visible curvature shows that the transformations are also nonlinear. As discussed in Section 5.3.2, the presence of an initial linear coordinate transformation in (5.8) was essential. An NN alone was unable to produce topologically equivalent closed curves and obtain a locally invertible transformation near the bifurcation point. Models with significant overfitting, such as the one in Fig. 5.9, were also found to result in poorly or even noninvertible transformations.

5.6 Conclusions

In this chapter, we have proposed a new hybrid modelling approach for physical systems with a Hopf bifurcation. At its core, it uses a mechanistic model, in the form of a normal form-like model, to capture the phenomenology of the physical system. A data-driven, machine-learnt

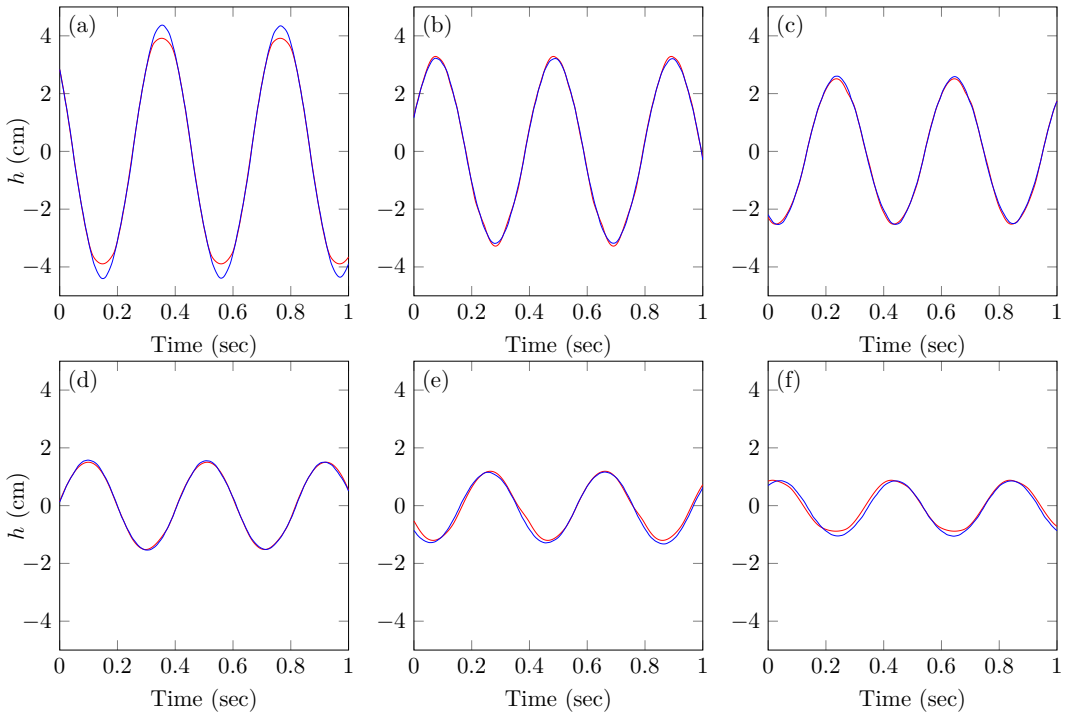

Figure 5.8: Comparison of heave time series between the measured LCOs (—) and the hybrid M/ML model (—). (a) stable LCO at wind speed 17.3 m/sec, (b) stable LCO at wind speed 16.5 m/sec, (c) stable LCO at wind speed 15.6 m/sec, (d) unstable LCO at wind speed 14.9 m/sec, (e) unstable LCO at wind speed 15.6 m/sec and (f) unstable LCO at wind speed 16.5 m/sec.

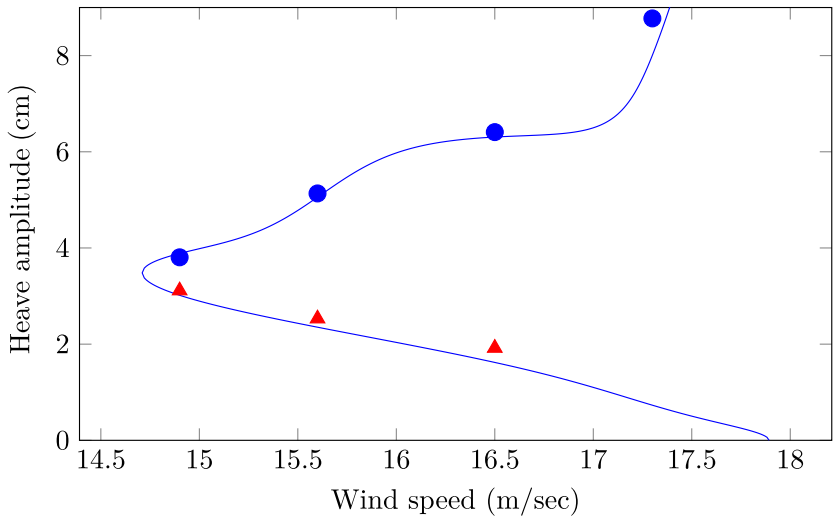

Figure 5.9: Illustration of model overfitting. Bifurcation diagram obtained from the hybrid M/ML model (—), stable (●) and unstable (▲) LCOs used for model training.

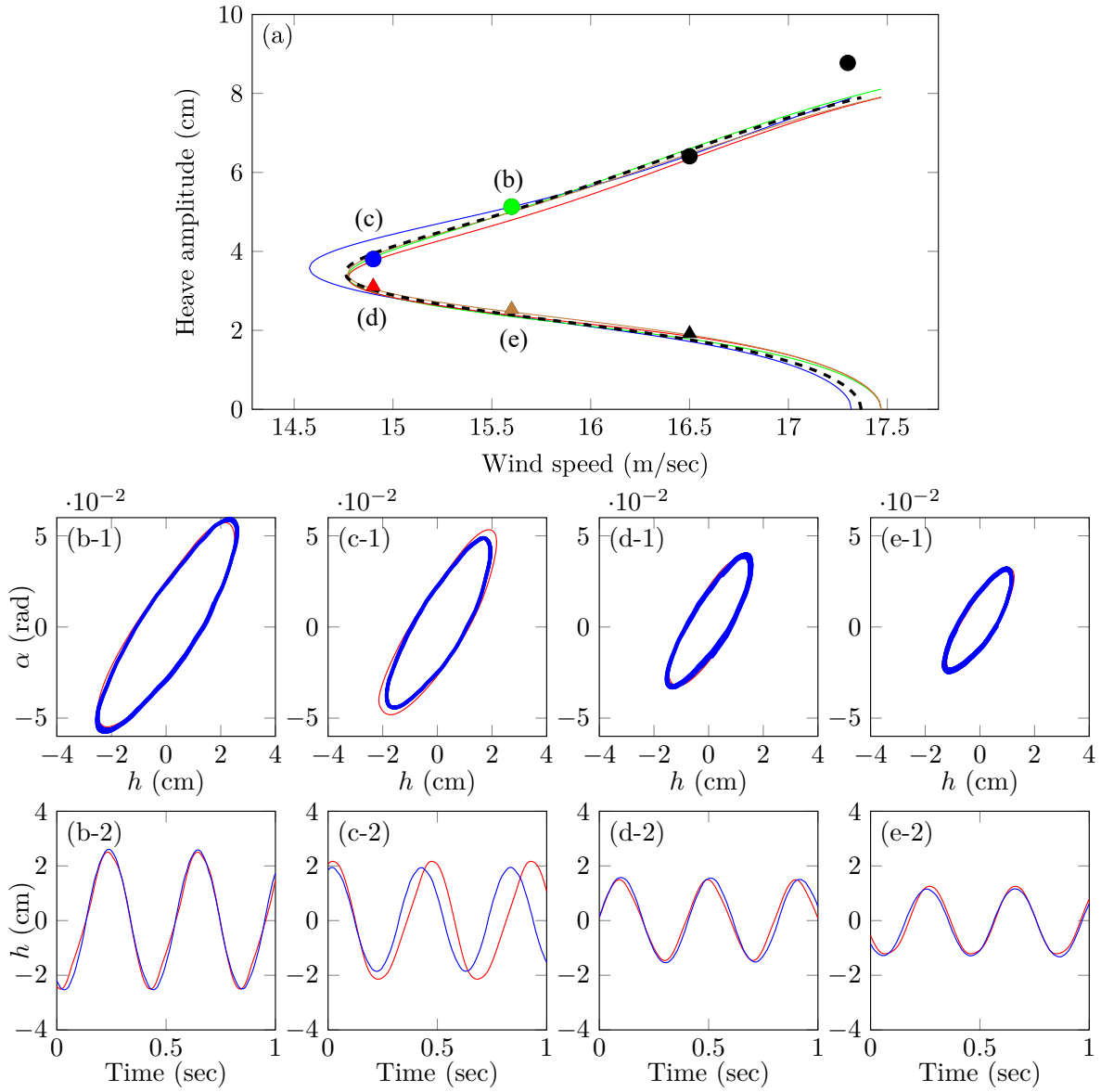

Figure 5.10: Effect of excluding one data point from the training data set on the hybrid M/ML model accuracy. (a) Bifurcation diagrams obtained when removing the data point of the same colour. For example, the blue bifurcation curve is obtained when the model is trained with a data set that excludes the blue point. (- - -) Bifurcation diagram obtained from a model trained with all measured data without removing any data points. (b-1) – (e-1) Prediction of the phase portrait at the excluded data point. (b-2) – (e-2) Prediction of time series at the excluded data point.

model is then used to map the mechanistic model predictions onto the measured data. Our method was first demonstrated with numerical data collected on a Van der Pol oscillator and an aeroelastic model, and then with experimental data collected on a flutter rig during wind tunnel tests. The hybrid mechanistic/machine-learnt models obtained with our method were

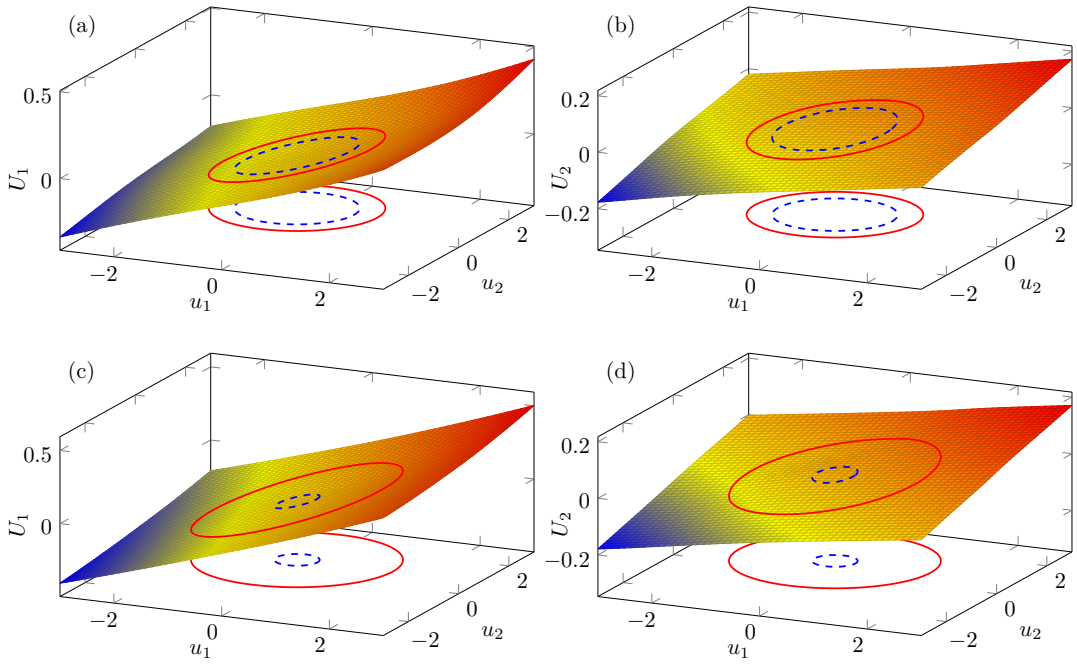

Figure 5.11: Mapping $\mathbf{U}_{12}(\mathbf{u},\mu) = (U_1(\mathbf{u},\mu), U_2(\mathbf{u},\mu))$ between normal form and measured coordinates. (a) U_1 at μ=15.0 m/sec, (b) U_2 at μ=15.0 m/sec, (c) U_1 at μ=17.0 m/sec and (d) U_2 at μ=17.0 m/sec.

shown to quantitatively capture the bifurcation diagrams of the different systems as well as their time evolution, even in the presence of multiple time scales and noise.

The proposed method has several advantages, such as being data-driven while being able to work with a limited number of measured states and data. It also requires only knowledge of the bifurcation structure of the system and is thus applicable to a priori any system with a Hopf bifurcation. Replacing the current mechanistic model with a more detailed model of the physical system could improve the accuracy of the obtained model, while also simplifying the training of the mapping. However, this will probably come at the cost of having a more application-specific modelling methodology. A more systematic approach to handling overfitting during ML model training is also required to make the method more systematically applicable. As the model is derived using LCO data only, the obtained hybrid-mechanistic/machine-learnt model reproduces the long-term behaviour of the physical system but is generally unable to accurately capture its transient dynamics. Future work should look at including transient data in the modelling approach. One option is to use CBC to stabilise unstable LCOs of the system and then turn off the control to measure response repelling from the unstable LCOs as shown in Fig. 3.18. Measured data sets converging to a stable periodic branch will provide information about the flow between the unstable solutions to Ω, and data sets that converge to equilibrium will provide information about the flow near the equilibrium. It will be possible to generate transient data on the centre manifold, making the trained model richer using this technique.

Finally, the principles of the proposed method are extremely general and could therefore be applied to systems with other types of bifurcation by changing the mechanistic model.

The hybrid mechanistic/machine-learnt models obtained with our method can have multiple uses. The machine-learnt part of the model could be exploited to improve understanding of the physical system of interest and provide new insights into the derivation of more accurate mechanistic models. The ability of the proposed models to reproduce the unstable part of the bifurcation diagram also has the potential to analyse stability boundaries and basins of attraction of physical systems, or help in reducing the cost of experimental methods such as CBC. Finally, the hybrid mechanistic/machine-learnt models developed here to establish a rigorous framework to combine known physics with experimental and/or operational data and could therefore be used as digital twins for nonlinear systems.

Data and code availability

Julia package developed for study in this chapter is available in repository ML Hopf.jl.

CHAPTER 6

Bifurcation-based data-driven modelling of ODEs with spectral-submanifolds

In this chapter, we

- develop bifurcation-based data-driven models of parameter-dependent ODEs with spectral-submanifolds,
- use knowledge of the application area, namely the existence and the dimension of an invariant manifold,
- demonstrate the developed modelling method on synthetic data sets generated from a harmonically-forced nonlinear coupled oscillator and experimental data discussed in Section 3.3.3.3.

6.1 Introduction

Our main objective here is to develop data-driven modelling of harmonically-forced damped mechanical systems using domain knowledge– the existence of invariant manifolds and the dimension of invariant manifolds. Specifically, we use the existence of a 2-dimensional invariant manifold as the core information of modelling to capture the dynamics of the frequency response of a harmonically forced system. In this chapter, the theoretical background of data-driven modelling is the invariant manifold theory of damped mechanical systems (Section 2.3.2) [36, 68, 101, 104, 105] which is also known as spectral submanifolds (SSMs) and nonlinear normal modes (NNMs) [66]. SSMs and NNMs can be understood as nonlinear extensions of linear modal subspaces. Also, a study in [36] shows that autonomous SSMs are smoothly perturbed by small harmonic forcing, where the phase variable is an additional parameterisation

variable of SSMs. Therefore, we will denote the invariant manifold of harmonically-forced damped mechanical systems as SSMs in this chapter.

Harmonically forced systems are prevalent in many applications, such as cars, aircraft, and wind turbines, where rotating components are present. Rotating components are typically the main source of excitation, and a system's dynamics depend on the rotating speed, which coincides with the excitation frequency and amplitude. Predictions of harmonically-forced systems are easy to analyse using linear modal superposition when the system's nonlinearity is small enough [93]. We cannot use linear modal superpositions when the system's nonlinearity is not neglectable, which is more challenging than linear systems in predicting and modelling. Also, nonlinear systems often show complex frequency responses such as bistability. Therefore, our primary goal is to develop data-driven models of harmonically-forced nonlinear mechanical systems that accurately predict the complex frequency response of nonlinear systems.

Data-driven modelling of systems with SSMs was first studied in [97], initially training a NARMAX [24] model from a delay-embedded resonant decay response. The dimension of the delay embedding was selected using Taken's delay embedding theorem [98]. Similarly, Canedese [21] trained the coordinates of the SSMs using a linear embedding, assuming a graph representation of an invariant manifold in embedding space and also using a resonant decay response. Szalai [96] improved the data-driven modelling of the system with an asymptotically stable equilibrium by using invariant foliations theory, which does not require the training data sets to be strictly on SSM.

The fundamental difference between this chapter and previous studies is that we do not train the manifold itself as a subspace of state space. Previous studies trained the invariant manifold of a delay-embedded observation space and trained the dynamics on that manifold afterwards. Instead, we train the dynamics on the invariant manifold directly from the measured bifurcation diagram. This simplification reduces the possibility of propagating error through manifold learning in the initial training stage. Moreover, we use kernel ridge regression to train the optimised model by controlling the fitting and smoothing of the model within the sparse data sets. This is different from studies using neural networks [34, 53] and polynomials [21, 97], which makes it challenging to optimise the trade-off between fitting and smoothing model. It should also be noted that this study uses the forced response obtained from the CBC experiment as input, while other related studies [21, 97] use unforced responses (resonant decay) to train the model.

In Section 6.2, we first briefly discuss the SSM theory and explain how to transform the measured forced response into input-output pair data for kernel ridge regression. We investigate the data-driven modelling method developed from two modelling examples in Section 6.3. One is a data-driven model trained from numerically generated FRCs of a two-dimensional nonlinear spring-mass-damper model. The second data-driven model is trained from experimentally measured S-curves of the nonlinear electromagnetic oscillator discussed in Chapter 3.

6.2 Training ML model for system with invariant manifold

We will discuss the approach taken here to train a data-driven model for harmonically forced systems. Specifically, we assume the existence of a harmonically-forced invariant manifold that represents the overall dynamics of the experiment and train the reduced dynamical system on this invariant manifold. The difference between the approach taken in the self-excited system, Chapter 5, is that there is a harmonic force that can be used as input for data-driven modelling.

6.2.1 Invariant manifold of forced mechanical systems

We consider a dynamical system with harmonic forcing governed by an N-dimensional ODE

$$\dot{\mathbf{x}} = A\mathbf{x} + \mathbf{G}(\mathbf{x}) + \varepsilon \mathbf{f}\cos(\phi), \tag{6.1}$$

where $A \in \mathbb{R}^n \times \mathbb{R}^n$ is a matrix with all eigenvalues having a negative real part, $\mathbf{G} : \mathbb{R}^N \to \mathbb{R}^N$ is a nonlinear function with $\mathbf{G}(0) = 0$, $D\mathbf{G}(0) = 0$, $\mathbf{f} \in \mathbb{R}^N$ is a direction vector of the harmonic force and $\phi \in \mathbb{S}^1$ is a phase variable of the harmonic force with constant frequency $\Omega \in \mathbb{R}$, i.e. $\dot{\phi} = \Omega$, and $\varepsilon \ll 1$ is a small parameter. The origin ($\mathbf{x} = 0$) is an asymptotically stable equilibrium of $\dot{\mathbf{x}} = A\mathbf{x} + \mathbf{G}(\mathbf{x})$.

We assume that statements 1-4 of Theorem 2.2 hold for a 2-dimensional spectral subspace E with corresponding spectrum λ_l and $\bar{\lambda}_l$ (see Section 2.3.2 for details). The theory of invariant manifolds for harmonically-forced systems with asymptotically stable equilibrium (Theorem 2.2) guarantees the existence of an invariant manifold W, of Eq. (6.1). Specifically, we consider a harmonically-forced invariant manifold that depends on a two-dimensional parameterisation variable $\mathbf{z} \in \mathbb{C}^2$ (single modal subspace) and a phase variable ϕ [14]

$$\mathbf{x} = \mathbf{W}(\mathbf{z}, \phi),\ \mathbf{z} \in \mathbb{C}^2, \tag{6.2}$$

where $\mathbf{W} : \mathbb{C}^2 \times S^1 \to \mathbb{R}^N$ is a parameterisation of the invariant manifold W. We further assume that the dynamics of W adequately represent the dynamics of the physical experiment with the near-resonant condition $\Omega \approx \mathrm{Im}(\lambda_l)$ satisfied.

The reduced dynamics $\mathbf{R} : \mathbb{C}^2 \times S^1 \to \mathbb{C}^2$ on this manifold can be represented as

$$\dot{\mathbf{z}} = \mathbf{R}(\mathbf{z}, \phi), \tag{6.3}$$

and we have the invariance condition on W as Eq. (2.20).

6.2.2 Observation and the bifurcation diagram

Note that we should consider the component of the forcing vector that falls into the subspace, E, as we are considering an invariant manifold tangent to E [14]. We will denote the amplitude

of harmonic forcing projected in the tangential direction of the invariant manifold as Γ in this chapter.

FRC is a curve of a periodic response with varying excitation frequency Ω. We cannot parameterise the FRCs by Ω when there is a bistable region. Therefore, the general way to parameterise the FRC is to choose another parameterisation variable, s, such as the arclength [47] used in the numerical continuation. Moreover, we will denote $\mathbf{z}_s^\Gamma(t)$ as a periodic solution of Eq. (6.3) with a parametrised frequency $\dot{\phi} = \Omega_s$ at a fixed Γ.

A scalar observation, φ, typically tracks FRC in the experiment, where we assume that it depends on the parameterisation vector $\mathbf{z}$ of the invariant manifold W as

$$\varphi = \varphi(\mathbf{z}). \tag{6.4}$$

We seek φ as in Eq. (6.4) since the measured response is on the invariant manifold, W, in our setting. Plotting the maximum amplitude of the observed periodic response A_s that has the form

$$A_s = \max_{t\in[0,T_s)} |\varphi(\mathbf{z}_s^\Gamma(t))|, \tag{6.5}$$

is a convenient way to plot the FRCs where $T_s = 2\pi/\Omega_s$ is a period of the periodic response. In this case, the point on the FRCs is parametrised by s as (Ω_s, A_s).

Similarly, we can parametrise the periodic response by fixing the forcing frequency Ω and changing the forcing amplitude Γ_s that depends on s. We call this bifurcation diagram the S-curve (Γ_s, A_s).

In this chapter, we will identify reduced dynamics, $\mathbf{R}(\mathbf{z}, \phi)$, and observation, φ, using experimentally obtained FRCs or S-curves.

6.2.3 Data-driven modelling of reduced dynamics on the invariant manifold

In this subsection, we transform the data-driven modelling of a dynamical system into a straightforward input-output pair regression problem suitable for kernel ridge regression. In addition, we will explain the ML framework used in this chapter.

6.2.3.1 Reduced dynamics on the invariant manifold

As in Section 2.3.2, we can express reduced dynamics $\mathbf{R}(\mathbf{z}, \phi)$ as

$$\mathbf{R}(\mathbf{z}, \phi) = \mathbf{R}_0(\mathbf{z}) + \varepsilon \mathbf{r}_1^0(\phi) + \mathcal{O}(\varepsilon|\mathbf{z}|, \varepsilon^2), \tag{6.6}$$

where $\mathbf{z} = [z, \bar{z}]^T$, $\mathbf{R}_0$ corresponds to the autonomous part of the reduced dynamics, and $\mathbf{r}_1^0$ corresponds to the harmonic force. Deriving a reduced-order model from Eq. (2.15) is finding

unknown coefficients of the $\mathbf{R}$ from the invariance equation Eq. (2.20). The typical power series expression of $\mathbf{R}_0$ upto order $2M+1$ [14, 97] is

$$\begin{aligned} \dot{z} &= \lambda_l z + \sum_{m=1}^{M} \beta_m z^{m+1} \bar{z}^m, \\ \dot{\bar{z}} &= \bar{\lambda}_l z + \sum_{m=1}^{M} \bar{\beta}_m z^m \bar{z}^{m+1}. \end{aligned} \tag{6.7}$$

The form of Eq. (6.7) ensures a broad domain of validity for reduced-order modelling by avoiding small denominators that arise when solving the invariance equation Eq. (2.20) (see [97] for details).

Here, we introduce a different functional form of reduced dynamics from Eq. (6.7), which aims to learn dynamics directly from forced responses and to impose higher model flexibility. Note that the expression of reduced dynamics in the invariant manifold Eq. (2.30), is not unique, and any coordinate transformation to $\mathbf{z}$ will give a different expression of the reduced dynamics.

In [21], the parametrisation of the invariant manifold was trained from the delay embedded space of a scalar observable, and the reduced dynamics were identified afterwards. Reduced dynamics trained from the embedded delay space are not necessarily rotationally symmetric; therefore, the near-identity transformation was introduced to derive reduced dynamics in the form of Eq. (6.7). However, we take a more straightforward approach in data-driven modelling where the main idea is to focus on reproducing the measured bifurcation diagram (S-curves or FRCs) using the reduced dynamics.

We assume the existence of parametrisation of invariant manifold, $\mathbf{z} = [z, \bar{z}]^T$, where the reduced dynamics is rotationally symmetric where the quadratic terms are removed using certain coordinate transformation, and the coefficients of the higher-order polynomials are Ω-dependent as

$$\begin{aligned} \dot{z} &= \lambda_l z + \sum_{m=1}^{M} \gamma_m(\Omega) z^{m+1} \bar{z}^m, \\ \dot{\bar{z}} &= \bar{\lambda}_l z + \sum_{m=1}^{M} \bar{\gamma}_m(\Omega) z^m \bar{z}^{m+1}, \end{aligned} \tag{6.8}$$

where γ_m is Ω-dependent coefficients of polynomial where Ω is the freqency of the external force. Transforming Eq. (6.8) into polar coordinates, $z = \rho e^{i\theta}$, we have

$$\begin{aligned} \dot{\rho} &= a(\rho, \Omega) = \mathrm{Re}(\lambda_l)\rho + \sum_{m=1}^{M} \mathrm{Re}(\gamma_m(\Omega))\rho^{2m+1}, \\ \dot{\theta} &= b(\rho, \Omega) = \mathrm{Im}(\lambda_l)\rho + \sum_{m=1}^{M} \mathrm{Im}(\gamma_m(\Omega))\rho^{2m+1}. \end{aligned} \tag{6.9}$$

Note that the functional form of Eq. (6.9) is different from the typical form of reduced dynamics on SSMs in Eq. (6.7), which has Ω-dependent autonomous dynamics. However, it is possible to transform Eq. (6.7) to Eq. (6.9) if the Ω-dependent coordinate transformation is applied to Eq. (6.7). Furthermore, the structure of Eq. (6.9) offers greater flexibility in the model, as data-driven modelling of reduced dynamics without Ω-dependent terms was only able to capture frequency responses of the small frequency range, as shown in [11].

Adding $\mathbf{r}_1^0$ (see [14] for details of the derivation from the external force $\mathbf{f}$) to Eq. (6.9), we have the forced reduced dynamics on the SSMs as

$$\begin{aligned} \dot{\rho} &= a(\rho, \Omega) + \Gamma \sin(\psi), \\ \dot{\theta} &= b(\rho, \Omega) + \frac{\Gamma}{\rho} \cos(\psi), \\ \dot{\phi} &= \Omega, \end{aligned} \tag{6.10}$$

where $\psi = \theta - \phi$ is the phase difference between the harmonic force and the response on the invariant manifold, $\phi = \Omega t$ is the phase of external forcing.

The periodic solutions of Eq. (6.10) correspond to fixed points of the following equation

$$\begin{aligned} &a(\rho, \Omega)^2 + (b(\rho, \Omega) - \Omega)^2 \rho^2 - \Gamma^2 = 0, \\ &b(\rho, \Omega) + \frac{\Gamma}{\rho} \cos(\psi) - \Omega = 0. \end{aligned} \tag{6.11}$$

For example, consider an FRC parameterised by s with a fixed Γ. The periodic response $\mathbf{z}_s^\Gamma(t)$ at $\Omega = \Omega_s$ corresponds to a fixed point (ρ_s, ψ_s) of Eq. (6.11) as

$$\mathbf{z}_s^\Gamma(t) = (\rho_s e^{i(\Omega_s t + \psi_s)}, \rho_s e^{-i(\Omega_s t + \psi_s)}). \tag{6.12}$$

We can train $a(\rho, \Omega)$ and $b(\rho, \Omega)$ by solving a regression problem if we know the fixed points $(\rho_1, \psi_1), \ldots, (\rho_n, \psi_n)$, of Eq. (6.11). Here, we aim to find fixed points, $(\rho_1, \psi_1), \ldots, (\rho_n, \psi_n)$, from measured bifurcation diagram (S-curves or FRCs) discussed in Section 6.2.2.

Let the function $A(\rho)$ denote the maximum output of $|\varphi|$ using the points in the trajectory of the periodic solution (Eq. (6.12)) as input, which can be defined as

$$A(\rho) = \max_{\theta \in [0, 2\pi)} |\varphi(\rho e^{i\theta}, \rho e^{-i\theta})|. \tag{6.13}$$

Note that the output of A corresponds to a point on the measured FRC of an experiment discussed in Section 6.2.2, which is the amplitude of the measured periodic response. The idea of data-driven modelling in this chapter is to locate the fixed points of Eq. (6.11) using A, which is measured in the experiment. Therefore, we assume that the following condition is satisfied by choosing the coordinate system $\mathbf{z}$ appropriately as

$$A(\rho) = \rho. \tag{6.14}$$

Eq. (6.14) means that we can extract the amplitude of periodic solution ρ directly from the amplitude of the measured periodic response A. We can train the reduced dynamics from the fixed points, $(A_1, \psi_1), \ldots, (A_n, \psi_n)$, of Eq. (6.11) where $(A_1, \psi_1), \ldots, (A_n, \psi_n)$ are measured data.

We expect the existence of a particular coordinate system of invariant manifold that satisfies Eq. (6.14) will depend on several mathematical conditions of observation φ. For example, if there exists a coordinate system that satisfies $\frac{dA(\rho)}{d\rho} \neq 0$, i.e. maximum measured amplitude A is a monotonic function of ρ, coordinate transformed by the transition map $(\rho, \theta) \mapsto (A(\rho), \theta)$ will satisfy Eq. (6.14). However, we assume the existence of a specific coordinate system that satisfies Eq. (6.14) without mathematical justification, such as providing a condition for A to be a monotonic function. This significantly simplifies the input-output map for the data-driven modelling problem explained in Section 6.2.3.2. Providing mathematical conditions that justify Eq. (6.14) is left for future work and not the scope of the thesis.

6.2.3.2 Data-driven modelling of the reduced dynamics

The phase-lag, ψ, between the phase of the harmonic forcing, ϕ, and the response of the reduced dynamics, $\mathbf{z}_s^\Gamma$, depends on the function $b(\rho, \Omega)$. We assume that the fundamental harmonic of the observed periodic response, $\varphi(\mathbf{z}_s^\Gamma(t))$, has an identical phase to the periodic response $\mathbf{z}_s^\Gamma(t)$.

We can train $b(\rho, \Omega)$ from the measured phase difference by constructing samples of input-outputs of $b(\rho, \Omega)$ using the following equation

$$p_j = \Omega_j - \frac{\Gamma_j}{\rho_j} \cos(\psi_j), \tag{6.15}$$

where j is the index of the measured periodic response, p_j is j-th output of $b(\rho, \Omega)$, ψ_j is j-th measured phase difference between force and the fundamental harmonic of observation, ρ_j is measured j-th amplitude, and Ω_j is j-th forcing frequency, and Γ_j is j-th forcing amplitude. Note that Γ_j, which is the amplitude of the force tangent to the invariant manifold, is not directly measurable. However, we assume that Γ_j is identical to the measurable quantity of the external force by choosing the coordinate system $\mathbf{z}$ appropriately. For example, amplitude of the force tangent to the SSM is proportional to the measured forcing amplitude. We assume parametrisation of the SSM is appropriately scaled such that Γ_j is identical to the measured forcing amplitude.

The expression of the invariant manifold and the reduced dynamics in SSM theory [36] takes polynomials. However, we assume $a(\rho, \Omega)$ and $b(\rho, \Omega)$ can be successfully approximated using functions in RKHS discussed in Definition 2.1, which makes data-driven modelling much

easier with input-output relations presented in Eq. (6.15). Also, we can easily control the model complexity by tuning the kernel's hyperparameters to avoid overfitting.

We can define a kernel-ridge regression problem with loss $\mathcal{L}$ as

$$\mathcal{L} = \frac{1}{n}\sum_{j=1}^{n}(b(\mathbf{x}_j) - p_j)^2 + \lambda\|b\|^2_{\mathcal{H}_k}, \tag{6.16}$$

where $\|\cdot\|^2_{\mathcal{H}_k}$ is a square norm defined in RKHS [45]. We find $b(\rho, \Omega)$ in the form of

$$b(\cdot) = \sum_{j=1}^{n}\alpha_j k(\cdot, \mathbf{x}_j), \tag{6.17}$$

where $\mathbf{x}_j = [\rho_j, \Omega_j]^{\mathrm{T}}$ is j-th column of an input matrix $\mathbf{x} \in \mathbb{R}^{2\times n}$, α_j is j-th component of the vector $\boldsymbol{\alpha} = [\alpha_1, \ldots, \alpha_n]^{\mathrm{T}}$, $k : \mathcal{X} \times \mathcal{X} \to \mathbb{R}$ is a postivie definite kernel, and $\mathcal{X} \subset \mathbb{R}^2$ is the input space. $\boldsymbol{\alpha}$ that minimises Eq. (6.16) is computed as [45]

$$\boldsymbol{\alpha} = (k_{\mathbf{xx}} + n\lambda I_n)^{-1}\mathbf{p}, \tag{6.18}$$

where $k_{\mathbf{xx}} \in \mathbb{R}^{n\times n}$ is the kernel matrix, λ is a regularisation constant, $\mathbf{p} = [p_1, \ldots, p_n]^{\mathrm{T}}$ is an output vector where p_j is a j-th output of b defined in Eq. (6.15). Hyperparameters [81] (length scale, scale factor, etc.) of the kernel k and the regularisation parameter λ are optimised by minimising the square loss $\mathcal{L}$.

Similarly, we can construct the j-th input-output map of $a(\rho, \Omega)$ from Eq. (6.11) as

$$a(\rho_j, \Omega_j) = -\sqrt{{\Gamma_j}^2 - (b(\rho_j, \Omega_j) - \Omega_j)^2\rho_j^2}, \tag{6.19}$$

to train $a(\rho, \Omega)$ using kernel ridge regression with the same procedure as in the training function $b(\rho, \Omega)$. Note that the sign in Eq. (6.19) corresponds to the stable equilibrium ($\rho = 0$), and we exclude the case of sign change in Eq. (6.19), which assumes the nonexistence of limit cycle oscillations without forcing.

6.2.3.3 Data-driven modelling of an observation

Once we have trained $a(\rho, \Omega)$ and $b(\rho, \Omega)$, observation, φ, can be trained by constructing an input-output map from the measured time series using kernel ridge regression. Let (ρ_j, ψ_j) be a fixed point of Eq. (6.11) at $\Omega = \Omega_j$, then the input-output map of φ is

$$\varphi(\rho_j \cos(\Omega_j t_i + \psi_j), \rho_j \sin(\Omega_j t_i + \psi_j)) = y_i, \tag{6.20}$$

where subindex i corresponds to the index of each time series of j-th periodic response at $\Omega = \Omega_j$ in an FRC. We can train φ using multiple periodic responses using the input-output map constructed from Eq. (6.20). The rest of the training procedure is identical to $a(\rho, \Omega)$ and $b(\rho, \Omega)$.

6.2.3.4 Extracting physical information from the model

The backbone curve connects the points in the FRCs where the phase difference between the harmonic forcing and the response is $\pi/2$ which also coincides with the maximum amplitude of FRCs [14]. The backbone curve provides critical resonance information of a nonlinear system. From the second equation of Eq. (6.11), we can derive a zero problem of the backbone curve as

$$b(\rho, \Omega) - \Omega = 0. \tag{6.21}$$

6.2.4 Summary of the data-driven modelling

Our first key assumption is the existence of the coordinate system $\mathbf{z}$ where the measured bifurcation diagram is identical to the bifurcation diagram in the invariant manifold. The second assumption is that the phase of the fundamental harmonic of the observed periodic response $\varphi(\mathbf{z}_s^\Gamma(t))$ is identical to $\mathbf{z}_s^\Gamma(t)$. Under these assumptions, the summarised procedure for data-driven modelling is as follows:

1. Train $b(\rho, \Omega)$ using the input-output relation defined in Eq. (6.15).
2. Train $a(\rho, \Omega)$ using the input-output relation defined in Eq. (6.19).
3. Train $\varphi(\mathbf{z})$ using the input-output relation defined in Eq. (6.20).

We can compute FRCs solving Eq. (6.11) using numerical continuation at a fixed value of Γ and using Ω as a bifurcation parameter once the model is trained. S-curves can be calculated by solving Eq. (6.11) using numerical continuation at a fixed value of Ω and using Γ as a bifurcation parameter.

6.3 ML modelling examples

We demonstrate two examples of ML modelling. One is a numerical 2-DOF nonlinear oscillator called a modified Shaw-Pierre example, where we have a ground-truth numerical model to assess the quality of the methodology. The other modelling example is built from the CBC experiment of the nonlinear electromagnetic oscillator.

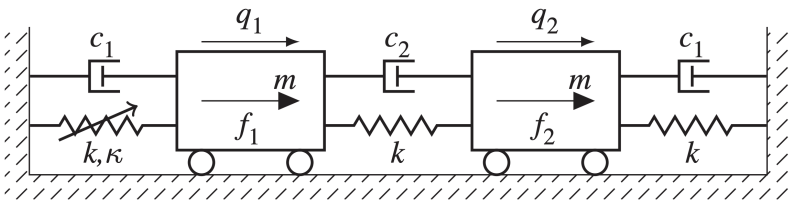

Figure 6.1: The modified Shaw-Pierre example in [14]. $m = 1$, $k = 1$, $c_1 = \sqrt{3}c_2 = 0.003$ and $\Gamma = 0.5$. m is mass, k is linear stiffness coefficient, c is linear damping coefficient, κ is quadratic stiffness coefficient, $f_1 = f_2 = F_0 \cos(\Omega t)$.

6.3.1 Numerical model: 2-DOF nonlinear oscillator

The data-driven modelling approach was applied to the system in Fig. 6.1. Training data sets are solutions of the numerical model with forcing amplitude $F_0 = 0.01$ and $F_0 = 0.007$ at 16 different frequencies with observation φ taken as the displacement x_1. The data-driven model is built for an invariant manifold tangent to the first eigenmode (modal frequency 1.0 rad/s).

For ML, square exponential kernels with ARD input transformation [81] is used for kernel ridge regression [45]. Using square exponential kernels, we can calculate $k(x, y)$ in Definition 2.2 as $\sigma exp(\sigma^2 \frac{-(x-y)^2}{2l^2})$ where σ, l are hyperparameters of the kernel which are output variance, length scale respectively. Also, we can set different length scales for different inputs using ARD input transformation; for example, the length scale for ρ and Ω can be set using different values which provides higher model flexibility. The hyperparameters of $a(\rho, \Omega)$, $b(\rho, \Omega)$ are optimised in the sense of minimising the loss function defined in Eq. (6.16) using the LBFGS algorithm [62]. We can see that the ML model computes FRCs accurately as in Fig. 6.2-(a) in training data sets.

We can also compute the FRCs for different forcing amplitudes ($F_0 = 0.3, 0.6, 0.9$, and 1.2) from the ML model as in Fig. 6.2-(b). The predicted FRCs from the ML model predict accurate FRCs compared to the ground-truth model. This shows that the selection of the structure of the basis model in Eq. (6.10) allows us to extrapolate the frequency-amplitude relation of periodic responses. The backbone curve is calculated from the model by applying a numerical continuation to Eq. (6.21), which shows a good correspondence with the linear modal frequency near the equilibrium. It is remarkable that the model captures accurate linear modal properties, even if it is trained with relatively high-amplitude oscillations.

Training observation is computationally more expensive than training $a(\rho, \Omega)$, $b(\rho, \Omega)$ since it requires the computation of larger kernel matrices where the input is a time series of periodic responses. We trained the observation using periodic responses at forcing amplitude $F_0 = 0.001$. Prediction of forced periodic response is accurate in trained forcing amplitudes as in Fig. 6.3 and untrained forcing amplitudes as in Fig. 6.4.

However, predicting the observation is less accurate at higher-amplitude periodic responses

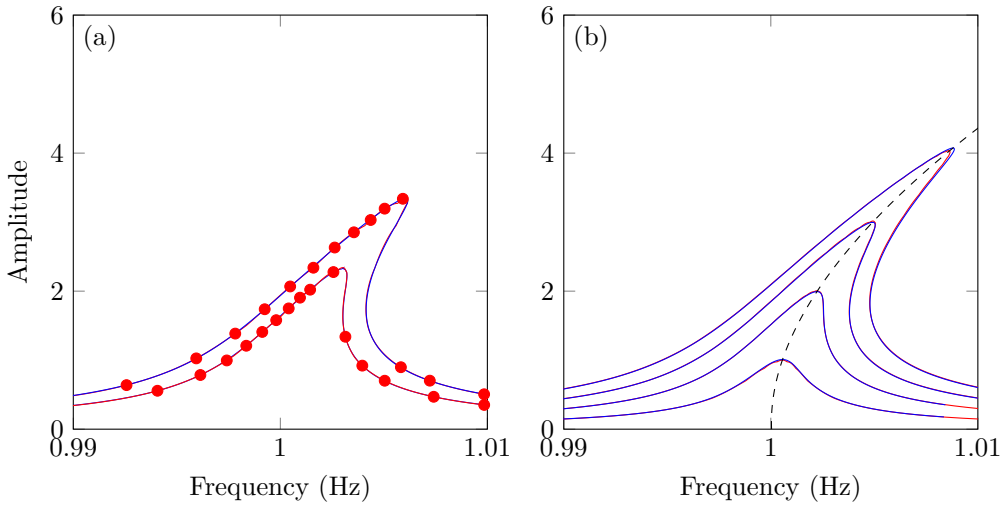

Figure 6.2: FRC computation at (a) training data sets (b) at untrained data sets with forcing amplitudes $F_0 = 0.003, 0.006, 0.009$ and 0.012. (—) is computed FRC from the ground truth model, (—) is computed FRC from the ML model, (- - -) is computed backbone curve from the ML model, and (●) are training data sets.

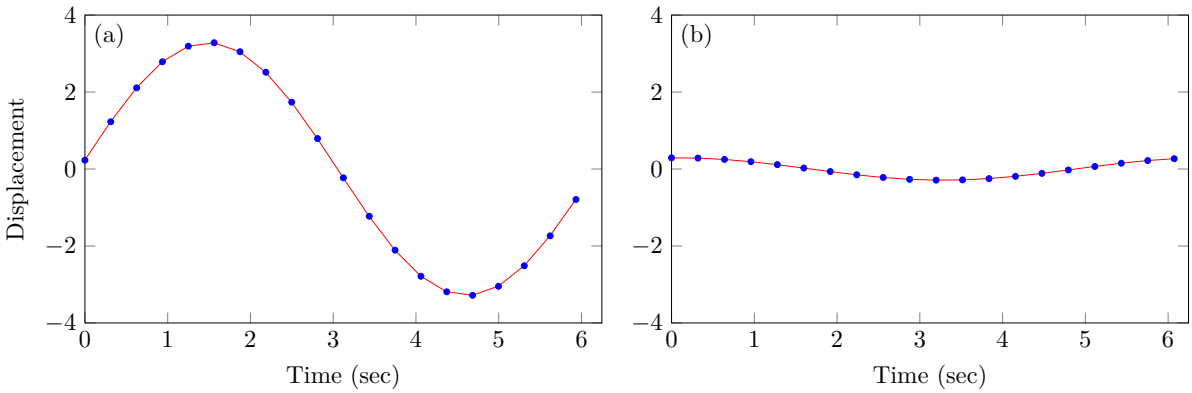

Figure 6.3: Predicting observation at trained data sets (a) $F_0 = 0.01$, $\Omega = 1.003$ rad/sec (b) $F_0 = 0.01$, $\Omega = 0.966$ rad/sec. (—) is the predicted time series from the model, and (●) is the time series of the ground truth model.

than the trained periodic responses. Fig. 6.5 (a) shows prediction of observations at forcing amplitude $F_0 = 1.002$ and the forcing frequency $\Omega = 0.988$ rad/sec, and Fig. 6.5 (b) shows prediction of observations at $F_0 = 1.002$, $\Omega = 1.008$ rad/sec. We can see that predicting the observation of the lower-amplitude response compared to the training data sets is accurate, but the higher-amplitude response has significant prediction errors. This shows that the extrapolation of φ is not accurate enough; therefore, training observations from a wide range of amplitude responses are suggested to have a model that can predict a wide range of amplitude responses.

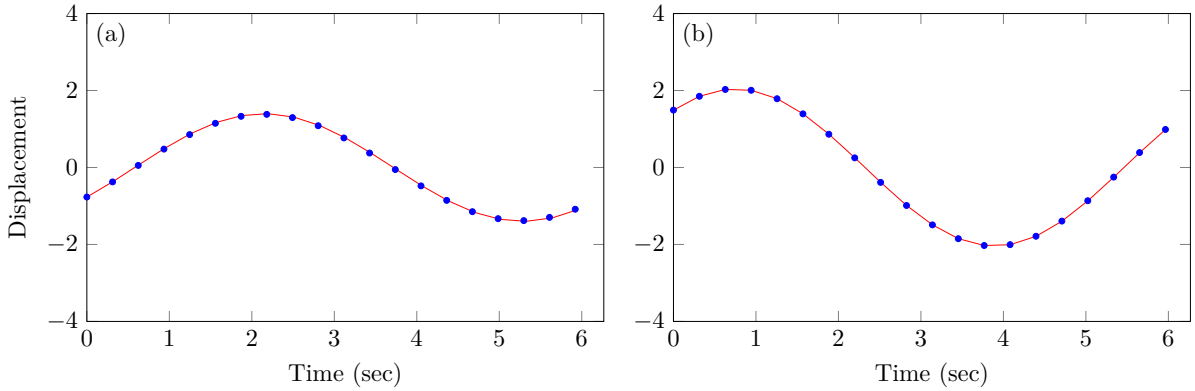

Figure 6.4: Predicting observation at untrained data sets (a) $F_0 = 0.005$, $\Omega = 1.002$ rad/sec (b) $F_0 = 0.009$, $\Omega = 1.00$ rad/sec. (—) is the predicted time series from the model, and (●) is the time series of the ground truth model.

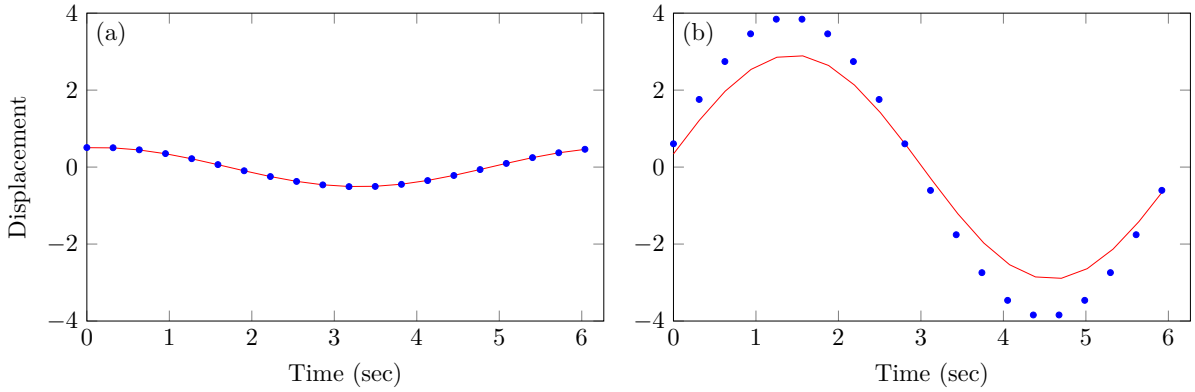

Figure 6.5: Predicting observation at untrained data sets with high forcing amplitudes (a) $\Gamma = 0.012$, $\Omega = 0.0988$ rad/s (b) $\Gamma = 0.012$, $\Omega = 1.008$ rad/s. (—) is the predicted time series from the model, and (●) is the time series of the ground truth model.

6.3.2 Physical model: nonlinear electromagnetic oscillator

The training data sets are measured from the experiment discussed in Section 3.2.1.1.

The model was first trained from the 24 measured S-curves, where CBC was used to track the branch of periodic responses, including unstable responses. The stabilising control algorithm and the set-up can be found in [82]. The forcing frequency is spaced between 17.5 and 23.4 Hz. $b(\rho, \Omega)$ was first trained using the square exponential kernel and the ARD input transformation on inputs ρ and Ω. The hyperparameters of $b(\rho, \Omega)$ are optimised using the cost function Eq. (6.16). $a(\rho, \Omega)$ was trained after training $b(\rho, \Omega)$ using a square exponential kernel and ARD input transformation. The hyperparameters of $a(\rho, \Omega)$ are optimised using the cost function Eq. (6.16) and using Eq. (6.19) to generate the input-output relation. After training $a(\rho, \Omega)$ and $b(\rho, \Omega)$, we can compute the S-curves using numerical continuation on Eq. (6.11). Three

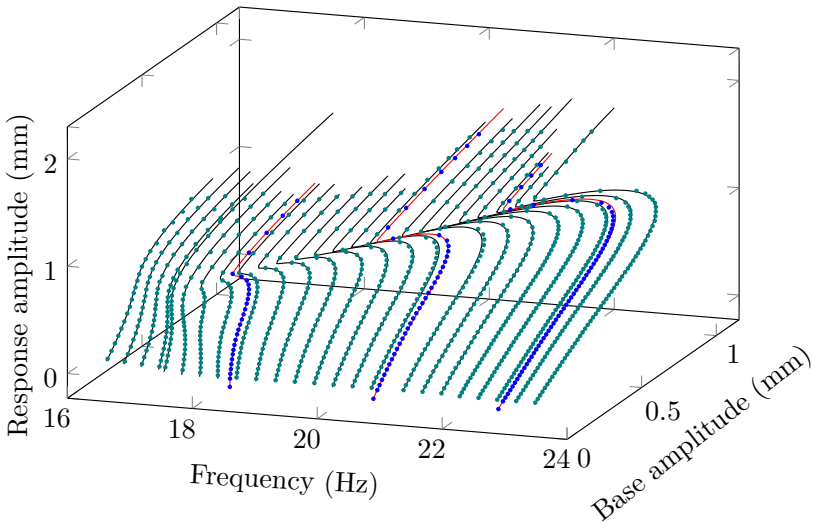

Figure 6.6: S-curves computed from an ML model trained using 24 measured S-curves. (●) are training data sets, (●) are validation data sets, and (—) are computed S-curves from the ML model.

S-curves are generated at the forcing frequency 18.5 Hz, 20.79 Hz and 22.79 Hz from the ML model, where the corresponding measured S-curves are validation sets of the ML model. We can see that the model accurately captures the S-curves in the training data sets as in Fig. 6.6, and it also predicts the S-curves at untrained frequencies, as seen in the validation sets.

To see the effect of the sparsity of the training data, we reduced the number of S-curves to 12 from the case shown in Fig. 6.6 and trained the ML model. The training process is identical to the 24 S-curves training case. The same validation sets are used for the above case. There is no significant decrease in the overall quality of the model in the validation sets, as shown in Fig. 6.7. However, there are slightly higher errors in the 20.79Hz S-curve, especially near the limit-point bifurcations.

The effect of the training data sparsity was further investigated by reducing the number of S-curves to 5 from the case shown in Fig. 6.6. The model training process is identical to the above two cases. As shown in Fig. 6.8, there is no significant decrease in the overall quality of the model in the validation sets. However, this ML model also has slightly increased errors in the 20.79Hz S-curve near the limit point. Model analysis shows that sufficient training data sets are needed to have a model that can predict accurate bifurcation points.

We can compute the backbone curve using trained ML models applying numerical continuation to Eq. (6.21). The backbone curve was measured in the experiment using CBC, where the algorithm and setup can be found in [82]. All three ML models predict very accurate backbone curves, as in Fig. 6.9. It is interesting to see that we can extract the backbone curve from the S-curves, which are experimentally much easier (see Section 3.2.1) to measure compared to backbone curves with crucial resonance information on the system. A small number of S-curves

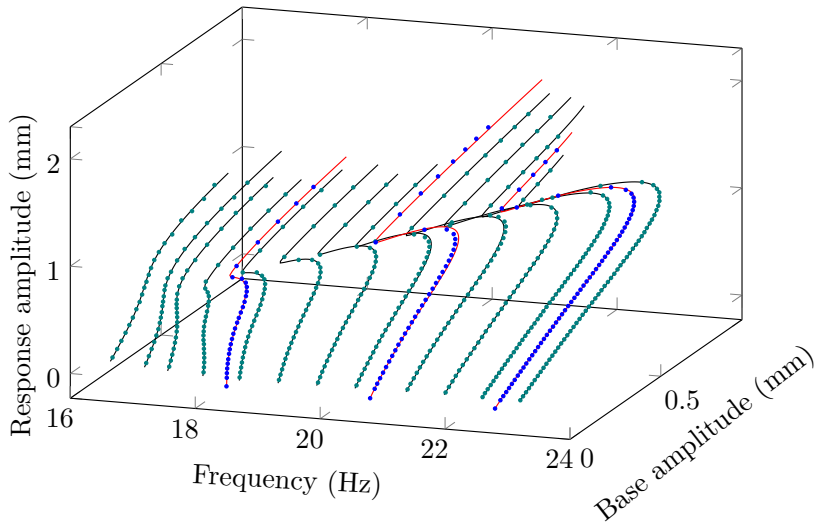

Figure 6.7: S-curves computed from an ML model trained using 12 measured S-curves. (●) are training data sets, (●) are validation data sets, and (—) are computed S-curves from the ML model.

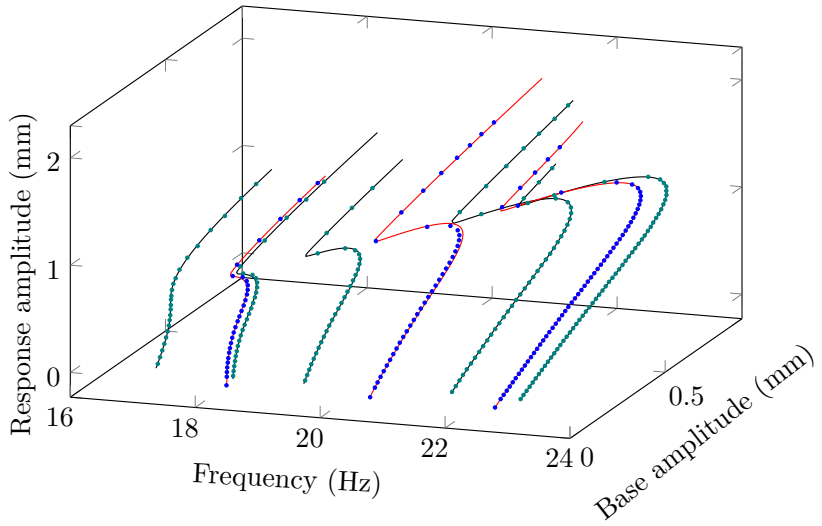

Figure 6.8: S-curves computed from an ML model trained using 5 measured S-curves. (●) are training data sets, (●) are validation data sets, and (—) are computed S-curves from the ML model.

is even enough to predict accurate backbone curves between the frequency range of the training data sets. However, the quality of the extrapolation of the model depends on the number of training data sets.

We can also predict the observation from the model using the forcing amplitude and the phase as input. It is shown in Fig. 6.10 where the predictions are accurate in the validation data sets.

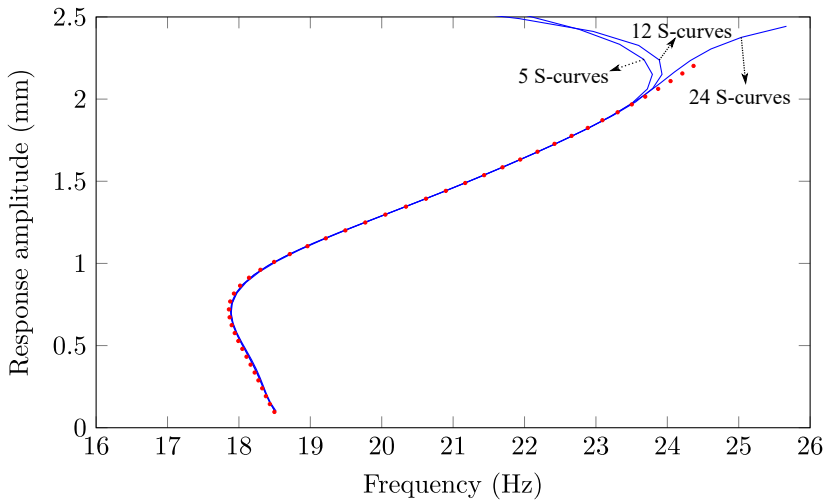

Figure 6.9: Prediction of backbone curve from ML model. (—) are computed backbone curves from the ML models, and (●) is a measured backbone curve. The measured backbone curve is measured between 18.59 Hz to 24.36 Hz using 47 points in frequency domain. S-curves used for ML model training ranges from 17.5 Hz - 23.4 Hz which are computed using numerical continuation.

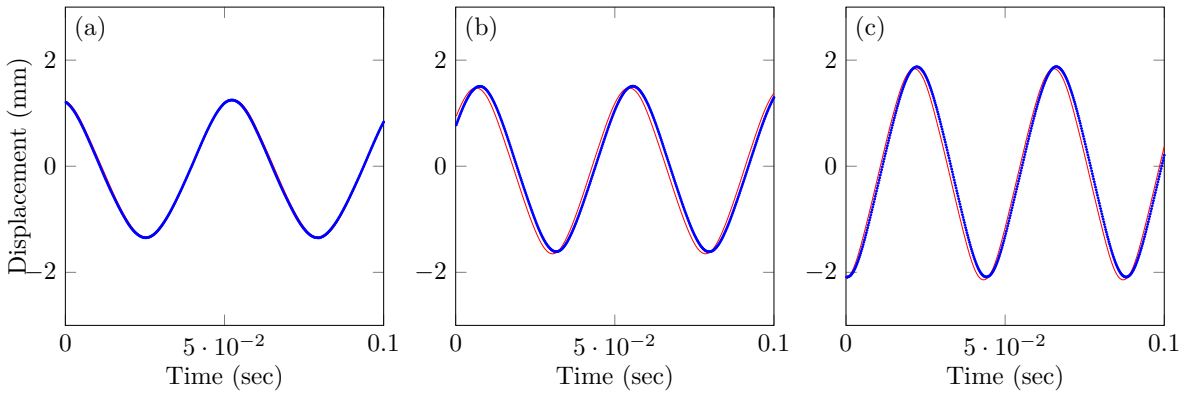

Figure 6.10: Prediction of time-series at validation sets (a) frequency 18.5 Hz, forcing amplitude 0.42 (b) frequency 20.8 Hz, forcing amplitude 0.16 (c) frequency 22.8 Hz, forcing amplitude 0.21. (—) is measured time series, and (—) is predicted time series from the model.

6.4 Conclusion

We developed a data-driven modelling methodology for forced mechanical systems using the information of the invariant manifold as domain knowledge. The reduced dynamics on the invariant manifold are trained using kernel ridge regression, where forced responses form the training data set. We also train observations in the sense of reproducing measured time series. The data-driven method in this research can predict high-amplitude bifurcation diagrams that accurately capture the frequency-amplitude relations.

We have shown two data-driven modelling examples: a numerical nonlinear mass-spring-damper system and an experiment of the nonlinear electromagnetic oscillator. Both examples accurately predict complex high-amplitude bifurcation diagrams– FRCs, S-curves, and backbone curves–from sparse training data sets. In addition, the trained observation accurately predicts the time series.

The current approach is limited to a two-dimensional invariant manifold of forced mechanical systems where no modal interaction is assumed. We are currently working on data-driven modelling for mechanical systems with modal interactions in ongoing research.

Data and code availability

Julia package developed for study in this chapter is available in repository ForcedKernel.jl.

CHAPTER 7

Conclusion

In this thesis, we developed a systematic approach to identifying ODE models, focusing on the bifurcations of the systems with Hopf bifurcations and harmonically forced mechanical systems. We summarise the findings of the thesis in this chapter. Moreover, we discuss the limitations of the thesis work and suggest areas for further research on bifurcation-based ODE model identification.

7.1 Conclusions

Experimental bifurcation analysis

In Chapter 3, we developed a PP-CBC scheme to extract the bifurcation structure from the experiment of self-excited systems. The fundamental idea is to parametrise the phase portrait of the LCOs using the angle of a two-dimensional phase plane constructed by two measured signals. Two parametrisation methods- elliptic and general polar curves- are suggested, and numerical examples show that the PP-CBC is robust in tracking the bifurcation structure. The developed PP-CBC algorithm was applied to an experiment on a flutter rig that undergoes a subcritical Hopf bifurcation in the wind tunnel.

We also discussed the CBC method for harmonically forced systems, which was previously studied. Specifically, we have shown that simplified Picard iteration schemes for the S-curve are robust from a numerical example. The S-curve measurement experiment for the electromagnetic oscillator was also introduced.

Parameter estimation of the mechanistic model with Hopf bifurcations

In Chapter 4, we developed parameter estimation methods for the system with Hopf bifurcations. We can apply the proposed model identification methods to the mechanistic models. Linearisation of the vector field is first identified using the small-amplitude free-decay response using the state-space approach. Then, the LCO near the Hopf bifurcation point is parameterised using the centre manifold reduction and the simplest normal form. Nonlinear parameters of the systems are initially optimised using the LCO parametrisation and updated using spectral collocation methods, taking account of higher amplitude LCOs to fit the bifurcation diagram. The proposed model identification method was applied to the experimental results presented in Chapter 3.

Bifurcation-based data-driven modelling of ODEs with centre manifolds

In Chapter 5, we developed the ODE model identification method for systems with centre manifolds. We use the existence of the centre manifold and the bifurcation structure as domain knowledge to set the basis model structure. The basis of the model is the normal-form-like equation, the reduced dynamics on the centre manifold, which is topologically equivalent to the experimental bifurcation analysis. The observation is modelled as a mapping between the centre manifold and the measured coordinates using neural networks. The model training is in two stages, where we train the observation to fit the phase portrait. In the second training stage, we train the speed of the oscillations to fit the time series prediction. The proposed ODE model identification method is applied to synthetic numerical data generated from the Van der Pol oscillator and the unsteady flutter model. We can see that the proposed data-driven modelling method is robust by comparing the bifurcation diagram and time series predictions with the ground truth model. The proposed data-driven modelling method was also applied to the data presented in Chapter 3.

Bifurcation-based data-driven modelling of ODEs with spectral-submanifolds

In Chapter 6, we developed the ODE model identification method for systems with spectral submanifolds. Specifically, we consider a harmonically forced system with an asymptotically stable equilibrium. The existence and dimension of a spectral submanifold are the domain knowledge of the modelling. We assume the existence of a coordinate system that gives identical frequency response curves to the measured bifurcation diagram. Using this assumption, we can construct input-output maps to identify reduced dynamics in the spectral submanifolds using kernel-ridge regression for data-driven modelling. The proposed method was designed to use S-curves and FRCs to train the model. We showed the robustness of the proposed data-driven modelling with a numerical 2 DOF nonlinear oscillator example trained from FRCs. The proposed data-driven modelling was applied to an experiment with an electromagnetic oscillator presented in Chapter 3. The predictions in the validation data sets and the comparison

of the predicted backbone curve and the measured backbone curve suggest that the proposed modelling method is robust enough and can extract valuable physical information, such as backbone curves.

7.2 Limitations of current work and future research suggestions

Experimental bifurcation analysis

We suggested two parameterisation methods for PP-CBC in this thesis. However, other parameterisation methods can be applied, such as using arclength as the parameterisation variable of the curve. This might increase the robustness to noise and can be applied to a broader range of phase portrait shapes.

Zero problems should be solved in the CBC experiment for noninvasive control, where Newton iterations and Picard iterations are typically used. However, the Picard iteration only works under specific conditions, and Newton iterations are highly time-consuming. A robust and time-effective noninvasive control target search scheme should be developed in which ML approaches such as kernel ridge regression can offer possibilities.

Parameter estimation of the mechanistic model with Hopf bifurcation

Chapter 4 only parameterised the LCOs near the Hopf bifurcation point. However, we can increase the order of the centre manifold reduction and the normal-form computation to consider the higher-amplitude branches of the LCOs in nonlinear parameter identification.

Also, the staged process here– identifying the linearisation first and identifying nonlinear parameters– could be the reason for the lack of model flexibility to fit the bifurcation diagram. This process can be replaced by recent ODE model identification packages considering linear and nonlinear parameters as free parameters. However, one should consider a way to resolve numerical integration errors while training unstable LCOs to the model.

Identifying the parameters of the mechanistic model gives a model that provides physical insight. However, a lack of model flexibility results in a relatively poor quality of capturing bifurcation diagrams in the high-amplitude region. To this end, combining the mechanistic model with universal approximators can improve the fitting of the bifurcation diagram.

Bifurcation-based data-driven modelling of ODEs with centre manifolds

In Chapter 5, the normal-form-like model has only a few free parameters in the radius direction. This results in a neural network heavily modifying the phase portrait, occasionally showing overfitting issues. We expect that having a flexible normal-form-like model, such as more free parameters, can resolve this issue.

The proposed model was trained using only LCOs and stability information from the LCOs. Using transient data sets that are not LCOs as training data can infuse more information into the model. However, a way to generate transient data sets that are not LCOs should be carefully considered.

Bifurcation-based data-driven modelling of ODEs with spectral-submanifolds

The data-driven modelling method is only developed for systems with 2-dimensional resonant spectral submanifolds. The modelling methods for spectral submanifolds with higher dimensions can be an exciting subject to study. The application of autoencoders to extract the coordinates of the reduced dynamics from the delay-embedded measured data can be an option.

7.3 Possible future application of the thesis

There are many opportunities for data-driven modelling of nonlinear dynamical systems. Recently, engineered systems have been heavily instrumented, and a massive amount of data is available. Therefore, there is a strong push for digital twins [4, 31] where experiments are mixed with mathematical models in a real-time feedback loop. In this context, the thesis work can be applied to digital twins of systems, where predicting the steady-state response depending on a control parameter is crucial. For example, ML models developed in this thesis can be applied to a digital twin of a lightweight drone to avoid the failure resulting from the aeroelastic flutter. Moreover, the ML models developed in this thesis are interpretable in the context of bifurcation theory which provides critical information on how the system will change depending on a parameter.

APPENDIX A

Aeroelastic model

The aeroelastic model considered in this thesis is unsteady formulation [1], which takes into account the unsteady effects of the flow. The equations of motion of this system are

$$\mathbf{M}\ddot{\mathbf{x}} + \mathbf{D}\dot{\mathbf{x}} + \mathbf{K}\mathbf{x} + \mathbf{N}(\alpha) = 0, \tag{A.1}$$

where $\mathbf{x} = [h, \alpha, w]^T$, h is the heave displacement, w is a state variable to take into account the unstable effects of the flow, and

$$\mathbf{M} = \begin{bmatrix} m_T + \pi\rho b^2 & m_w x_\alpha b - a\pi\rho b^3 & 0 \\ m_w x_\alpha b - a\pi\rho b^3 & I_\alpha + \pi(1/8 + a^2)\rho b^4 & 0 \\ 0 & 0 & 1 \end{bmatrix}, \tag{A.2a}$$

(A.2b)

$$\mathbf{D} = \begin{bmatrix} c_h + 2\pi\rho b U\hat{c} & (1 + \hat{c}(1-2a))\pi\rho b^2 U & 2\pi U^2 b(c_1c_2 + c_3c_4) \\ -2\pi(a+1/2)\rho b^2\hat{c}U & c_\alpha + (1/2-a)(1-\hat{c}(1+2a))\pi\rho b^3 U & -2\pi\rho b^2 U^2(a+1/2)(c_1c_2+c_3c_4) \\ -1/b & a - 1/2 & (c_2+c_4)U/b \end{bmatrix},$$

$$\mathbf{K} = \begin{bmatrix} k_h & 2\pi\rho b U^2\hat{c} & 2\pi U^3 c_2c_4(c_1+c_3) \\ 0 & k_\alpha - 2\pi(1/2+a)\rho\hat{c}b^2U^2 & -2\pi\rho b U^3(a+1/2)c_2c_4(c_1+c_3) \\ 0 & -U/b & c_2c_4U^2/b^2 \end{bmatrix}, \tag{A.2c}$$

$\hat{c} = c_0 - c_1 - c_3$ and $\mathbf{N}(\alpha) = [0, k_{\alpha 2}\alpha^2 + k_{\alpha 3}\alpha^3, 0]^T$. The meaning of the parameters and their values used are given in Table A.1, and in the schematic in Fig. A.1.

Parameter	Value	Description
U	0–25	Airspeed (m/s)
b	0.15	Wing semi-chord (m)
a	-0.5	Position of the elastic axis relative to the semi-chord (nd)
ρ	1.204	Air density (kg/m^3)
m_w	5.3	Mass of the wing (kg)
m_T	16.9	Mass of wing and support (kg)
I_α	0.1726	Wing moment of inertia about elastic axis (kg m^2)
c_α	0.5628	Pitch linear damping coefficient (kg m^2/s)
c_h	15.443	Heave linear damping coefficient (kg/s)
k_α	54.1162	Pitch linear stiffness (N/rad)
$k_{\alpha 2}$	751.6	Pitch quadratic nonlinear stiffness (N/rad^2)
$k_{\alpha 3}$	5006.7	Pitch cubic nonlinear stiffness (N/rad^3)
k_h	3529.4	Heave linear stiffness (N/m)
x_α	0.234	Distance between center of gravity and elastic axis (nd)
$c_{0,\ldots,4}$	(1, 0.1650, 0.0455, 0.335, 0.3)	Aeroelastic coefficients

Table A.1: Descriptions of the parameters of Eq. (A.1) and their values where applicable. Non-dimensional units are indicated by 'nd'.

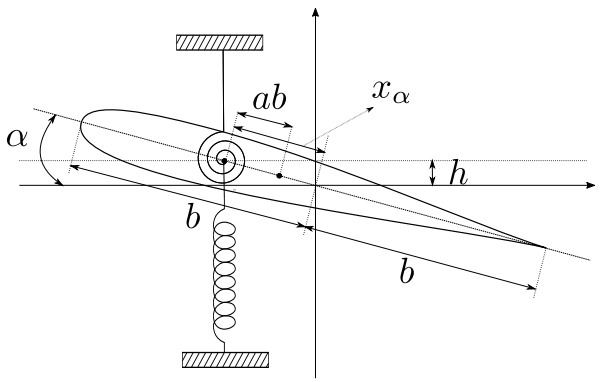

Figure A.1: Schematic of an aeroelastic system of Eq. (A.1).

Bibliography

[1] A. Abdelkefi, R. Vasconcellos, A. H. Nayfeh, and M. R. Hajj, *An analytical and experimental investigation into limit-cycle oscillations of an aeroelastic system*, Nonlinear Dynamics, 71 (2013), pp. 159–173.

[2] A. Abdelkefi, R. Vasconcellos, A. H. Nayfeh, and M. R. Hajj, *An analytical and experimental investigation into limit-cycle oscillations of an aeroelastic system*, Nonlin. Dyn., 71 (2013), pp. 159–173.

[3] A. Algaba, E. Freire, and E. Gamero, *Hypernormal Form for the Hopf-Zero Bifurcation*, International Journal of Bifurcation and Chaos, 08 (1998), pp. 1857–1887.

[4] N. Baker, F. Alexander, T. Bremer, A. Hagberg, Y. Kevrekidis, H. Najm, M. Parashar, A. Patra, J. Sethian, S. Wild, et al., *Workshop report on basic research needs for scientific machine learning: Core technologies for artificial intelligence*, tech. rep., USDOE Office of Science (SC), Washington, DC (United States), 2019.

[5] D. A. Barton and J. Sieber, *Systematic experimental exploration of bifurcations with noninvasive control*, Physical Review E, 87 (2013), p. 052916.

[6] D. A. W. Barton and S. G. Burrow, *Numerical continuation in a physical experiment: Investigation of a nonlinear energy harvester*, Journal of Computational and Nonlinear Dynamics, 6 (2010), p. 011010.

[7] D. A. W. Barton, B. P. Mann, and S. G. Burrow, *Control-based continuation for investigating nonlinear experiments*, Journal of Vibration and Control, 18 (2012), pp. 509–520.

[8] D. A. W. Barton and J. Sieber, *Systematic experimental exploration of bifurcations with noninvasive control*, Physical Review E, 87 (2013), p. 052916.

[9] R. Bellman and K. J. Åström, *On structural identifiability*, Mathematical Biosciences, 7 (1970), pp. 329–339.

[10] S. Beregi, D. A. Barton, D. Rezgui, and S. Neild, *Using scientific machine learning for experimental bifurcation analysis of dynamic systems*, Mechanical Systems and Signal Processing, 184 (2023), p. 109649.

[11] S. Beregi, D. A. Barton, D. Rezgui, and S. A. Neild, *Robustness of nonlinear parameter identification in the presence of process noise using control-based continuation*, Nonlinear Dynamics, 104 (2021), pp. 885–900.

[12] S. Beregi, D. Takacs, and G. Stepan, *Bifurcation analysis of wheel shimmy with non-smooth effects and time delay in the tyre–ground contact*, Nonlinear Dynamics, 98 (2019), pp. 841–858.

[13] Q. Bi and P. Yu, *Symbolic computation of normal forms for semi-simple cases*, Journal of Computational and Applied Mathematics, 102 (1999), pp. 195–220.

[14] T. Breunung and G. Haller, *Explicit backbone curves from spectral submanifolds of forced-damped nonlinear mechanical systems*, Proceedings of the Royal Society A: Mathematical, Physical and Engineering Sciences, 474 (2018), p. 20180083.

[15] N. J. Brunel, *Parameter estimation of ode's via nonparametric estimators*, Electronic Journal of Statistics, 2 (2008), pp. 1242–1267.

[16] F. Burden and D. Winkler, *Bayesian regularization of neural networks*, Artificial neural networks, (2008), pp. 23–42.

[17] E. Bureau, F. Schilder, M. Elmegård, I. F. Santos, J. J. Thomsen, and J. Starke, *Experimental bifurcation analysis of an impact oscillator - determining stability*, Journal of Sound and Vibration, 333 (2014), pp. 5464 – 5474.

[18] E. Bureau, F. Schilder, I. Ferreira Santos, J. J. Thomsen, and J. Starke, *Experimental bifurcation analysis of an impact oscillator - tuning a non-invasive control scheme*, Journal of Sound and Vibration, 332 (2013), pp. 5883–5897.

[19] J. C. Butcher, *Numerical methods for ordinary differential equations*, John Wiley & Sons, 2016.

[20] J. Carr, *Applications of centre manifold theory*, vol. 35, Springer Science & Business Media, 2012.

[21] M. Cenedese, J. Axås, H. Yang, M. Eriten, and G. Haller, *Data-driven nonlinear model reduction to spectral submanifolds in mechanical systems*, arXiv preprint arXiv:2110.01929, (2021).

[22] J. Chen and H. Wu, *Efficient local estimation for time-varying coefficients in deterministic dynamic models with applications to hiv-1 dynamics*, Journal of the American Statistical Association, 103 (2008), pp. 369–384.

[23] R. T. Chen, Y. Rubanova, J. Bettencourt, and D. K. Duvenaud, *Neural ordinary differential equations*, Advances in neural information processing systems, 31 (2018).

[24] S. Chen and S. A. Billings, *Representations of non-linear systems: the narmax model*, International journal of control, 49 (1989), pp. 1013–1032.

[25] K. Da, *A method for stochastic optimization*, arXiv preprint arXiv:1412.6980, (2014).

[26] R. Dandekar and G. Barbastathis, *Neural network aided quarantine control model estimation of global covid-19 spread*, arXiv preprint arXiv:2004.02752, (2020).

[27] J. Dawes, *Dynamical Systems course lecture notes*, University of Bath.

[28] J. V. Dillon, I. Langmore, D. Tran, E. Brevdo, S. Vasudevan, D. Moore, B. Patton, A. Alemi, M. Hoffman, and R. A. Saurous, *Tensorflow distributions*, arXiv preprint arXiv:1711.10604, (2017).

[29] G. Dimitriadis, *Introduction to Nonlinear Aeroelasticity*, John Wiley & Sons, 2017.

[30] M. Elmegård, B. Krauskopf, H. M. Osinga, J. Starke, and J. J. Thomsen, *Bifurcation analysis of a smoothed model of a forced impacting beam and comparison with an experiment*, Nonlinear Dynamics, 77 (2014), pp. 951–966.

[31] J. Eyre and C. Freeman, *Immersive applications of industrial digital twins*, The Industrial Track of EuroVR 2018, (2018).

[32] N. Fenichel and J. Moser, *Persistence and smoothness of invariant manifolds for flows*, Indiana University Mathematics Journal, 21 (1971), pp. 193–226.

[33] S. Fichera, S. Jiffri, X. Wei, A. Da Ronch, N. Tantaroudas, and J. Mottershead, *Experimental and numerical study of nonlinear dynamic behaviour of an aerofoil*, in PROCEEDINGS OF INTERNATIONAL CONFERENCE ON NOISE AND VIBRATION ENGINEERING (ISMA2014) AND INTERNATIONAL CONFERENCE ON UNCERTAINTY IN STRUCTURAL DYNAMICS (USD2014), 2014, pp. 3609–3618.

[34] D. Floryan and M. D. Graham, *Charts and atlases for nonlinear data-driven models of dynamics on manifolds*, arXiv preprint arXiv:2108.05928, (2021).

[35] W. Gander, R. Strebel, and G. H. Golub, *Fitting of circles and ellipses least squares solution*, in SVD and Signal Processing III, Elsevier, 1995, pp. 349–356.

[36] G. Haller and S. Ponsioen, *Nonlinear normal modes and spectral submanifolds: existence, uniqueness and use in model reduction*, Nonlinear dynamics, 86 (2016), pp. 1493–1534.

[37] B. Hammer and K. Gersmann, *A note on the universal approximation capability of support vector machines*, neural processing letters, 17 (2003), pp. 43–53.

[38] A. Haro and R. de la Llave, *A parameterization method for the computation of invariant tori and their whiskers in quasi-periodic maps: rigorous results*, Journal of Differential Equations, 228 (2006), pp. 530–579.

[39] M. Heinonen, C. Yildiz, H. Mannerström, J. Intosalmi, and H. Lähdesmäki, *Learning unknown ODE models with gaussian processes*, in International Conference on Machine Learning, PMLR, 2018, pp. 1959–1968.

[40] K. Hornik, M. Stinchcombe, and H. White, *Multilayer feedforward networks are universal approximators*, Neural networks, 2 (1989), pp. 359–366.

[41] M. Innes, *Flux: Elegant machine learning with julia*, Journal of Open Source Software, 3 (2018), p. 602.

[42] S. Jiffri, S. Fichera, J. Mottershead, and A. Da Ronch, *Experimental nonlinear control for flutter suppression in a nonlinear aeroelastic system*, AIAA Journal of Guidance, Control and Dynamics, 40 (2017), pp. 1925–1938.

[43] K. Kaheman, J. N. Kutz, and S. L. Brunton, *Sindy-pi: a robust algorithm for parallel implicit sparse identification of nonlinear dynamics*, Proceedings of the Royal Society A, 476 (2020), p. 20200279.

[44] T. Kalmár-Nagy, G. Stépán, and F. C. Moon, *Subcritical hopf bifurcation in the delay equation model for machine tool vibrations*, Nonlinear Dynamics, 26 (2001), pp. 121–142.

[45] M. Kanagawa, P. Hennig, D. Sejdinovic, and B. K. Sriperumbudur, *Gaussian processes and kernel methods: A review on connections and equivalences*, arXiv preprint arXiv:1807.02582, (2018).

[46] J. Kim, K. Lee, D. Lee, S. Y. Jin, and N. Park, *Dpm: A novel training method for physics-informed neural networks in extrapolation*, Comput. Phys, 378 (2019), pp. 686–707.

[47] B. Krauskopf, H. M. Osinga, and J. Galán-Vioque, *Numerical continuation methods for dynamical systems*, vol. 2, Springer, 2007.

[48] C. Kuehn, *Multiple time scale dynamics*, vol. 191, Springer, 2015.

[49] Y. A. Kuznetsov, *Elements of applied bifurcation theory*, vol. 112, Springer Science & Business Media, 2013.

[50] T. Lauss, S. Oberpeilsteiner, W. Steiner, and K. Nachbagauer, *The discrete adjoint method for parameter identification in multibody system dynamics*, Multibody system dynamics, 42 (2018), pp. 397–410.

[51] K. Lee, D. Barton, and L. Renson, *Reduced-order modelling of flutter oscillations using normal forms and scientific machine learning*, arXiv e-prints, (2020), pp. arXiv–2011.

[52] H. Lin and S. Jegelka, *Resnet with one-neuron hidden layers is a universal approximator*, in Advances in neural information processing systems, 2018, pp. 6169–6178.

[53] A. J. Linot and M. D. Graham, *Deep learning to discover and predict dynamics on an inertial manifold*, Physical Review E, 101 (2020), p. 062209.

[54] D. C. Liu and J. Nocedal, *On the limited memory bfgs method for large scale optimization*, Mathematical programming, 45 (1989), pp. 503–528.

[55] L. Ljung, *System identification*, Wiley Encyclopedia of Electrical and Electronics Engineering, (2001).

[56] L. Ljung and R. Singh, *Version 8 of the matlab system identification toolbox*, IFAC Proceedings Volumes, 45 (2012), pp. 1826–1831.

[57] C. Louizos, M. Welling, and D. P. Kingma, *Learning sparse neural networks through l_0 regularization*, arXiv preprint arXiv:1712.01312, (2017).

[58] C. C. Margossian, *A review of automatic differentiation and its efficient implementation*, Wiley interdisciplinary reviews: data mining and knowledge discovery, 9 (2019), p. e1305.

[59] T. McKelvey, *Frequency domain identification*, IFAC Proceedings Volumes, 33 (2000), pp. 7–18.

[60] K. Menda, L. Laird, M. J. Kochenderfer, and R. S. Caceres, *Explaining covid-19 outbreaks with reactive seird models*, Scientific Reports, 11 (2021), pp. 1–12.

[61] H. Miao, X. Xia, A. S. Perelson, and H. Wu, *On identifiability of nonlinear ODE models and applications in viral dynamics*, SIAM review, 53 (2011), pp. 3–39.

[62] P. K. Mogensen and A. N. Riseth, *Optim: A mathematical optimization package for julia*, Journal of Open Source Software, 3 (2018), p. 615.

[63] T. Nishijima, *Universal approximation theorem for neural networks*, arXiv preprint arXiv:2102.10993, (2021).

[64] T. E. Noll, J. M. Brown, M. E. Perez-Davis, S. D. Ishmael, G. C. Tiffany, and M. Gaier, *Investigation of the helios prototype aircraft mishap*, NASA Report, 9 (2004).

[65] A. Paszke, S. Gross, F. Massa, A. Lerer, J. Bradbury, G. Chanan, T. Killeen, Z. Lin, N. Gimelshein, L. Antiga, et al., *Pytorch: An imperative style, high-performance deep learning library*, in Advances in neural information processing systems, 2019, pp. 8026–8037.

[66] M. Peeters, R. Viguié, G. Sérandour, G. Kerschen, and J.-C. Golinval, *Nonlinear normal modes, part ii: Toward a practical computation using numerical continuation techniques*, Mechanical systems and signal processing, 23 (2009), pp. 195–216.

[67] R. Penrose, *A generalized inverse for matrices*, in Mathematical proceedings of the Cambridge philosophical society, vol. 51, Cambridge University Press, 1955, pp. 406–413.

[68] E. Pesheck, C. Pierre, and S. Shaw, *A new galerkin-based approach for accurate non-linear normal modes through invariant manifolds*, Journal of sound and vibration, 249 (2002), pp. 971–993.

[69] S. Peter and R. I. Leine, *Excitation power quantities in phase resonance testing of nonlinear systems with phase-locked-loop excitation*, Mechanical Systems and Signal Processing, 96 (2017), pp. 139–158.

[70] R. Pintelon and J. Schoukens, *System identification: a frequency domain approach*, John Wiley & Sons, 2012.

[71] A. Poyton, M. S. Varziri, K. B. McAuley, P. J. McLellan, and J. O. Ramsay, *Parameter estimation in continuous-time dynamic models using principal differential analysis*, Computers & chemical engineering, 30 (2006), pp. 698–708.

[72] Pyragas, *Delayed feedback control of chaos*, Philosophical Transactions of the Royal Society A: Mathematical, Physical and Engineering Sciences, 364 (2006), pp. 2309–2334.

[73] K. Pyragas, *Continuous control of chaos by self-controlling feedback*, Physics letters A, 170 (1992), pp. 421–428.

[74] K. Pyragas and A. Tamaševičius, *Experimental control of chaos by delayed self-controlling feedback*, Physics Letters A, 180 (1993), pp. 99–102.

[75] C. Rackauckas, M. Innes, Y. Ma, J. Bettencourt, L. White, and V. Dixit, *Diffeqflux. jl-a julia library for neural differential equations*, arXiv preprint arXiv:1902.02376, (2019).

[76] C. Rackauckas, Y. Ma, J. Martensen, C. Warner, K. Zubov, R. Supekar, D. Skinner, A. Ramadhan, and A. Edelman, *Universal differential equations for scientific machine learning*, arXiv preprint arXiv:2001.04385, (2020).

[77] C. Rackauckas and Q. Nie, *Differentialequations. jl–a performant and feature-rich ecosystem for solving differential equations in julia*, Journal of open research software, 5 (2017).

[78] M. Raissi, P. Perdikaris, and G. E. Karniadakis, *Inferring solutions of differential equations using noisy multi-fidelity data*, Journal of Computational Physics, 335 (2017), pp. 736–746.

[79] M. Raissi, P. Perdikaris, and G. E. Karniadakis, *Physics-informed neural networks: A deep learning framework for solving forward and inverse problems involving nonlinear partial differential equations*, Journal of Computational physics, 378 (2019), pp. 686–707.

[80] J. O. Ramsay, G. Hooker, D. Campbell, and J. Cao, *Parameter estimation for differential equations: a generalized smoothing approach*, Journal of the Royal Statistical Society: Series B (Statistical Methodology), 69 (2007), pp. 741–796.

[81] C. E. Rasmussen, *Gaussian processes in machine learning*, in Summer school on machine learning, Springer, 2003, pp. 63–71.

[82] L. Renson, D. A. Barton, and S. A. Neild, *Experimental tracking of limit-point bifurcations and backbone curves using control-based continuation*, International Journal of Bifurcation and Chaos, 27 (2017), p. 1730002.

[83] L. Renson, D. A. W. Barton, and S. A. Neild, *Experimental tracking of limit-point bifurcations and backbone curves using control-based continuation*, International Journal of Bifurcation and Chaos, 27 (2017), p. 1730002.

[84] L. Renson, A. Gonzalez-Buelga, D. Barton, and S. Neild, *Robust identification of backbone curves using control-based continuation*, Journal of Sound and Vibration, 367 (2016), pp. 145–158.

[85] L. Renson, A. Shaw, D. Barton, and S. Neild, *Application of control-based continuation to a nonlinear structure with harmonically coupled modes*, Mechanical Systems and Signal Processing, 120 (2019), pp. 449 – 464.

[86] L. Renson, A. Shaw, D. Barton, and S. Neild, *Application of control-based continuation to a nonlinear structure with harmonically coupled modes*, Mechanical Systems and Signal Processing, 120 (2019), pp. 449–464.

[87] D. Rezgui and M. H. Lowenberg, *On the nonlinear dynamics of a rotor in autorotation: a combined experimental and numerical approach.*, Phil. Trans. R. Soc. A, 373 (2015).

[88] A. Rosenfeld, *Digital picture processing*, Academic press, 1976.

[89] S. Ruder, *An overview of gradient descent optimization algorithms*, arXiv preprint arXiv:1609.04747, (2016).

[90] M. Ruzzene, A. Fasana, L. Garibaldi, and B. Piombo, *Natural frequencies and dampings identification using wavelet transform: application to real data*, Mechanical systems and signal processing, 11 (1997), pp. 207–218.

[91] F. Schilder, E. Bureau, I. F. Santos, J. J. Thomsen, and J. Starke, *Experimental bifurcation analysis—continuation for noise-contaminated zero problems*, Journal of Sound and Vibration, 358 (2015), pp. 251–266.

[92] B. Schölkopf, R. Herbrich, and A. J. Smola, *A generalized representer theorem*, in International conference on computational learning theory, Springer, 2001, pp. 416–426.

[93] A. A. Shabana, *Theory of vibration: an introduction*, Springer, 2018.

[94] J. Sieber, *Generic stabilizability for time-delayed feedback control*, Proceedings of the Royal Society A: Mathematical, Physical and Engineering Sciences, 472 (2016), p. 20150593.

[95] J. Sieber and B. Krauskopf, *Control based bifurcation analysis for experiments*, Nonlinear Dynamics, 51 (2008), pp. 365–377.

[96] R. Szalai, *Invariant spectral foliations with applications to model order reduction and synthesis*, Nonlinear Dynamics, 101 (2020), pp. 2645–2669.

[97] R. Szalai, D. Ehrhardt, and G. Haller, *Nonlinear model identification and spectral submanifolds for multi-degree-of-freedom mechanical vibrations*, Proceedings of the Royal Society A: Mathematical, Physical and Engineering Sciences, 473 (2017), p. 20160759.

[98] F. Takens, *Detecting strange attractors in turbulence*, in Dynamical systems and turbulence, Warwick 1980, Springer, 1981, pp. 366–381.

[99] K. Thomaseth and M. P. Saccomani, *Local identifiability analysis of nonlinear ODE models: how to determine all candidate solutions*, IFAC-PapersOnLine, 51 (2018), pp. 529–534.

[100] M. Thothadri and F. Moon, *Nonlinear system identification of systems with periodic limit-cycle response*, Nonlinear Dynamics, 39 (2005), pp. 63–77.

[101] C. Touzé, A. Vizzaccaro, and O. Thomas, *Model order reduction methods for geometrically nonlinear structures: a review of nonlinear techniques*, Nonlinear Dynamics, 105 (2021), pp. 1141–1190.

[102] L. N. Trefethen, *Spectral methods in MATLAB*, SIAM, 2000.

[103] J. M. Varah, *A spline least squares method for numerical parameter estimation in differential equations*, SIAM Journal on Scientific and Statistical Computing, 3 (1982), pp. 28–46.

[104] A. Vizzaccaro, L. Salles, and C. Touzé, *Comparison of nonlinear mappings for reduced-order modelling of vibrating structures: normal form theory and quadratic manifold method with modal derivatives*, Nonlinear Dynamics, 103 (2021), pp. 3335–3370.

[105] A. Vizzaccaro, Y. Shen, L. Salles, J. Blahoš, and C. Touzé, *Direct computation of nonlinear mapping via normal form for reduced-order models of finite element nonlinear structures*, Computer Methods in Applied Mechanics and Engineering, 384 (2021), p. 113957.

[106] M. Wainwright, *Advanced topics in statistical learning theory*, Spring 2009.

[107] B. H. Wang, D. B. Wang, Z. A. Ali, B. Ting Ting, and H. Wang, *An overview of various kinds of wind effects on unmanned aerial vehicle*, Measurement and Control, 52 (2019), pp. 731–739.

[108] S. Wang, Y. Teng, and P. Perdikaris, *Understanding and mitigating gradient flow pathologies in physics-informed neural networks*, SIAM Journal on Scientific Computing, 43 (2021), pp. A3055–A3081.

[109] S. Wiggins, *Normally hyperbolic invariant manifolds in dynamical systems*, vol. 105, Springer Science & Business Media, 1994.

[110] D. A. Winkler and T. C. Le, *Performance of deep and shallow neural networks, the universal approximation theorem, activity cliffs, and qsar*, Molecular informatics, 36 (2017), p. 1600118.

[111] P. Yu, *Computation of normal forms via a perturbation technique*, Journal of Sound and Vibration, 211 (1998), pp. 19–38.

[112] P. Yu and A. Y. T. Leung, *The simplest normal form of Hopf bifurcation*, Nonlinearity, 16 (2003), pp. 277–300.

[113] C. T. Zahn and R. Z. Roskies, *Fourier descriptors for plane closed curves*, IEEE Transactions on computers, 100 (1972), pp. 269–281.

[114] D. Zhang and G. Lu, *Review of shape representation and description techniques*, Pattern recognition, 37 (2004), pp. 1–19.

[115] H. Zhang, S. Abhyankar, E. Constantinescu, and M. Anitescu, *Discrete adjoint sensitivity analysis of hybrid dynamical systems with switching*, IEEE Transactions on Circuits and Systems I: Regular Papers, 64 (2017), pp. 1247–1259.